The Turbulent Structure of the Clear and Cloud-topped Convective Boundary Layer over Land

Arunchandra. S. Chandra

Doctor of Philosophy

Department of Atmospheric and Oceanic Sciences

McGill University

Montreal,Quebec

September 2012

A thesis submitted to McGill University in partial fulfillment for the requirements of the degree of Doctoral of Philosophy

DEDICATION

To my parents for giving me life
and to my teachers, family and friends for their inspiration, love and sharing their passions.

Acknowledgements

No one deserves more thanks than my advisor Pavlos Kollias for the success of this work. I wholeheartedly thank for his advice, support, constant motivation and giving me enough freedom.

I thank him for his continued support as an advisor, teacher, colleague and foremost, as a friend. He patiently critiqued my ideas and research methods to let me develop my independent research abilities, which i always cherish !. I feel that after working with him, I am more disciplined, simple, confident and independent.

I wish to thank my group: Aleksandra Tatarevic, Wanda Szymer, Ieng Jo, Jasmine Remillard, Veronique Meunier, Kevin Bowley, Katia Lamer, Kirk North, Paloma Borque, Heike Kalesse for their support and feedback during our group discussions. A special thanks to Wanda Szymer for her willingness to share wisdom on clouds and remote sensing. A very special thanks to Aleksandra Tatarevic and Ieng Jo for our friendship and making my difficult times a little easier.

Special thanks to my labmates, young curious minds and close friends: Mathew Gruber and Katia Lamer for our unending conversations both scientifically and personally. I am thankful to all administrative staff of the department for making my life easier through all the paperwork, with special thanks to Vaughn Thommasin, Ornella Cavaliere, Jennifer Marleau and Paula Domingues. Furthermore, my sincere gratitude to Michael Havas for his selfless help with our servers, computers and printers, and his assistance with latex.

I wish to thank all my friends at the department, to name only few: Patrick Martineau, Ayako Yamamoto, Joowan Kim, Radha Krishna, Kostas, Ali, Barbara, Marc Berenguer, Shinju, Dominik and Madalina for hours of togetherness, parties and outdoor activites.

Bruce Albrecht from University of Miami has been an inspiration for me to work on Boundary Layer and Cumulus Clouds. My sincere thanks to him for his support and feedbacks on my research work. I thank Ed Luke and Karen Johnson from Brookhaven National Laboratory for sharing their expertise on cloud radar data and processing.

My thanks also to my co-authors: Bruce Albrecht, Stephen Klein, and Scott Giangrande for their constructive criticisms on my research work.

A very special thanks to my friends Ramdas Satyan, Lakshmish Kowshik, Swaroop Visweswaraiah, Pannaga, Ksenia, Kshama Nargund, Vijay Badagi, Shankar, Deepa, Radha Krishna for sharing the moments of joy and bitterness, and making my stay in Montreal memorable. I also thank my fellow Montreal Kannadigas for sharing their wonderful memories with me. A big thanks to Bikram Yogis: Your friendship and our yoga keeping my life very focused and stress-free.

I also thank my teachers Jacques Derome, Henry Leighton, Frederic Fabry, and Pavlos Kollias for imbibing in me the rigor of physics, dynamics and remote sensing. Special thanks to my friends, Aneesh Subramanian, Shekar Chandra, Kshama and our group members (Kirk, Paloma and Heike) for proof reading my dissertation. A very special thanks to my close friend Shekar Chandra for his generous friendship, support, encouragement, and advice in both academic and non-academic. I also thank Vernoque Meunier for translating the thesis abstract to french.

My deepest gratitude to my father for his continued support, guidance and understanding. I owe everything to my mother for taking care of every need of mine. My special thanks due to my sister Anupama and her husband for their prayers. My nephew Pranav Bharadwaj (6 years) is always be dear to me. I thank my sister Saraswathi and her husband Nagaraj for their support and encouragement. my I am indebtful to my cousin Pradeep for his support and taking care of my family at the very difficult times.

Contribution of Authors

The research in this thesis was entirely carried out by me under the supervision of Prof. Pavlos Kollias. All texts, comprising structure and content of the papers are the result of numerous discussions, and were written by me and edited by Prof. Kollias. The other coauthors contributed in these papers through their suggestions and feedback, which improved the scope and quality of the research content. In the first manuscript, co-author: Dr. Scott Giangrande contributed through his suggestions on the methodology to correct for insect motion, and his feedback on the research content of the paper. The contribution from the other co-author: Dr. Stephen Klein was through his suggestions in the section on how to use the extended observational data set from this study for other modelling and parameterization studies, and his feedback on the research content of the paper. Prof. Kollias contributed to the research presented here through many discussions and much valuable feedback.

The idea for the first objective (”Turbulent Structure of Convective Boundary Layer over Land”, chapter 3) arose from the discussions between Prof. Kollias and myself. The version included here is the published material in the J. Climate.

The idea for the second objective (”Multi-year, Summertime Observations of Daytime Fair-Weather Cumuli at the ARM Southern Great Plains Facility”, Chapter 4) arose from the discussions between Prof. Kollias and myself. This chapter is submitted to the Journal of Climate and it is in subjudice right now. The co-author: Prof. Bruce Albrecht contributed in the second paper through his feedbacks on the diurnal cycle of the fair-weather cumuli and surface properties.

The idea for the third objective ("Evaluating the updraft characteristics in mass-flux schemes using Doppler Lidar observations", Chapter 5) was mine. The refined results in this chapter are to be submitted as a manuscript.

Statement of Originality

This thesis made several contributions towards understanding the turbulent structure of clear and cloud-topped boundary layer over land through long term observations.

1. Insect radar echoes within the CBL were considered to be a nuisance as they hinder our ability to detect fair-weather clouds during summer time. This study explored a potential to utilize the long-term radar insect echoes to study the turbulence structure in the CBL.
2. This study is first of its kinds to provide the composite day evolution of the turbulent parameters (e.g., Vertical velocity variance, vertical velocity skewness, updraft mass flux, plume width, etc.) of the CBL as models have difficulty in capturing the observed daytime evolution over land.
3. Observations on FWC over land are very sparse to evaluate the performance of shallow cumulus parameterizations. This study documented the daytime evolution of turbulence parameters (e.g., Vertical velocity variance, vertical velocity skewness, updraft mass flux, etc.), and geometrical properties (such as Cloud chord length, cloud aspect ratio, cloud thickness, etc.) of FWC using 14 years of cloud radar observations. These properties provide a crucial data set for assessing the distribution of scalars inside the cloud and serve as a robust observational basis for evaluation of LES and mass flux schemes over continental site.

4. The observational evidence reported in this study gave a new insight into the role of cloudiness on the subcloud structure, which would help to assess the boundary layer parameterizations by including the behavior of CBL and FWC properties under different cloudiness conditions.
5. This study demonstrated the careful use of Doppler lidar observations to evaluate the aspects of mass flux parameterizations to test its applicability over land. In this study, a new alternative method to estimate critical velocity is proposed from observations. The estimates from this approach can be used as a constraint in models to get proper vertical velocity distributions to predict the updraft properties at the cloud base.

Abstract

Over land, the daytime evolution of the convective boundary layer (CBL) is driven by the strong surface forcing evolution. Recent modeling studies have demonstrated that models cannot capture the observed evolution because of difficulty to represent turbulent processes in CBL and shallow cumulus clouds. The purpose of this thesis is to advance our understanding of the structure of clear and cloudy boundary layer over land by providing observational evidence using long-term data set. Specifically, it focuses on documenting the turbulent structure and properties of CBL and FWC using observations at the U.S. Department of Energy Atmospheric Radiation Measurement Program (ARM) Southern Great Plains (SGP) Climate Research Facility. First, Doppler velocity measurements from insects occupying the lowest 2 km of the boundary layer during summer months are used to map the vertical velocity component in the CBL. The observations cover four summer periods (2004–08) and are classified into cloudy and clear boundary layer conditions. A conditional sampling method is applied to the original Doppler velocity data set to extract coherent vertical velocity structures and to examine plume dimension and its contribution to the total turbulent transport. Profiles of vertical velocity variance, skewness, and mass flux are estimated to study the daytime evolution of the convective boundary layer during these conditions.

The properties of summer time FWC clouds are analyzed using the long data record

(14–year) of ground-based MMCR (Millimeter Wavelength Cloud Radar) observations at the ARM facility at the SGP site to document the macroscopic and dynamical properties of FWC clouds. Doppler velocities are processed for lower reflectivity thresholds that contain small cloud droplets having insignificant terminal velocities; thus Doppler velocities used as tracers of air motion. A fuzzy-logic based algorithm is developed to eliminate insect radar echoes in the boundary layer that hinder our ability to develop representative cloud statistics. The refined data set is used to document composite daytime evolution of cloud vertical velocity statistics, surface parameters and profiles of updraft and downdraft fractions, updraft and downdraft velocity, and updraft mass fluxes. Statistics on the cloud geometrical properties such as, cloud thickness, cloud chord length, cloud spacing and aspect ratios are calculated on the cloud scale.

Lastly, some of the updraft aspects in existing mass-flux parameterizations are tested using the recent observations from Doppler lidar deployed since Midlatitude Continental Convective Cloud Experiment (MC3E). The updraft aspects from two existing mass-flux schemes are evaluated with the Doppler lidar vertical velocity observations to test its applicability over land. The vertical velocity observations in the subcloud layer are analyzed for various cloud conditions by separately decomposing into clear and cloudy regions, and for various cloud fractions to investigate the role of clouds on the subcloud structure.

Abrégé

Sur les continents, l’évolution diurne de la couche limite convective (CLC) est entrainée par l’évolution des forçages de surface. Les modélisations récentes ont démontré que les modèles ne peuvent pas capturer l'évolution observée en raison des difficultés pour représenter les processus turbulents dans les nuages cumulus de la CLC et peu profonde. Le but de cette thèse est de faire progresser notre compréhension de la structure de la couche limite claire et nuageuse sur les terres en fournissant des données d'observation à long terme et en utilisant un ensemble de données. Plus précisément, elle met l'accent sur la documentation de la structure turbulente et les propriétés de la CLC et des cumulus de beau temps (CBT) à l'aide d’observation acquise au site de recherches « Southern Great Plains » (SGP) du programme « Atmospheric Radiation Measurement » (ARM) du Département américain de l'énergie. Premièrement, les mesures de vitesse Doppler des insectes, qui occupent les 2 km au bas de la couche limite pendant les mois d'été, sont utilisés pour cartographier la composante de vitesse verticale dans la CLC. Les observations portent sur quatre périodes estivales (2004 - 08) et sont classées en conditions de couche limite claire et nuageuse. Un procédé d'échantillonnage conditionnel est appliqué aux données d'origine de vitesse Doppler pour extraire les structures cohérentes de vitesse verticale et pour examiner la dimension du panache et sa contribution au transport turbulent total. Les profils de la variance et de l'asymétrie de la vitesse verticale et du flux de masse sont estimés pour étudier l'évolution diurne de la CLC au cours de ces conditions.

Les propriétés des nuages CBT d'été sont analysées en utilisant le long jeu de données d’observations (14 années) à partir du sol de MMCR (Radar de nuages à longueur d’onde millimétrique) au laboratoire SGP de ARM afin de documenter les propriétés macroscopiques et dynamiques des nuages CBT. Les vitesses Doppler sont traitées pour des seuils inférieurs de réflectivité qui contiennent de petites gouttelettes de nuages ayant des vitesses terminales négligeables; ainsi les vitesses Doppler sont utilisées comme des traceurs de mouvements de l'air. Un algorithme de logique floue a été développé pour éliminer les échos radar d'insectes dans la couche limite qui entravent notre capacité d'élaborer des statistiques représentatives des

nuages. L'ensemble de données raffineés est utilisé pour documenter l'évolution diurne compose des statistiques de vitesse verticale des nuages, les paramètres de surface et des profils des fractions de courant ascendant et descendant, la vitesse des courants ascendant et descendants, et les flux de masse ascendant. Les statistiques sur les propriétés géométriques des nuages telles que, l'épaisseur des nuages, la longueur de corde des nuages, l'espacement des nuages et les rapports d'aspect sont calculés sur l'échelle nuageuse.

Enfin, quelques uns des aspects des courants ascendants dans les paramétrisations existantes du flux de masse sont testées en utilisant les observations récentes du lidar Doppler déployé depuis l'expérience « Midlatitude Continental Convective Cloud Experiment » (MC3E). Les caractéristiques des courants ascendants de deux schéma existants de flux de masse sont évalués avec les observations de vitesse verticale du lidar Doppler pour tester son applicabilité sur les terres. Les observations de vitesse verticale dans la couche sous les nuages sont analysées pour différentes conditions nuageuses, en décomposant séparément les régions claires et nuageuses, et pour différentes fractions de nuages pour étudier le rôle des nuages sur la structure sous-nuageuse.

TABLE OF CONTENTS

LIST OF TABLES

LIST OF FIGURES

List of Acronyms and Abbreviations

ABL	Atmospheric Boundary layer
ACRF	ARM Climate Research Facility
ARM	Atmospheric Radiation Measurement
ARSCL	Active Remotely Sensed Cloud Locations
BL	Boundary Layer
BLH	Boundary Layer Height
CF	Cloud Fraction
DL	Doppler Lidar
CIN	Convective INhibition
CRM	Cloud Resolving Model
FL	Fuzzy-Logic
EMR	Electro Magnetic Radiation
EZ	Entrainment Zone
FWC	Fair-weather Cumuli
GCM	General Circulation Model
ILH	Insect Layer Height
LCL	Lifting Condensation Level
LES	Large Eddy Simulation
LFC	Level of Free Convection

LST	Local Standard Time
LWP	Liquid Water Path
MC3E	Midlatitude Continental Convective Clouds Experiment
ML	Membership Functions
ML	Mixed Layer
MMCR	Milli-Meter Cloud Radar
MWR	Micro-Wave Radiometer
PDF	Probability Density Function
RWP	Radar Wind Profiler
SCM	Single Column Model
SGP	Southern Great Plains
SNR	Signal to Noise Ratio
TKE	Turbulent Kinetic Energy
TSI	Total-Sky Imager
UTC	Coordinated Universal Time
VAP	Value-Added Product
WACR	W-band ARM Cloud Radar

List of Symbols

e_{avg}	Average turbulent kinetic energy in ms^{-1}
g	Acceleration due to gravity in ms^{-1}
h	Convective boundary layer height in m
inv	Inversion
M_u	Updraft mass flux in $kgm^{-2}s^{-1}$
$m_u{=}M_u/\rho$	Updraft mass flux in ms^{-1}
SNR	Signal to Noise Ratio in dB
$L{=}\frac{-u_*^3\theta_v}{kg(\overline{w'\theta_v'})_s}$	Monin Obukhov length in m
u_*	Frictional velocity in ms^{-1}
$(\overline{w'\theta_v'})_s$	Surface buoyancy flux in Kms^{-1}
T_v	Virtual temperature in K
T_v'	Virtual temperature perturbation in K
w^*	Convective velocity in ms^{-1}
w'	Vertical velocity perturbation in ms^{-1}
w_c	Critical velocity in ms^{-1}
w_u	Bulk updraft velocity in ms^{-1}
z	Height from the surface m
z_i	Mixed layer height in m
$\zeta = z_i/L$	Stability parameter

θ_v	Virtual potential temperature in K
θ_{v0}	Surface virtual potential temperature in K
σ_u	Updraft fraction
ρ	Air density in kgm^{-3}
ρ_u	Updraft air density in kgm^{-3}

CHAPTER 1
Introduction

1.1 Convective Boundary Layer

The convective boundary layer (CBL) plays an important role by acting as an interface for exchanging momentum, scalars (e.g., temperature, water vapor, gases), and pollutants from the surface into the free atmosphere (Betts 1973). Most of the solar radiation absorbed at the surface is transferred back to the atmosphere in the form of sensible and latent heat fluxes through boundary layer processes. Thus, the fuel (heat and moisture) to drive the atmosphere is supplied from the boundary layer. Most of the pollutants trapped inside the boundary layer, and their exchange with the free atmosphere is regulated by boundary layer processes. About half of the atmosphere's kinetic energy is dissipated in the boundary layer (abbreviated as BL in the following), and it is the important momentum sink for the atmosphere. To summarize, BL affects our lives directly and indirectly by influencing the weather (Stull 1998). The BL over land has a strong diurnal cycle because of its close connection with the surface. A typical daytime BL over land comprises of the surface layer, mixed layer (ML) and the entrainment zone (Inversion layer) (Garratt 1994).

The surface layer (depth is about tenth of a CBL depth) is the lowest part of the CBL, characterized by super adiabatic lapse rate, strong wind shear, where moisture decreases with height and is well described by Monin-Okukhov similarity theory (Monin and Obukhov 1954). The temperature and moisture within the surface layer depends strongly on the recent history of surface layer, and are diagnostically described using similarity theory. The main transport mechanism in the surface layer is turbulence. The convective updrafts have their origins in this layer and occur as thermals of buoyant air. The flow is highly turbulent in the surface layer because of the influence of both buoyancy and wind shear. The eddy structures (plumes) are small, and appear as ramp like structures in temperature and vertical velocity time series (Kaimal and Finnigan 1994).

The ML is where there is intense vertical mixing, which tends to leave conserved variables such as potential temperature and humidity nearly constant with height (Stull 1988). The vertical gradients of θ_v, mixing ratio and mean wind are small and the whole layer tends to warm at a uniform rate, implying that heat flux decreases linearly with height. The turbulence field in the mixed layer is dominated by coherent physical structures or by large eddies. Plumes from the surface layer merge together to form the large-diameter mixed-layer thermals. Typical scales of convective circulations are of the order of h (convective boundary layer height). With h=1000m and w*=$2ms^{-1}$, they have life times of order h/w*=500 seconds (Garratt 1994). The mixing can be generated by shears or convectively by buoyancy. Buoyant generated MLs tend to be more uniformly mixed than ones driven mechanically, because anisotropy in convection favors vertical motions, where anisotropy in shear favors horizontal motion (Kaimal and Finnigan 1994).

The entrainment zone is the region of statically stable air at the top of the mixed layer. Entrainment is defined as the exchange process by which the relatively quiescent fluid is engulfed by turbulent motions penetrating across the mean density interface and is subsequently mixed into the turbulent region. Where there is entrainment of free atmosphere air downward and overshooting thermals upward. Thin EZ's are expected for large temperature changes across ML top, because thermals will not penetrate as far and entrainment will be slow. Figure 1-1 shows the schematic of convective boundary layer circulations and entrainment of air through the capping inversion.

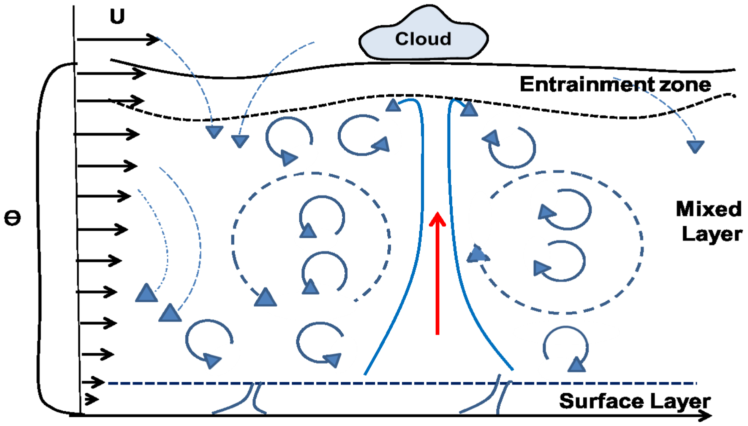

Figure 1–1: Schematic of convective boundary layer circulations and entrainment of air through the capping inversion (Adapted from Kaimal and Finnigan 1994).

The thermals in the ML carry a significant portion of the transports (e.g., mass, momentum, scalars) into the free atmosphere and into the clouds. Thermals (updrafts) are considered to be the invisible roots of clouds in the subcloud layer (Lemone and Pennell 1976) and carry a significant portion of the transports (e.g., mass, momentum, energy, scalars) into the free atmosphere. The shallow cumulus clouds, which are connected to the surface, provides an efficient mechanism for venting mixed layer air into the atmosphere thereby influencing cloud cover, temperature, moisture, winds, and CBL depth. Fair-weather cumuli (FWC) clouds are the visible manifestations of the vertical transport of momentum, heat, moisture, and pollutants from the surface into the free troposphere; thus, their lifecycle is strongly coupled to the surface fluxes (e.g., Betts 1973; Lemone and Pennell 1976; Betts 1973; Albrecht 1979; Betts and Viterbo 2005). This shallow mode of convection is most common in tropics and also part of subtropics.

1.2 Challenges in Clear and Cloud-topped Boundary layers

The poor representation of clear and cloudy boundary layer conditions in global climate models (GCMs) limits the predictability of cloud feedback in a changing climate (e.g., Tiedtke 1989; Bony et al. 2006; Teixeira et al. 2008). Transition from clear to cloudy conditions has major impact on both the surface energy budget and FWC are important in modulating the diurnal cycle (e.g., Brown et al. 2002; Lemone and Pennell 1976; Betts and Viterbo 2005). FWC play an important role in the atmospheric processes on various temporal and spatial scales. Locally, presence of FWC can cause a substantial change in turbulence intensity and internal structure of CBL (Stull and Eloranta 1984). Such a change in the CBL may further lead to subsequent variations in other processes or properties related to dispersion rates, chemical reaction rates and the removal of air pollutants from the CBL (e.g., Issac et al. 1984, Shipley and Browell 1984). Over land, the shallow mode of convection plays an important role in the preconditioning of deep convection (Lenderink et al. 2004).

Though, shallow cumuli coverage over land is $\sim$ 5%, yet it has significant affect on the global radiation budget (Norris 1998). Recent sensitivity studies have demonstrated that different shallow cumulus parameterizations used in different models lead to different responses of these clouds in the climate system (Bony et al. 2006). A controlling factor in the transition and evolution of clear and cloudy boundary layers is the diurnal cycle of the CBL. One of the key issues is to understand what regulates the mass flux of subcloud air into the cloud layer, its diurnal cycle, and the effect of clouds (e.g., Betts 1975; Esbensen 1975; Seibesma et al. 2003; Teixeira et al. 2008). Therefore, improving the representation of transport processes (turbulent local transport, thermals, shallow clouds) in the CBL is still an important issue for improving climate models(e.g., Rio and Hourdin 2008; Teixeira et al. 2008).

1.2.1 Modelling Challenges

GCM's don't have enough resolution to resolve the length scales associated with the BL thermals and shallow clouds ($\sim$ 1 km). In order to account for the physical effects of clouds and boundary layer in terms of large scale parameters through parameterization. High resolution models (e.g., LES (Large Eddy Simulation) cloud resolving models) and direct observations are needed to improve the understanding of the physics and represent its physical effects. Large-eddy simulations (LESs) have proved their suitability for modeling the diurnal evolution of clear and cloudy boundary layers (e.g., Schumann and Moeng 1991; Sullivan et al. 1994; Seibesma and Cuijpers 1995; Wang and Stevens 2000; DeRoode and Bretherton 2003; Zhu and Albrecht 2003). LES have successfully modeled the temporal evolution of macroscopic features of the CBL, such as the mixed-layer height and cloud fraction (CF) in well documented case studies (e.g., Deardorff 1974; Sommeria and Lemone 1978; Moeng 1984; Schmidt and Schumann 1989; Cuijpers and Duynkerke 1993; Seibesma et al. 2003). Efforts have been made to improve fair-weather cumuli parameterizations in models (e.g., Betts 1973; Albrecht 1979, 1981; Zhu and Albrecht 2003; Zhu and Bretherton 2004; Neggers et al. 2004; Berg and Stull 2005; Rooy and Seibesma 2008). These efforts have increased both our observational basis to understand FWC processes and modelling capabilities for better understanding the nature of these clouds and their interaction with large-scale dynamics (Zhu and Albrecht 2003, 2002). The scarcity of in-cloud observations and insufficient knowledge about the turbulent structure of the subcloud layer and its diurnal evolution limits our ability to evaluate higher-order vertical velocity statistics (variance, skewness) and the mass-flux representation of the vertical turbulent fluxes in the subcloud layer (e.g., Lenderink et al. 2004; Brown et al. 2002; Seibesma et al. 2003; Neggers et al. 2003; Stevens and Coauthors 2001).

1.2.2 Observational Challenges

Past CBL studies have been conducted during both cloud-free and cloudy conditions (e.g., Lenschow 1970; Kaimal et al. 1976; Lemone and Pennell 1976; Young 1988; Rauber and Coauthors 2007; Goke and Coauthors 2007). Coupled studies on the cloud and subcloud layer are limited to aircraft and tower measurements (e.g., Lemone and Pennell 1976; Warner 1977), data obtained from tethered balloon systems (e.g., Echternacht and Garstang 1976; Thompson et al. 1980), and multiple radiosonde ascents (Johnson 1977). Aircraft studies (e.g., Lemone and Pennell 1976;

Warner 1977; Squires 1958; Blyth and Latham 1985; Stull et al. 1997) on FWC clouds which provided invaluable information about the microphysical and dynamical structure of both CBL and FWC clouds. However, probing ABL and sampling shallow cumuli has its own observational challenges. Typically, surface tower observations cover only the surface layer (within 100 m). The aircraft penetrations gives detailed horizontal structure, but its vertical structure needs multi pass penetrations at many heights, which is limited due to the short life time of fair-weather cumulus cloud. Aircraft observations without on-board radar system are dimensionally challenged (Warner 1977). Furthermore, the high cost associated with routine aircraft observations make their use challenging.

1.3 Mass flux parameterization

The mass flux approach is a widely accepted framework for cumulus parameterization in large-scale models. The mass flux scheme assumes ensemble of cloud population by a bulk 1-D model with separately treating updraft and downdraft regions with in the model grid. It is first introduced by Ooyama 1971. In a numerical grid having cloud fraction (σ), an area average of a quantity ϕ (e.g., scalars such as temperature or mixing ratio, or vertical velocity) is expressed as a linear summation of contributions from cloud and environment (cloud free) separately.

$$\overline{\phi} = \sigma\phi^c + (1-\sigma)\phi^e \tag{1.1}$$

This approximation is reasonable for low cloud covers ($\sigma < 0.1$) where there is no significant difference between the quantity averaged over total area (includes cloudy and environmental area) compared the averaged over cloud free (environment) domain. Whereas for moderate-high cloud covers, the absolute errors in temperature and mixing ratio are generally small, but the errors in the vertical velocity are significant (varies from 10-20 % for σ between 20-30 %). So, this approximation is fairly reasonable for shallow cumulus clouds (with typical $\sigma \sim 15$ %). The most challenging part of this approach is to specify the cloud properties through closure assumptions. This scheme requires coupling of a cloud model/observations for specifying upward mass flux through the cloud bases. Knowing the profile of mass flux in the cloud layer, the convective mass fluxes can be estimated with the defining assumptions of single-plume mass flux scheme as

$$\rho\overline{w'\phi'} = M_u(\phi_u - \overline{\phi}) \tag{1.2}$$

where M_u is the cloud mass flux ($kgm^{-2}s^{-1}$), ϕ_u is bulk updraft-average value of some conserved variable ϕ, which changes with height because of the mixing of updraft with environment air, $\overline{\phi}$ is the value of ϕ in the environment. The expression for convective mass flux based on mass flux scheme is given by

$$M_u = \rho_u \sigma_u w_u \tag{1.3}$$

where ρ_u is the updraft air density, σ_u is the fractional area of grid box containing cumulus updrafts, and w_u is the convective updraft velocity. it is assumed that the storage of the quantity ϕ in cloud field represented by single updraft is neglected ($\partial(\sigma_u\phi_u)/\partial t = 0$).

There are two major issues in cumulus parameterizations. Turbulent mixing of the cloud updraft with its environment is critically important in determining how M_u and ϕ_u varies with height (Bretherton et al. 2004). The mixing rates (entrainment(E)/detrainment(D)) in the models are not directly computed, instead, the mixing rates are chosen for which the simulated thermodynamic profiles matches with the realistic thermodynamic profiles. However, sensitivities of mixing rates in convective layer, subcloud-layer and environment profiles are not clear. The second major issue is to specify the triggering (whether there is a convection or not), if so, how much (”closure”). There are different approaches to address this closure. In some approach (e.g., Emanuel and Raymond 1992; Bretherton et al. 2004), the cloud mass flux and triggering is controlled by the strength of weak stable layer capping the subcloud layer (inversion layer). In this study, we considered two mass flux schemes for shallow cumulus, one based on convective velocity scale (e.g., Grant 2001), and another based on CIN (Convection INhibition energy) in the subcloud layer top (e.g., Bretherton et al. 2004).

1.3.1 Convective velocity scale approach

This approach is based on mixed-layer scaling (Kaimal and Finnigan 1994) where it is assumed that the turbulence generated in the CBL is purely from surface buoyancy (turbulence due to wind shear is neglected). This approach based on the TKE budget in the subcloud layer, in which cumulus convection is assumed be associated with turbulent kinetic energy (abbreviated as TKE in the following) transport from subcloud to the cloud layer. Simplifying TKE budget for CBL assuming horizontal homogeneity, neglecting shear production gives an expression for cloud-base mass flux-given by

$$m_u = (\frac{1}{2}(1-\alpha) - A_\epsilon)w_* \tag{1.4}$$

where, m_u is cloud base mass flux (for convenience its defined as M_u/ρ with units of ms^{-1} where M_u is true mass flux and ρ is the air density), w_* is subcloud convective velocity scale.

$$w_* = (\frac{g}{\theta_v}\overline{w'\theta_{v0}}z_i)^{\frac{1}{3}} \tag{1.5}$$

In deriving the equations, it is assumed that A_ϵ and α are constants and independent of cloud conditions. Observational estimates of A_ϵ and α are constants, and they are rather uncertain.

1.3.2 TKE-CIN based approach

In the second approach, buoyant cumulus clouds form if the source air (updrafts) has sufficient vertical velocity to overcome the CIN in the inversion layer above subcloud layer top. The critical velocity (w_c) of a given undiluted air parcel leaving the mixed layer is computed such that it will reach its level of free convection and continue upward. Reliable estimates of w_c requires accurate detailed information about relative heights of the inversion, LCL (Lifting Condensation Level) of cumulus updrafts, LFC (Level of Free Convection) and vertical profile of environmental properties to estimate CIN. Practically CIN computation is very challenging, because it is highly sensitive to the vertical grid spacing, surface properties of air parcel and the difficulty in accurately estimating LCL, LFC and inversion layer top. Assuming Gaussian form for vertical velocity distribution, updraft fraction (σ_u) and updraft mass flux (M_u) at the inversion top are modelled as

$$\sigma_{inv} = \int_{w_c}^{\infty} f(w)dw = \frac{1}{2} erf(\frac{w_c}{\sqrt{2k_f e_{avg}}}) \tag{1.6}$$

$$M_{u,inv} = \overline{\rho_{inv}} \int_{w_c}^{\infty} wf(w)dw = \overline{\rho_{inv}} \sqrt{\frac{k_f e_{avg}}{2\pi}} exp(-\frac{w_c^2}{2k_f e_{avg}}) \tag{1.7}$$

where, $\overline{\rho_{inv}}$ is the density of source air at the LFC, k_f is a constant, e_{avg} is the average TKE in the subcloud mixed layer and $k_f e_{avg}$ is the vertical velocity variance at the inversion. The updraft velocity at the inversion is obtained from

$$w_{u,inv} = \frac{M_{u,inv}}{\sigma_{inv}\overline{\rho_{inv}}} \tag{1.8}$$

No entrainment is assumed to occur betwen the inversion and the LCL.

These schemes are formulated based on oceanic conditions. The major features that distinguishes marine ABL from its continental counterpart are moisture source, stability, lower boundary and mobility. Air is usually moister over the sea, compared over land, which results in different Bowen ratio (ratio of sensible to latent heat flux). The near-surface stability conditions over much of the ocean are near-neutral conditions, as a result, surface flux doesn't play a large role in determining the boundary-layer structure. Diurnal variations in the sea-surface temperature, and hence diurnal forcing of the marine ABL, are small because of the large heat capacity of the ocean. Over large areas, sea surface is uniform, which leads to less small-scale variability compared to the land counterpart. Over ocean, dynamical interaction occurs between ocean surface and surface-layer turbulence. Over land, the CBL is evolving continuously in response to the heating and cooling of the earth's surface. The mass flux schemes discussed above are based on many assumptions, such as steady state, horizontally homogeneity,no separate treatment of cloud conditions, Gaussian vertical velocity distribution,etc. In reality, one can't expect these simplified solutions to be representative for the unsteady conditions over land. However, the validity of the assumptions have to be tested and refined using observations.

1.4 Objectives

It is clear that long-term observations of subcloud layer turbulence and associated cloudiness are needed in order to develop robust descriptors of the daytime evolution of the CBL over land and thus provide observational targets for high and low resolution models. The presented thesis has three main objectives. The first objective is to document the structure of the subcloud layer from early morning to late afternoon. The second objective is to document the macroscopic properties and turbulent structure of FWC from early morning to late afternoon. The third objective is to test the assumptions made in the mass flux parameterizations and to refine the performance of these schemes over land.

The first objective is to investigate the turbulent structure of the summertime convective boundary layer over land during clear and cloudy conditions using long-term observations. A long-term study of the turbulent structure of the CBL is carried out using the data at the U.S. Department of Energy Atmospheric Radiation Measurement Program (abbreviated as ARM in the following) Southern Great Plains (abbreviated as SGP in the following) Climate Research Facility. Doppler velocity measurements from insects occupying the lowest 2 km of the boundary layer during summer months will be used to map the vertical velocity component in the CBL. The observations covering four summer periods 2004–08 will be analyzed by classifying them into cloudy and clear boundary layer conditions. Profiles of vertical velocity variance, skewness, and mass flux will be estimated to study the daytime evolution of the convective boundary layer during these conditions. A conditional sampling method is applied to the original Doppler velocity data set to extract coherent vertical velocity structures and to examine plume dimension and contribution to the turbulent transport.

The second objective is to study the properties of the summertime shallow cumulus clouds over land and its daytime evolution using long-term observations. 14-year of ground-based observations at the ARM SGP site will be analyzed to document the daytime composites of fair-weather cumuli clouds properties. Doppler velocities processed for lower reflectivity thresholds containing small cloud droplets having insignificant terminal velocities; thus Doppler velocities will be used as tracers of air motion. Composite diurnal variations of the cloud vertical velocity statistics, surface parameters and profiles of updraft and downdraft fractions, updraft and downdraft velocity, and updraft mass flux will be calculated. Apart from vertical velocity statistics, it is also aimed at calculating statistics on the cloud geometrical properties such as, cloud thickness, cloud chord length, cloud spacing and aspect ratios on the cloud scale.

The third objective is to test the validity of two existing mass flux schemes over land and investigate the factors influence the cloud base mass flux. The third objective aims to provide a more holistic (integrated) view using the observations from the planned MC3E field campaign. The new observations such as, i) the frequent soundings (eight versus four) provide a more complete picture of the diurnal evolution of the convective boundary layer and its stability, ii) the new Doppler lidar that will provide us with vertical air motion measurements from the surface to the cumulus clouds base. Using these new observations the updraft statistics in the subcloud layer will be analyzed in detail. In particular, certain aspects of two existing mass-flux schemes are evaluated using observations. In this study, we considered two mass flux schemes for shallow cumulus, one based on convective velocity scale (Grant 2001), and another based on CIN in the subcloud layer top (Bretherton et al. 2004).

Chapter 2 provides information on the available ground-based observations, instruments and outlines the methodology used in the analysis of the results shown in Chapters 3 and 4. Further, a brief description about the instruments, and their working principles are presented. The methodology for objectively classifying the data into clear and cloudy periods used for composite statistics calculations are explained. The detailed description about the newly developed fuzzy-logic algorithm to separate insect echoes inside clouds is explained with illustration.

Chapter 3 investigates the turbulent characteristics of CBL using long-term (4 years) radar insect echoes during summer-time at the SGP ARM facility. Composites of turbulent statistics such as vertical velocity skewness, variance, and updraft mass flux are calculated. To document the diurnal cycle and influence of cloudiness on the turbulent budget of CBL, statistics are further decomposed for different times of the day, and for various cloud fractions.

Chapter 4 documents the geometrical and turbulence characteristics of FWC using 14 years of doppler velocity observations inside FWC. Composites of daytime evolution of turbulent statistics such as vertical velocity skewness, variance, and updraft mass flux are calculated. The cloud geometrical properties such as cloud chord length, cloud spacing, aspect ratio and cloud thickness are calculated using large cloud sample ($\sim$ 5300 clouds) over 13 years.

Chapter 5 tests the performance of updraft aspects in two mass-flux schemes (Grant 2001; Bretherton et al. 2004) using Doppler lidar observations. Some of the assumptions (such as Gaussian assumption for vertical velocity distribution near cloud base, clouds do not contribute to subcloud layer turbulent kinetic energy budget, etc.) made in these schemes are evaluated for continental conditions using Doppler lidar observations. The computed updraft properties from these two schemes are compared with those estimated from the Doppler lidar observations.

CHAPTER 2
Data and methodology

2.1 Observational site

The US Department of Energy Atmospheric Radiation Measurements (ARM) program (www.arm.gov) was established in 1989 to address the uncertainties related to global climate change, with a specific focus on clouds and their influence on radiation transfer within the atmosphere. As a result, ARM Climate Research Facility (ACRF) established with an aim of providing long term measurements of radiation, clouds, aerosols and related atmospheric characteristics in diverse climate regimes. The first field site was in the Southern Great Plains (SGP, location: 36 36' 18.0" N, 97 29' 6.0" W), which is the largest and most extensive climate research facility in the world. This site consists of more than 300 instrument platforms, both in-situ and remote sensing instrument clusters which are arrayed across 142000 square kilometers. The site has homogeneous geography, with wide variability of cloud types and surface flux properties and large seasonal variations in temperature and specific humidity. This site is used as a test bed for evaluating both LES and SCMs. These physical features made ARM SGP site best suited for this study.

2.2 Scattering mechanisms

All active remote sensors such as radar/lidar transmits electromagnetic radiation (EMR) towards a target and part of its return energy (backscattered energy) is measured at the receiver end. In meteorological applications, the targets could be clouds, precipitation, particles, etc. The strength of the return signal provides information about the object composition (e.g., concentration or size or phase). The phase difference (Doppler shift) between transmitted and returned signal provides information about the target motion relative to the sensor, and the time delay between the transmitted and reflected signals determines the distance (range) of the target.

Back scattering occurs when particles or large gas molecules present in the atmosphere interact with and cause EMR to be redirected 180 degree from incident direction. How much scattering takes place depends on several factors including the wavelength of the radiation, the abundance of particles or gases, and the distance between the receiver and target.

Rayleigh scattering occurs when particles are very small compared to the wavelength of the incident radiation. For cloud radars, cloud droplets and small drizzle droplets are Rayleigh scatterers, but precipitating drops are non-Rayleigh scatterers. The scattering cross section per unit volume (η) in Rayleigh theory is given by

$$\eta = \pi^5 \lambda^{-4} |K|^2 Z \tag{2.1}$$

where λ is the wavelength of the radiation, $|K|^2$=0.93 is the refractive-index for liquid water and Z is the radar reflectivity factor given by:

$$Z = \frac{1}{2}\int_{0}^{\infty} (2r)^6 n(r) dr \tag{2.2}$$

where r is the droplet radius and n(r) is the droplet-size spectral density. In radar community, Z is typically expressed in decibels.

$$dBZ = 10log(Z) \tag{2.3}$$

Some radars are sensitive to receive return signals from refractive index inhomogeneities (e.g., air mass boundaries), and thus do not require cloud or precipitation targets to receive a signal. This type of scattering is known as Bragg scattering. Specular reflection (mirror-like reflection in which radiation from a single incoming direction is reflected into a single outgoing direction) is most important for radars of longer wavelength (particularly above tens of centimeters and into the meter range), especially those which are vertically pointed (generally the lower the elevation angle, the less likely specular reflection observed). The reason for this is that the atmosphere is primarily horizontally stratified. Thus stratified layers with very high refractive index gradients at their interfaces reflect some of the radar power directly back to a vertically pointing radar (Gossard et al. 1982). The effect may be enhanced with altitude when the layers appear concave to the radar due to Earths curvature.

The fundamental physical principles for Bragg backscatter are the same as those causing refraction of visible light. That is, as the refractive index of the medium changes, so does the velocity with which waves travel through the medium. This results in refraction of the wave in accordance with Snells ́ law. Turbulence within the atmosphere can be defined by the use of quantities known as structure parameters. They represent the root mean square difference between an atmospheric variable at two points a unit distance apart. Structure parameters can be defined for practically any atmospheric variable. Hardy et al., 1966 showed that the the radar reflectivity (η) is related to the refractive index structure constant, C_n^2 (and hence to gradients in refractive index) as follows

$$\eta = 0.38 C_n^2 \lambda^{1/3} \tag{2.4}$$

This relationship assumes that all measured reflectivity is due to the effects of refractive index gradients. Hence, if other scatterers are present, their effect must be filtered out if the relationship is to be valid. Also, the turbulence producing the inhomogeneities is assumed to be isotropic and fill the entire radar resolution volume. Finally, one half of the radar wavelength must fall within the inertial subrange.

2.3 Instruments

The main observations used in this study are from cloud radars and Doppler lidar. However, supplemental observations from laser ceilometer, microwave radiometers, eddy correlation sensors, radar wind profiler, and radio sondes have also been utilized in this study.

2.3.1 Millimeter wavelength cloud radars

Recent studies have emphasized the need to understand the role of clouds in the global radiation budget. Advances in radar technology since the past two decades has expanded the scope of radar meteorology from observing intensity and structures of precipitation to observing the structure and properties of clouds (Clothiaux et al. 2000). Millimeter wavelength radars have potential for probing cloud and ice particles ranging from a few micrometers diameter to precipitating drops. The cloud radar is also sensitive to the biological scatterers such as pollens and insects in the boundary layer (Clothiaux et al. 2000). The cloud radars have unique advantages over longer wavelength counterparts. Short wavelength radars have higher dynamical range without using high power transmitters or large antennas (Lhermitte 1987). These radars are also less susceptible to Bragg scattering, scattering due to biological targets such as insects, and ground clutter compared to centimeter radars. Furthermore, scatterers such as cloud droplets are treated as Rayleigh scatterers at cloud radar wavelength. Previous studies have demonstrated the benefit of cloud radars for defining the vertical structure of cloud reflectivity and velocity (e.g., French et al. 2000; Kollias et al. 2001). The small antenna size, flexibility to operate on mobile platforms and their ability to resolve fine time and spatial scales made it very suitable for observing detailed microphysics and dynamics. The particles within the radar (MMCR) resolution volume (i.e., horizontal scale of $\sim$10 m at 2km and vertical scale of 45 m, and beam width of 0.3) are randomly distributed. The amplitude and phase of scattered EMR from the particles in the radar resolution volume are random due to constructive and destructive interference (Kollias et al. 2007).

The particles within the radar pulse volume are moving relative to each other. The amplitude (A) of the electromagnetic wave scattered back to the radar will fluctuate from pulse to pulse, leading to distribution of amplitudes described by the

Rayleigh probability distribution (Marshal and Hitschfeld 1953). The distribution of backscattered power (A^2) follows an exponential relationship, and the average over all the power in the distribution is proportional to the total particle backscattering cross section per unit volume. This power is converted to an estimate of radar reflectivity (η) using Rayleigh approximation in equation (2.1).

The cloud radars used in the present study are equipped with the hardware to monitor the phase change of backscatter signal, which from Doppler theory, allows for an estimate of target motion. The phase shift from pulse to pulse contains information about motions of targets relative to the radar. Transforming the time series of backscattered powers using the Fourier transform gives series of particle backscattering cross sections. The distribution of backscattered power versus the corresponding velocities (Frequency shifts; towards or away from the radar) is called the Doppler spectrum. The total back scattered power is the zeroth moment, the mean Doppler velocity is the first moment, and the Doppler spectrum width is the second moment of the Doppler spectrum.

The present study focuses on exploiting the cloud radars capability to study the dynamics of the convective boundary layer and shallow cumulus clouds. The first part of its application involves the use of insect radar returns in the summertime convective boundary layer to study its turbulent structure over land. The second part involves its capability to observe cloud droplets in order to study the turbulent structure of non-precipitating shallow cumulus clouds over land. The methodology used to process the statistics is explained below.

2.3.2 Doppler lidar

Doppler lidar (hereafter DL) is an active remote sensing instrument that provides time-height resolved Doppler velocity and attenuated backscatter. It is an optical analog of a radar. The number concentration of the larger droplets that dominate the radar signal is relatively very low, and in the case of lidar, the signal is dominated by smaller droplets that are much more numerous. It is because in Rayleigh scattering for spherical droplets the radar backscattering is proportional to the droplet size exponent 6, while the lidar extinction coefficient to exponent 2. In both cases (radar and lidar), the signal is directly proportional to the number concentration. DL operates at the near-Infrared region (λ=1.5μm) of the EMR, and is sensitive to micron-sized aerosols. Since aerosols are ubiquitous in the lower troposphere, its motion can be used to trace the air motion assuming aerosols as a passive tracer. DLs are capable of measuring the wind field during clear-sky and non-precipitating convective conditions within the boundary layer with very good velocity precision ($\sim 0.1\ ms^{-1}$). In a vertical pointing-mode, DL provides time-height measurements of vertical velocity. A detailed description on Doppler lidar operation and principles can be found in Grund et al. 2001.

2.3.3 Radar Wind Profiler (RWP)

RWPs measure wind profiles and back scattered signal strength up to 5 km when operating in long-pulse mode. Its principle of operation is similar to radar. Since it operates at a longer wavelength (λ=30 cm), Bragg scattering allows RWP to detect clear-air targets. The Bragg signatures of maximum SNR gradients associated with reflectivity inhomogeneities can be used to locate the CBL top during clear–sky condition. RWP operating at 30 cm wavelength are also sensitive to Rayleigh scatterers such as insects and pollens within the CBL. The basic operating principle and application of wind profilers is explained in early classic papers (e.g., Ecklund et al. 1988; Rogers et al. 1993).

2.3.4 Laser Ceilometer

Laser ceilometers measure cloud-base height, vertical visibility, and potential backscatter signals by aerosols. The laser ceilometer transmits near-infrared pulses of energy and the receiver detects the energy scattered back by clouds and precipitation. It can detect up to three cloud layers simultaneously. The operating principle of the ceilometer is based on measurement of the time needed for a short pulse of light to traverse the atmosphere from the transmitter of the ceilometer to a backscattering cloud base and back to the receiver of the ceilometer. Instantaneous magnitude of the return signal will provide information on the backscatter properties of the atmosphere at a certain height. From the return signal, information about fog and precipitation, as well as cloud, can be derived. Since fog and precipitation can attenuate the light pulse, the cloud base signal can appear lower in magnitude in the return echo. More details on instrument specifications is explained in https://www.arm.gov/instruments/vceil.

2.3.5 Microwave Radiometer (MWR)

A MWR (MWRLOS; available online; http://www.arm.gov/instruments/mwr) provides measurements of column integrated amounts of water vapour and liquid water at 20 sec resolution. The instrument is essentially a sensitive receiver, tuned to measure the microwave emissions of the vapor and liquid water molecules in the atmosphere. This instrument receives the MWR emissions at two wavelength (23.8GHz and 31.4 GHz). These two frequencies allow simultaneous determination of water-vapor and liquid water burdens along the selected path. More information on the principles of MWR are explained in detail elsewhere (Liljegren et al. 2001).

2.3.6 Eddy correlation flux systems

The instrument setup involves a fast response 3-D wind sensor (sonic anemometer) to obtain orthogonal wind components and an open-path infrared gas analyzer to obtain water vapor density. The fluxes are obtained with the eddy covariance technique, which involves correlation of these turbulent measurements to compute turbulent fluxes of sensible and latent heat, as well as momentum. The principles of these systems are explained in detail in Kaimal and Finnigan 1994. The detailed instrument specifications is explained in https://www.arm.gov/instruments/ecor.

2.3.7 Total Sky Imager (TSI)

The TSI provides time series of hemispheric sky images during daylight hours and retrievals of fractional sky cover for periods when the solar elevation is greater than 10 degrees. TSI Model (TSI-660) is an automatic, full-color sky imager system that provides real-time processing and display of daytime sky conditions. An image-processing program running on a PC workstation captures images via TCP/IP at a 30sec sampling interval and saves them to JPEG files that are analyzed to infer both fractional sky cover and sunshine duration. The details of the TSI can be found from the following website (https://www.arm.gov/instruments/tsi).

2.3.8 Radiosondes

A balloon-borne sounding system provides a vertical profile of the atmosphere's thermodynamic and kinematic states (temperature, humidity and wind speed and direction). Radiosondes are launched at the site 4 times per day. The details about the radiosonde system are explained in https://www.arm.gov/instruments/sonde.

The specifications of the instruments discusses above are provided in the table (Table 2.1).

2.4 Techniques and Algorithms

This section contains the methodology and techniques applied to the data in Chapter 3 and 4. The methodology for objectively classifying the data into clear and cloudy periods, and a technique to estimate the BL height from wind profiler data are discussed. The correction for insect motion, and a detailed description about the newly developed fuzzy-logic algorithm to separate insect echoes inside clouds are explained.

2.4.1 Estimation of BL height from wind profiler

Estimates of the BLH are needed to normalize the turbulent statistics within CBL. Diurnal evolution of turbulent statistics demands frequent (in this case, hourly) measurments of BLH to scale accordingly. Measurements of potential temperature and mixing ratio from soundings can be used to retrieve estimates of the BLH, however, sounding-based estimates of the BLH are not available at the temporal resolution required for hourly scaling. An alternative approach for retrieving the BLH is the use of the 915-MHz RWP (Grimsdell and Angevine 1998), which is sensitive to Bragg scattering from gradients of the atmospheric refractive index. During clear-air and non-precipitating conditions, the RWP backscatter exhibits a local maximum at the top of the CBL because of the presence of strong gradients in the temperature and humidity fields. An example of RWP-retrieved mixed layer heights (black circles) as compared with the two estimates obtained from collocated ARM radiosonde launches (red crosses) is shown in Fig. 2-1.

A subset of the retrieved BLH values from the RWP is evaluated using the BLH estimates using data from atmospheric soundings collected within the same hour period (Fig. 2-2). The comparison exhibits good agreement between the BLH estimates with a correlation coefficient of 0.9.

2.4.2 Classification of clear and cloudy periods

In order to assess the differences in CBL structure between clear and cloud-topped conditions, a screening prcess has to be done to separate the two conditions. Every 1-hour period, the observations are classified as clear and cloudy using a conservative threshold combining the collocated ceilometer and TSI. Hourly periods are

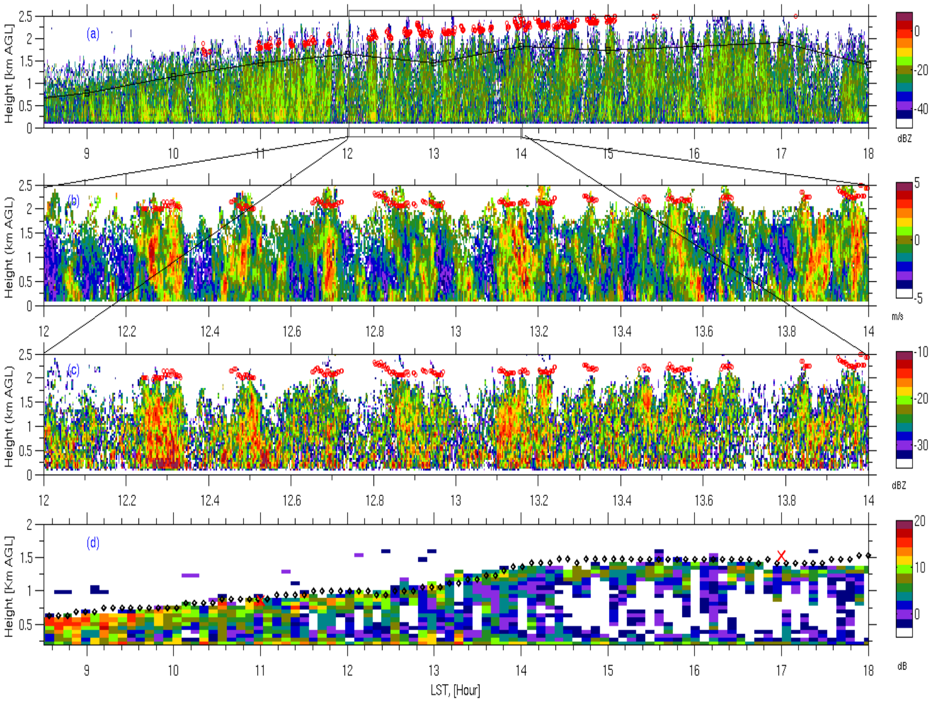

Figure 2–1: Example of time-height mapping of (a) MMCR reflectivity factor during a cumulus-topped event on 22 Jul 2006. Red dots indicate the cloud base measured from a ceilometer. Black lines indicate the objectively defined hourly ILH (Insect Layer Height). (b) MMCR Doppler velocity for the period 1200-1400 LST. (c) MMCR reflectivity for the period 1200-1400 LST. (d) Sample diurnal variation of RWP SNR during a clear-sky day (20 Jun 2006). Black diamonds indicate the algorithm-retrieved mixed layer heights based on SNR gradient. Red crosses are the mixed layer heights estimated using the virtual potential temperature profile from radiosondes launched at 1100 and 1700 LST.

classified as clear if the ceilometer-based hourly cloud fraction is zero and the opacity-based TSI hourly cloud fraction is less than 0.1. Extensive visual inspection of the TSI images is done to validate the classification. Cloudy hourly periods are further classified in three categories according to their cloud fraction: low (0–20%), medium

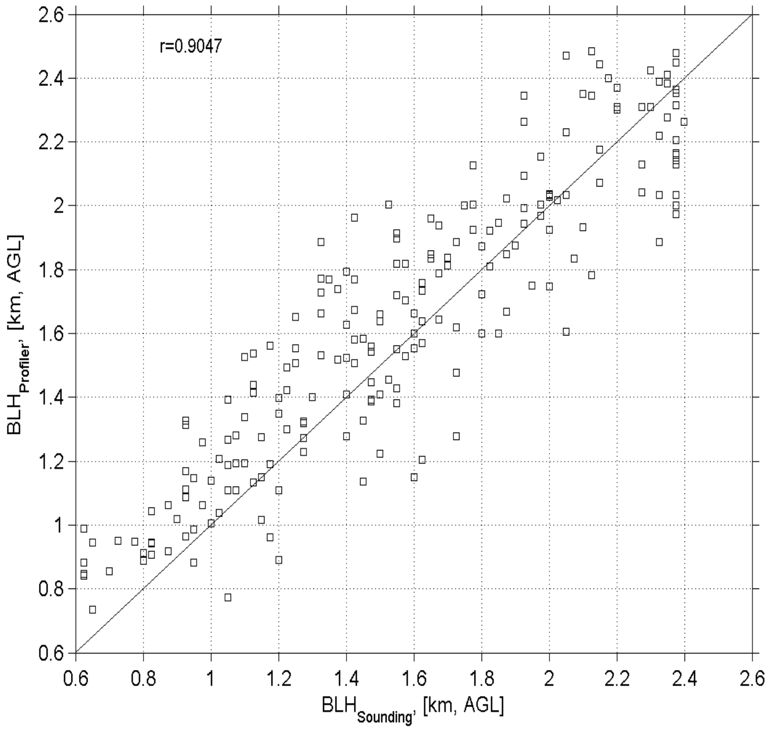

Figure 2–2: Comparison of BLH estimated from the soundings to the profiler-retrieved BLH based on refractivity gradient from the 4-yr dataset (2004-07). Soundings launched at 1100 and 1700 LST are compared with the BLH values nearest in time from the profiler.

(20–60%), and high (60–100%). Precipitation periods are removed using the rain gauge measurements and the MMCR first detection height and intensity (reflectivity threshold of -17 dBZ) to sample only the non-precipitating clouds. Overcast conditions (stratus or stratocumulus) are filtered out using the TSI and ceilometer.

2.4.3 Correction for insect motion

The first part of the analysis involves the use of insect radar returns from MMCR for studying turbulence in the CBL. For turbulence calculations, the mean of the vertical velocity data averaged over a period should be zero. The long-term velocity observations from the MMCR dataset in clear-sky conditions indicate a net downward velocity of 0.2-0.4 ms^{-1} in the lower half of the CBL that approaches zero near the insect layer top. The range of net downward velocities reported are comparable to the insect velocities observed from past studies (e.g., Riley 1992; David and Hardie 1998; Schaefer 1976; Riley and Reynolds 1979) and also in a recent field campaign (International H2o Project (IHOP-2002) field campaign over SGP location) using the wyoming airborne cloud radar (**?**). The excellent discussion in GM05 indicates that insects introduced stronger downward biases in the presence of stronger updrafts. Thus, the effect of the insect motion in the observed Doppler velocity is more than the introduction of a systematic bias. In this study, equation 2 in GM05 is adopted to correct the observed MMCR Doppler velocities for insect motion. However, this study uses Doppler velocities from a 35 GHz radar, and GM05 utilized a 94 GHz radar. Thus, as a preliminary test, a comparison between between the 35 and 94 GHz Doppler velocities from the SGP site was done. The study concluded that there is no difference in the observed Doppler velocity values

2.4.4 Algorithm to remove insect echoes in clouds

The insect echoes that overwhelm the MMCR returns in the lowest 2–3 km during the warm season hinders our ability to document fair-weather cumuli (FWC) at the ARM SGP is (e.g., Clothiaux et al. 2000; Luke 2008; Chandra et al. 2010; **?**). The ARSCL VAP is the most popular data product in the ARM archive and it is often used as the starting point for deriving cloud macroscopic (e.g. cloud climatology) and cloud microphysical and dynamical properties. As part of the ARSCL standard quality control, insect contamination is addressed by classifying MMCR echoes as either insects or mixture of cloud and insect returns. No automated algorithm is available, and often manual editing is required. In spite of the extensive quality control efforts, there is considerable misclassification of insect echoes as cloud echoes and the viceversa. This is often the case when the ceilometer detects a FWC base and there is little information to enable classification of the radar echoes above the ceilometer-derived cloud base. The MMCR echoes above the cloud base can be: i) all cloud related returns (in the absence of insects and if the radar reflectivity of the hydrometeors is above the sensitivity of the MMCR, ii) cloud returns near the cloud base in the cloud is shallow and insect returns above and iii) insects returns only, if the radar reflectivity of the hydrometeors is below the sensitivity of the MMCR. Thus, additional screening is required before the MMCR data can be used for the estimation of FWC properties (e.g., cloud top height and updraft fraction).

Two representative examples of insect contamination in the ARSCL VAP are shown in Fig. 2-3. The top panel shows the time-height plot of MMCR reflectivity as reported in ARSCL. The first example (Fig. 2-3a1) shows broken shallow cumulus with the ceilometer-defined cloud base and MMCR-defined cloud top shown in black. The second example (Fig. 2-3a2) is from a shallow, continuous MMCR echo. All MMCR echoes below the ceilometer-defined cloud base have been removed and classified as insects. The corresponding WACR co-polar channel observations are shown in Fig. 2-3b1-2. The WACR detects almost the same echoes as the MMCR in the case of the broken cumulus (Fig. 2-3b1) and no echoes in the cases of the low stratiform-like cloud (Fig. 2-3b2). The small offset in the radar reflectivity values of the MMCR and WACR is due to small calibration offset or/and mie effect due to targets greater than ∼ a mm. At W-band, non-Rayleigh scattering suppresses the intensity of the insect radar returns by 20 dB on average compare to their respective value at Ka-band (see Fig. 13 in Luke et al., 2008). Thus, the WACR detects a shallower insect layer and lower insect radar reflectivity, and in some cases, depending on the insect layer characteristics, the WACR detects no insect echoes if their intensity is below the sensitivity of the radar (Fig. 2-3) The WACR echoes in the first case (Fig. 2-3b1) are from hydrometeors and this is verified by the absence of WACR cross-polar signal (Fig. 2-3c1,c2). The LWP time series (Fig. 2-3d1,d2) further support the provided interpretation of the MMCR and WACR echoes. Significant values of LWP values are reported during the FWC periods compared to the intermitted clear sky periods (Fig. 2-3d1) while no such variability is observed during the second case (Fig. 2-3d2). The easiest approach to separate insect echoes from cloud is to use WACR capability to detect insect from cloud echoes. The WACR data are limited (only couple years of intermitted operations). However, the WACR data was very limited (only couple of years of intermittent operations) compared to the long-term (14 years) observations from MMCR.

Luke 2008 developed a technique to remove insects based on radar Doppler spectra. But the lack of MMCR Doppler spectra before 2005 and the significant

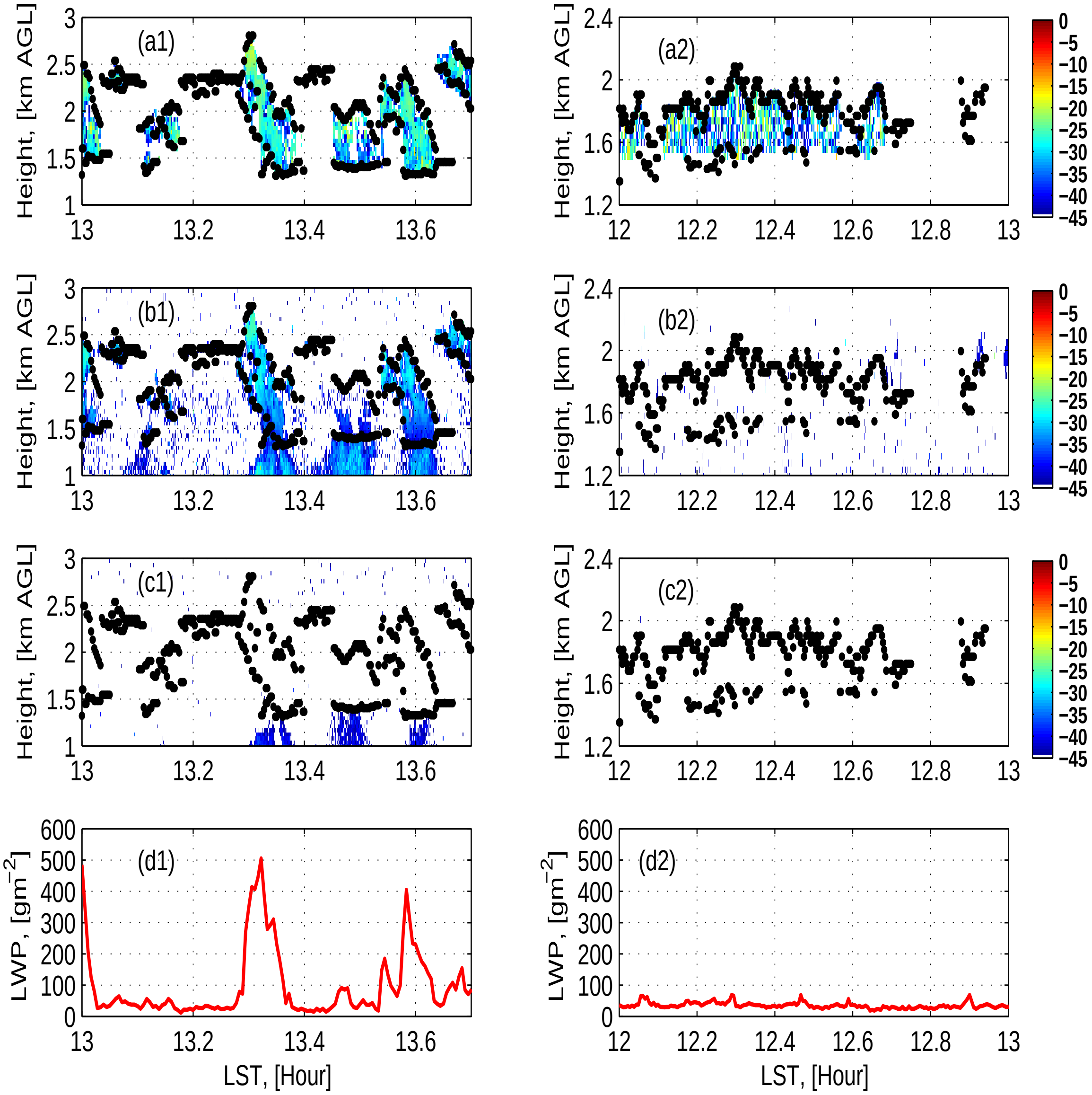

Figure 2–3: Sample cases showing the dominant cloud and insect echoes (right and left panels) from 35 and 94 GHz systems. a1(a2) ARSCL reported Reflectivity (dBZ). b1(b2) WACR Co-poloralization Reflectivity (dBZ). c1(c2) WACR Cross-polarization Reflectivity (dBZ). and d1(d2) LWP values from the Microwave radiometer.

computational resources required limit the application of the aforementioned technique to the present dataset. Therefore, a new approach is required. A new method based on fuzzy-logic (hereafter FL) technique is developed to separate insects from cloud echoes. A flowchart showing the sequence of steps used in FL algorithm to separate insects from cloud echoes is shown in Fig. 2-4.

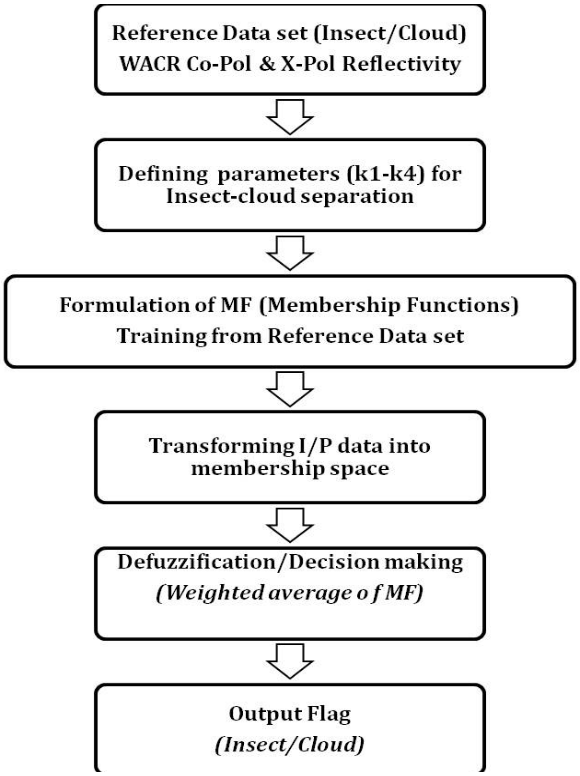

Figure 2–4: Flowchart showing the sequence of steps used in fuzzy-logic algorithm for separating insect echoes from cloud echoes.

The WACR dataset is used as a reference to choose the test cases containing insect and cloud echoes. Careful analysis of the MMCR observations indicated that there are several variables that have the potential to assist in the discrimination of insect and cloud echoes above the ceilometer-derived cloud bases. Such variables are: i) the observed LWP time series from the MWR, ii) the ratio of the LWP to the square of the reported cloud thickness from the ceilometer-derived cloud base height and MMCR derived cloud top height iii) the local variability of the MMCR reflectivity and iv) the observed Doppler spectrum width. During insect contaminated MMCR echoes above the ceilometer base, the LWP values are either at the MWR sensitivity level (30-50 gm^{-2}) or exhibit very small increase that indicates that the cloud echoes are not detectable by the MMCR. Similarly, the ratio of the observed LWP to the square of the MMCR echo thickness is very small in insect contaminated layers and higher for layers that contain significant liquid. Furthermore, the reflectivity texture of insect echoes is very spotty compared to the cloud echoes that results in higher variability in reflectivity field and the observed MMCR Doppler spectrum width values from insects are very small ($\sim$ 0.1 ms^{-1}) compared to these reported in cloud layers (e.g., Luke 2008). Using test cases from WACR dataset, the range of variability in each variable for insect and cloud cases are used formulate the membership functions (MF: it is a curve that defines how each value in the input space is mapped between 0 and 1 depending on its value in insect/cloud regime) as shown in Fig. 2-5. Subplots 2-5a-d corresponds to standard deviation of reflectivity (MF1) values, median of spectral width values (MF2), liquid water path (MF3) and the ratio of liquid water path (from MWR) to the cloud thickness (MF4) at each gate with surrounding 9 grid points. Here, the FL technique is applied to the radar echoes only when there is a valid cloud base from the ceilometer for a more conservative approach. Different weighting factors are assigned to the membership functions based on their individual performance to separate insects from cloud echoes.

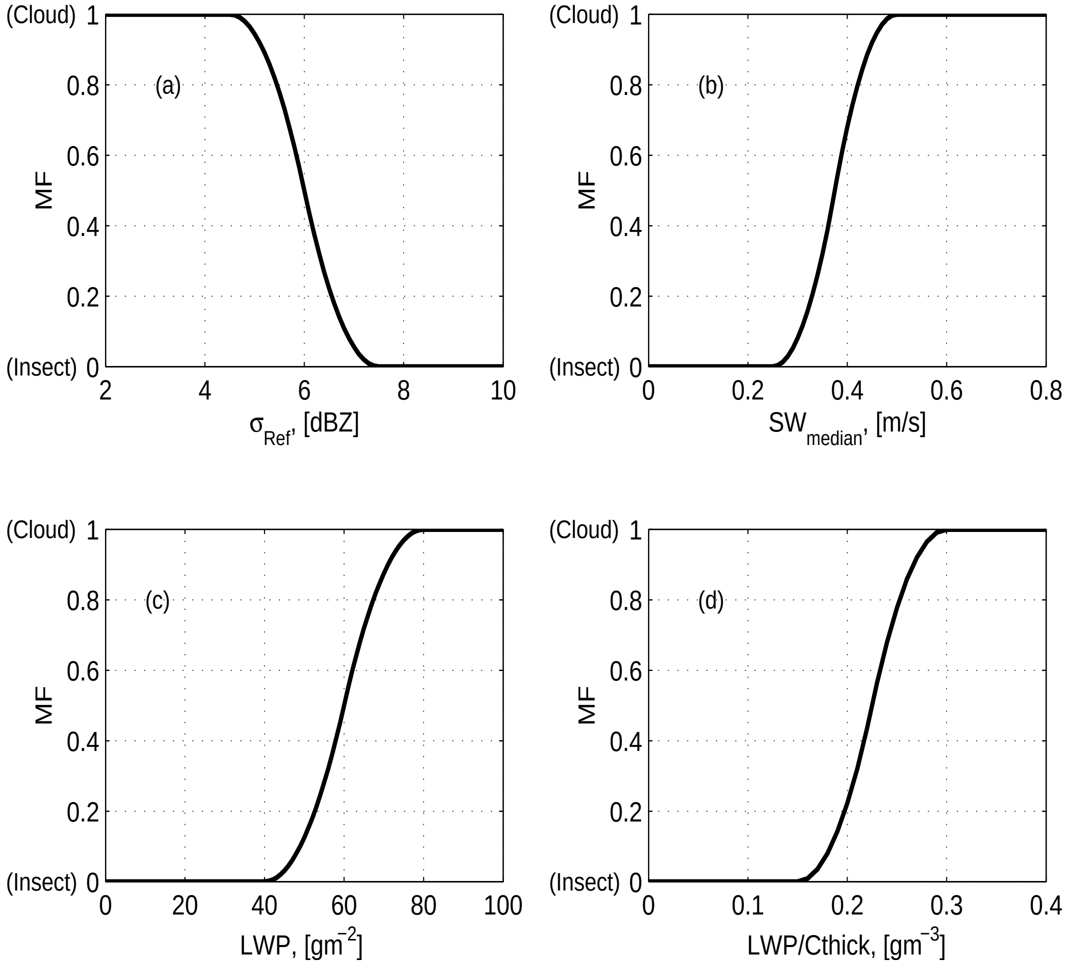

Figure 2–5: Graphs showing the MF for each decision parameter. a) Standard deviation of reflectivity values. b) Median of spectral width values, c) Liquid water path, and d) Ratio of liquid water path to cloud thickness

The combination of these parameters is used in FL algorithm to flag insect/cloud regime by assigning different weights (0.8 for MF1, 1.0 for MF2, 1.2 for MF3 and 1.3 for MF4) for membership functions. The output decision flag (Insect/Cloud) is calculated based on the weighted average of the membership values. The generalization of FL algorithm may be restricted to particular frequency radar (in our case Ka-band), but the methodology adopted here can be applicable to other systems. Figure 2-6 shows the comparison of output flags (cloud/insects) reported in ARSCL and FL for the cases showcased in Fig. 2-3. It can be observed that there is a misclassification of pure cloud echoes being reported as cloud and insects (as in panel a1) and insect echoes being reported as pure cloud echoes (as in panel a2) from ARSCL quality control. Thus this sets a necessity for an additional screening to process MMCR data. It is to be noted that there were no flags reported for most of the grid points in panel (b2). This is because, the FL algorithm needs a finite number of continuous MMCR profiles (3) in order to estimate the membership parameters and thus assign a insect/hydrometeor flag. When we actually zoom-in the right panel, the cloud bases are very sparse and wherever there are continuous cloud bases, algorithm computed the flags.

On applying FL algorithm, the percentage of data containing insect echoes are quantified as a function of daytime hours and summer months. The volumetric insect fraction (defined as the fraction of the number of radar gates with insect contamination to the total number of radar gates inside the cloud in an hour) values are high (with maximum values between 40-65%) between late morning to noon hours with fractional occurrences between 20-30 %. On monthly basis, the volumetric insect fraction values are high (with maximum values between 45-65%) during the month of May and June with fractional occurrences between 20-30 %. The FL algorithm is applied to the entire 14 years of the MMCR dataset for calculating the vertical velocity statistics.

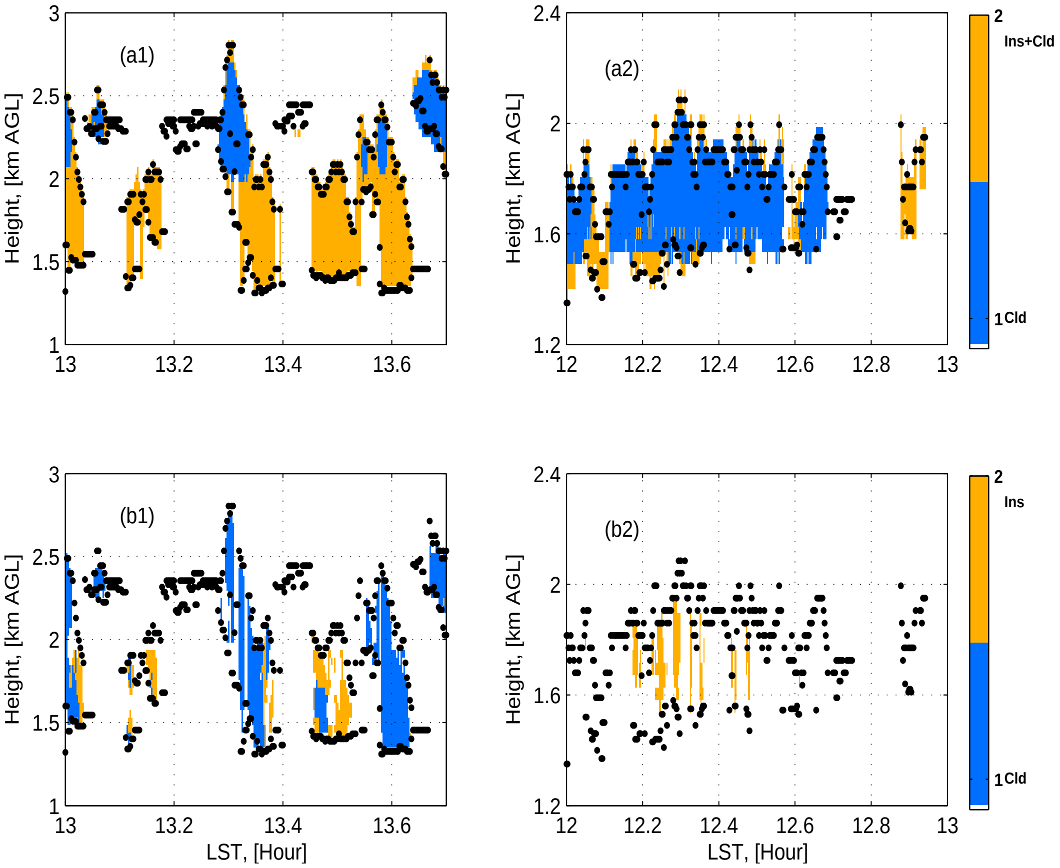

Figure 2–6: Two cases showing the ARSCL and Fuzzy-logic classification of insect and cloud echoes. a1(a2) ARSCL flag (1=pure cloud echoes, 2=Insect and cloud echoes). b1(b2) Fuzzy-logic flag (1=pure cloud, 2=Insects).

Figure 2-7 shows the differences in the cloud top variability as a function of volumetric insect fraction. It suggests that the echo layers with more insect contamination have lesser cloud top variability than the pure cloud echoes. Though this parameter can be used to discriminate the echoe layers with dominant insects versus cloud echoes, but the extent of insect contamination inside clouds cannot be quantified. Thus this parameter can be used to screen the insect layers from the cloud layers.

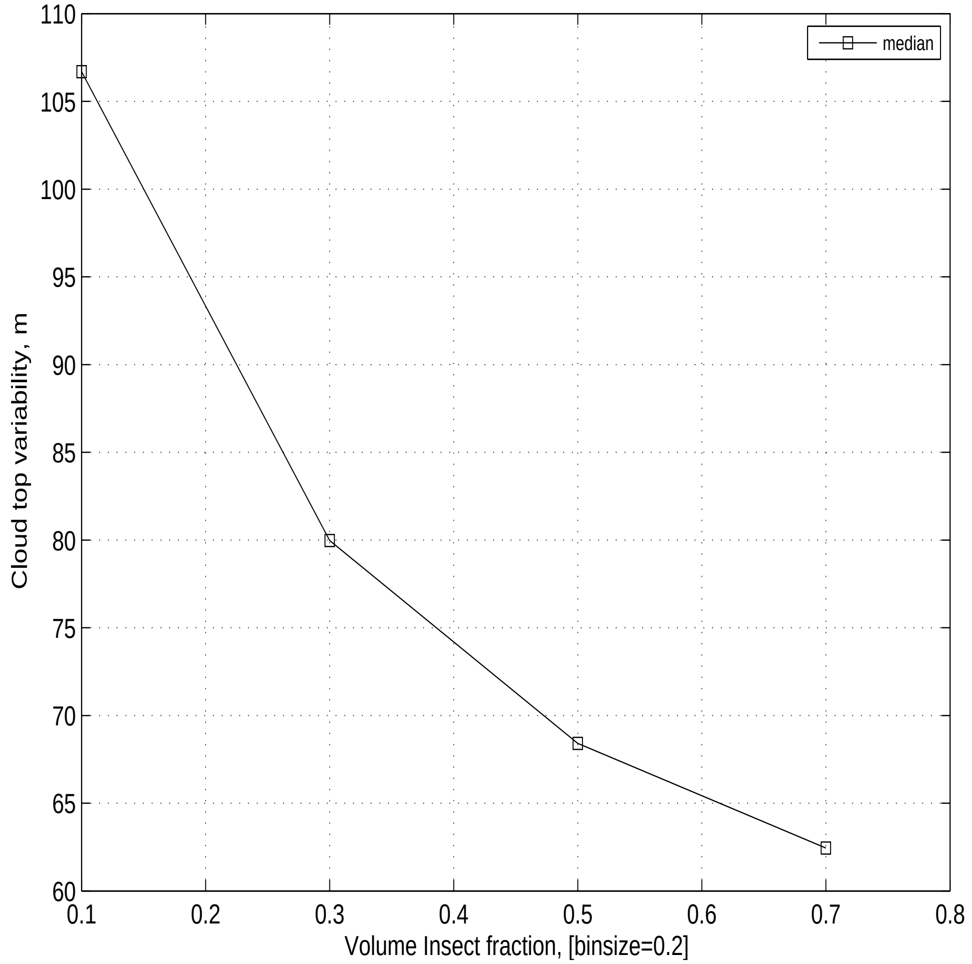

Figure 2–7: Plot of hourly volumetric insect fraction versus hourly cloud top standard deviations. Each point on the graph shows the median value of the cloud top standard deviation distribution for each insect fraction bin (bin size=0.2).

Table 2–1: List of Instruments along with with their specifications.

Instrument	*Resolution*	*Measurements*	*Accuracy*	*Remarks*
MMCR	10 sec, 45 m	Reflectivity Doppler velocity Spectrum width	0.5 dB 0.1 ms-1 0.1 ms-1	Vertically pointing -
WACR	$\sim$2 sec, 45 m	Reflectivity Doppler velocity Spectrum width	0.5 dB 0.1 ms-1 0.1 ms-1	Vertically pointing -
MWR	$\sim$20 sec	Brightness temp Liquid water path	0.3 k $\sim$ 3 gm^{-2}	Vertically pointing
Radio-Sounding	every 6 hours	Temperature Relative humidity Pressure Wind speed Wind direction	0.5 deg C $\sim$ 5% 0.05 kPa $\sim$0.5 ms^{-1} 10 deg	
Flux sensors	every 30 mins	Sensible heat flux Latent heat flux	10 % uncertainty 10 % uncertainty	
TSI	30 sec	Hemisp.Sky.Image Fractional sky cover		Reliable when solar.elev.>10 deg
Ceilometer pointing	$\sim$2 sec,10 m	Cloud base	50–75 m	Vertically
Doppler Lidar	2 sec, 30 m	Atten.Backscatter Doppler velocity	 0.1 ms^{-1}	Vertically pointing -
RWP	$\sim$10 min, 60/240 m	SNR Hor. winds and dir	0.5 dB 0.5 ms^{-1}, 3 deg	Vertically pointing

CHAPTER 3
Turbulent Structure of Convective Boundary Layer at the ARM Southern Great Plains Facility

3.1 Introduction

Echoes from nonhydrometeor targets including insects have been reported within many low-altitude radar observations, both in clear and cloudy boundary layers (e.g., Richter et al. 1973; Reynolds and Reynolds 2008; Achtemeier 1991; Russell and Wilson 1997; Wood et al. 2009). Cloud radar observations have been previously used in entomology to study flights of small insects because of the sensitivity of these systems to detect small insects (Riley 1992; Ka band, 35 GHz). According to the hypothesis tested and verified in **?** (hereafter GM05), these scatterers are subject to turbulent mixing in the CBL and tend to converge in the regions of sustained ascent, as these insects oppose any updrafts in which they embedded. At the SGP ACRF, insect–based MMCR echoes are regularly observed during the warm season (April-October). Using the ceilometer, rain gauge, TSI measurements, and reflectivity thresholds, one can verify that these returns do not originate from hydrometeors. The sample diurnal evolution of MMCR reflectivity and Doppler velocity due to insect echoes during shallow cumulus condition is shown in chapter 2(refer Fig. 2-1). In the Fig. 2-1, the cloud bases are associated with the high-reflectivity region and updraft motion beneath. The echo plumes are expected to represent coherent eddies of rising motion and in most of the fair-weather CBL, these echoes are believed to be small insects (∼10mm in flights; Miao et al. 2006). In a meteorological context, echoes from non–hydrometeor scatterers including insects should be removed from hydrometeor echoes from the millimeter wavelength cloud radar (MMCR) for the study of clouds. In the present study, a different approach is adopted to study CBL in long-term basis. Instead of removing the insect MMCR echo contribution to study clouds in the boundary layer, this study capitalizes on insect Doppler content to study the turbulent structure of the subcloud layer. Doppler signatures of insect echoes measured from cloud radar (95 GHz, 3 mm) were previously explored to study the characteristics of buoyant eddies within the CBL using 3 days of data during the International H2O Project (IHOP–2002; Miao et al. 2006). A correction is applied to the Doppler velocity based on Eq. (2) in GM05 to remove the downward bias. The detailed explanation regarding the correction is discussed in the methodology section. A more extensive set of corrected insect observations from Doppler radar is classified into clear and cloudy boundary layer (non-precipitating shallow cumulus) conditions, and composite profiles of vertical velocity variance, skewness, and updraft mass-flux ratio (ratio of updraft mass-flux contribution from coherent structures to the total mass flux, capitalizing on all upward values of the vertical velocity) are computed. In addition to the long-term MMCR data set, supplementary observations from the radar wind profiler (RWP), total sky imager (TSI), and tower observations are used to characterize the surface conditions and the top of the mixed layer.

3.2 Turbulent Statistics

Turbulence is the main efficient mode of energy transfer in the CBL. Turbulence influences wide range of scales [ranging from dissipation scales (mm) to BL scale (km)] encounter in the CBL. The evolution of the turbulent flow is highly complex and turbulent flows appear highly disorganized with structure and signals appear unpredictable in their detailed behavior. Its impossible to study detailed description at all scales. However, it is useful to seek the statistical description of turbulent flows. A statistical measure would be an average of some kind which satisfies some conditions. For e.g., flow is stationary (statistical properties doesn't vary with time) or an ensemble (statistics are constant over multiple realizations). A complete description of the turbulent variable v at a given instant and location is given by the probability density function (PDF). The moments of the variable v are derived from the PDF. The first moment $<v>$ is the mean:

$$< v > = \int_{-\infty}^{\infty} vP(v)dv \tag{3.1}$$

where P(v)dv is the probability of variable v taking a value between v and v+dv. The variance is the second moment of the perturbation quantity $v' = v - < v >$, it is the measure of variability about the mean.

$$< v^{'2} > = \int_{-\infty}^{\infty} (v - < v >)^2 P(v)dv \tag{3.2}$$

The skewness is the third moment of v', normalized by the variance:

$$skewness = \frac{< v^{'3} >}{< v^{'2} >^{3/2}} \tag{3.3}$$

The skewness reveals the information about the asymmetry of the PDF. Positive skewness indicates that the PDF has a longer tail for $v- < v > \ > 0$ than for $v- < v > < 0$.

3.3 Analysis

A total of 2894 h of observations over 4 yr (2004–08) of summer periods (May–September) was included in this analysis (Tables 3.1–3.4). The events are separated into clear-sky periods (1603 h) and cumulus-topped boundary layer periods (1291 h). The cumulus-topped cases are further classified with respect to cloud fraction as low (cloud fraction less than 20% of the hour, 412 h), moderate (cloud fraction between 20% and 60%, 516 h) and high (cloud fraction above 60%, 363 h). The data set is also classified according to the time of the day. An average profile at each hour for clear-sky (cumulus) days is computed independently from all the clear-sky (cumulus) days at this hour having clear-sky (cumulus cloud) conditions.

3.3.1 Bulk daytime observations of surface and CBL parameters

During cloud-free conditions, the mixed layer depth increases from 947 m between 1000 and 1100 local standard time (LST= CST=UTC–6 hr) to a maximum of 1654 m between 1600 and 1700 LST. In cumulus-topped conditions, the largest diurnal variability in the cloud-base height (CBH) is during low-cloud fraction conditions (1080–1730 m) and the smallest is during high-cloud fraction conditions (1154–1401 m). In general, the cloud-base height decreases with increasing cloud fraction. The surface buoyancy flux maximum is observed around 1200 LST and decreases from

275 Wm^{-2} during clearsky conditions to 233, 217, and 154 for low, moderate, and high cloud fraction conditions, respectively.

The convective velocity scale (Lenschow et al. 1980) in Tables (3-1 to 3-4) is defined as

$$w_* = (\frac{g}{T_v}\overline{w'T_v'h})^{1/3} \tag{3.4}$$

where g is the acceleration due to gravity, T_v is the virtual temperature, $\overline{w'T_v'}$ is the surface kinematic buoyancy flux, and h is the BLH. In (eqn.3.1), the kinematic buoyancy flux is provided directly from sonic measurements of w' and T_v'. The calculated convective-velocity scale maximum for clear-sky, low, and moderate cloud conditions is observed between 1200–1300 and 1300–1400 LST with values ranging from 1.65 to 2.23 ms^{-1}. The lowest convective-velocity-scale maximum (1.65 ms^{-1}) is observed during high-cloud fraction conditions. This can be attributed to the reduction in both surface buoyancy flux and boundary layer depth (Table 3-4). The maximum of the convective velocity scale is found close to the maximum of the surface kinematic buoyancy flux (Tables 3.1–3.4).

Table 3–1: Tabulated hourly values of boundary layer and surface properties during clear-sky conditions computed from the 4-yr data set.

$LST(hr)$	$10-11$	$11-12$	$12-13$	$13-14$	$14-15$	$15-16$	$16-17$
Clear-sky hours (total)	195	174	157	141	135	144	149
BLH, mean (m)	947	1167	1355	1501	1543	1598	1654
BLH, std.dev (m)	286	375	462	524	552	581	575
Convective velocity mean (ms^{-1})	1.81	1.96	2.03	2.02	1.89	1.81	1.80
Convective velocity std.dev (ms^{-1})	0.41	0.42	0.47	0.49	0.47	0.42	0.46
Sfc.buoyancy flux, mean (Wm^{-2})	231	267	275	271	239	193	131
Sfc.buoyancy flux, std.dev (Wm^{-2})	77	81	85	80	83	80	63

In addition to the surface conditions, the daytime evolution of the BLH is documented using the RWP returns. The hourly based estimates of the BLH are used to scale the profiles of vertical velocity statistics. The averaged insect layer top and the BLH for both clear-sky and cumulus-topped conditions are shown in Fig. 3-2. During clear-sky conditions, the BLH rises from 0.95 km (1000–1100 LST) to 1.65 km (1600–1700 LST). During cumulus-topped conditions, BLH values of low-cloud fraction conditions are higher compared to under clear–sky, medium, and high-cloud fraction conditions during afternoon, but they are nearly comparable before noon. In clear-sky days, the insect layer jump is higher than the growing mixed layer early in the morning (in conjunction with the development of daytime convection) similar to the observations of Wood et al. (2009), but it remains very close to the BLH after 1200 LST. In cumulus-topped conditions, the insect-layer-top estimate remains slightly above the BLH during morning times; during the afternoon, the estimate is slightly lower than the BLH. This is consistent with previous studies of insects at the SGP ACRF (Luke 2008).

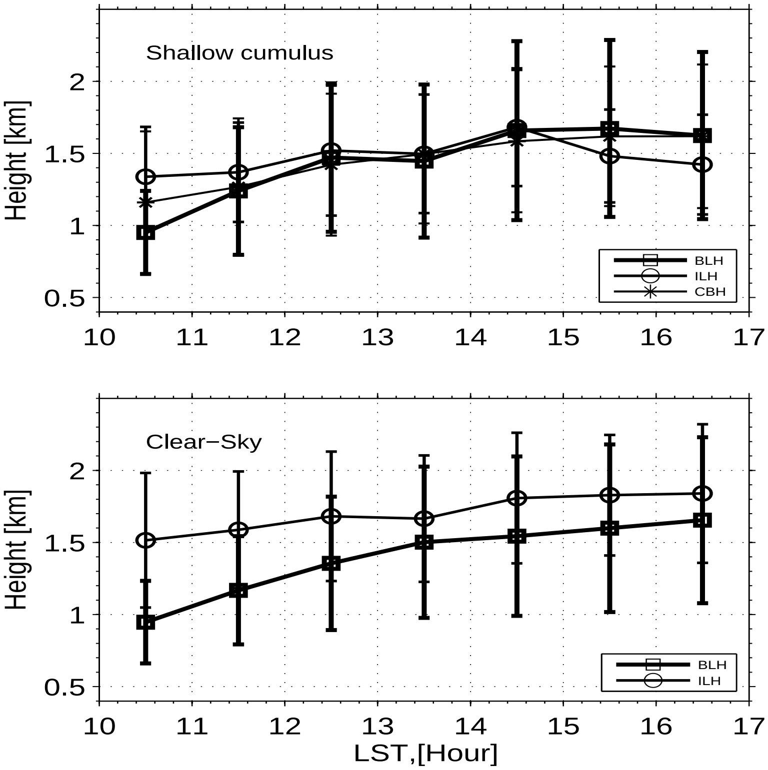

Figure 3–1: (top) Daytime evolution of BLH, ILH, and CBH for cumulus-topped condition. (bottom) Daytime evolution of the BLH and ILH for clear-sky condition. Symbols in both panels indicate the mean observed height from all events (clear or cumulus topped) for the same hours. Bars indicate the plus or minus std dev of the hourly averaged values.

3.3.2 Vertical velocity variance

Profiles of vertical velocity variance and skewness have been frequently explored to characterize convective conditions and the source of turbulent kinetic energy (TKE) in the boundary layer (e.g., Lemone 1980; Moyer and Young 1991; Hogan et al. 2009). These profiles are often scaled with the boundary layer height (zi) to provide nondimensional vertical coordinates for the daytime turbulent statistics in the planetary boundary layer (e.g., Lenschow et al. 1980; Young 1988). As in the previous sections, during both clear-sky and cloudy conditions, the BLH deduced by the RWP is used to scale the vertical coordinate. For each hour of observations and at each MMCR range gate from the surface to the top of the insect layer, the variance of the vertical air motion ($\overline{w'^2}$) is calculated based on the time series of corrected MMCR mean Doppler velocity measurements. The variance values are normalized by the convective velocity scale (w*).

The daytime evolution of the normalized vertical velocity variance profile for cloudy and clear-sky conditions is shown in Fig. 3-3. For each hour, and separately for cloudy and clear periods, the mean of the hourly estimated normalized vertical velocity variance is shown. In addition, the measurements of normalized vertical velocity variance collected by aircraft (Nicholls and Lemone 1980) and Doppler lidar (Hogan et al. 2009) are also shown for comparison. The mean normalized vertical velocity profiles collected using the insect radar returns are smooth because of the large number of hours included in the analysis and are limited to the depth z/zi ; 0.8 to ensure the filtering of erroneous values due to the scarcity of MMCR insect echoes up to zi for all the days considered in the averaging. In addition to the mean, the standard deviation (std. dev.) of the hourly values is estimated to provide a measure of the one-day-to-another variability for the same hourly period. The height averaged standard deviation of the reported values for the cumulus-topped and clear-sky conditions is 0.49 and $0.54 ms^{-1}$, respectively; and the spread (change) of the standard deviation values with height for the cumulus–topped and clear-sky conditions is 0.08 and 0.09, respectively (Fig. 3-3). In both clear and cloudy conditions, a gradual increase in the magnitude of the normalized variance is observed with time. The maximum values are observed between 1400 and 1600 LST. In the vertical profile, the maximum variance is observed between 0.2 and 0.4 in normalized height, which is consistent with the asymmetric profile of Lenschow et al. 1980 fitted to the observations and the previous LESs (e.g., Schmidt and Schumann 1989; Shen and Leclerc 1995) and slightly lower compared to the observations of Nicholls and Lemone 1980. The difference may also be attributed to the differences in the spatial extent of the surface inhomogeneities. Above the variance maximum, the normalized variance profiles decrease with height. This observation is consistent with a well-mixed boundary layer, where forcing is provided from the bottom (surface) in the form of surface heat flux (Garratt 1994). Clear-sky days exhibit relatively higher normalized variance values compared to cloudy days. Overall, the observed magnitudes are higher than these observed by Nicholls and Lemone 1980 and Hogan et al. 2009, especially during clear-sky periods. The observed differences can be attributed first to the fact that the observed profiles by Nicholls and Lemone 1980 and Hogan et al. 2009 are derived by a small sample of data and under different conditions, and second to the sensitivity of the vertical velocity variance to the GM05 correction.

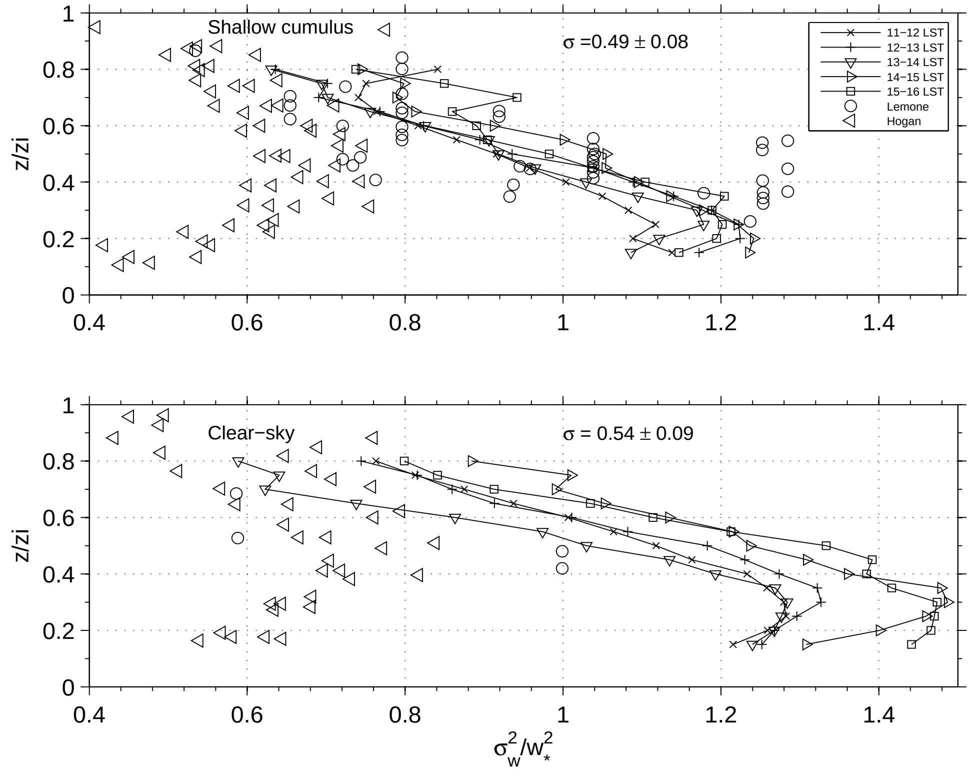

Figure 3–2: Top(bottom) panel: Daytime evolution of normalized vertical velocity variance profiles during cumulus-topped (clear-sky) conditions. Profiles for each hour are computed from all the cumulus (clear-sky) hours at this hour from 4 yr data set. In the Figure legends, mean represents the average std dev and ± indicates the minumum and maximum value of the std dev.

GM05 used a linear relationship with a 1.92 slope to correct the observed Doppler velocities for insect motion. The variance of the vertical velocity increases with the square of the slope. The variance is the only result presented in this study that is sensitive to the insect motion correction. Nevertheless, the vertical velocity data contain rich information with respect to the vertical structure and the daytime evolution of the normalized variance. During clear-sky periods, there is a systematic shift toward higher value with daytime. This is not clear in the cloudy periods and it is attributed to the averaging of hours with different cloud fraction amount. The impact of increased cloudiness at the top of the CBL in the observed profile of normalized variance is shown (Fig. 3-5, top panel). The hourly-estimated normalized variance profiles are classified and averaged with respect to the observed cloudiness for clear-sky, low-, medium-, and high-cloud fraction conditions. The composite averages indicate that an increase in cloudiness is associated with higher normalized variance (compared to low- and medium-cloud fraction conditions). Furthermore, in high-cloud fraction conditions, the normalized variance profile reverses its decreasing trend near the upper part of the CBL. This implies a source of turbulence near the top of CBL driven by increased cloudiness.

3.3.3 Vertical velocity skewness

In addition to the normalized variance, the hourly profiles of vertical velocity skewness are estimated using the corrected MMCR Doppler velocities for both clear and cloudy periods.The sign and magnitude of the skewness are driven by asymmetries in the distribution of vertical velocities in a particular height. Positive (negative) skewness indicates the presence of a few narrow strong updrafts (downdrafts) in our observations. In a surface-driven well–mixed boundary layer, one expects the skewness to be positive and increasing with height; in a top-driven boundary layer, one expects the skewness to be negative at the top (e.g., Moyer and Young 1991).

The composite profiles of vertical velocity skewness and their daytime evolution for cloud-topped and clearsky conditions as a function of the normalized z_i are shown in Fig. 3-4. For comparison, the aircraft measurements from Nicholls and Lemone

(1980) and lidar measurements from Hogan et al. (2009) are shown in the same Figure. The limited data set (covering only few days) from aircraft and Doppler lidar observations exhibits great scatter with no evident vertical structure, and it covers the range of the observed values using the insect radar returns. The composite profiles exhibit a smooth vertical structure. This is attributed to the long data set used in this study. Despite the smooth vertical structure, on average, the day-to-another-day standard deviation of the observed skewness values is high: 0.51 and 0.38 for cloudy and clear-sky conditions, respectively. During clear-sky conditions, skewness values are positive with magnitudes ranging from 0.1 to 0.4. This is consistent with a surface-driven boundary layer. Near the surface ($z/zi<0.25$) and the upper part ($z/zi>0.7$) of the CBL, we observe the lowest values (0.1–0.25), while the middle part of the CBL exhibits the higher positive values of skewness without a noticeable daytime progression. During cloud-topped conditions, we observed both positive and negative skewness values. The lowest values of skewness are observed before noon (1100–1200 LST) and during late afternoon (1500-1600 LST), while the highest (positive) values are observed between 1200 and 1500 LST. The skewness remains positive in the lower two-thirds of the CBL and negative in the upper part of the CBL. This is a clear difference compared to the clear-sky profiles, and it is another indicator of the effect of clouds in the subcloud layer turbulent kinetic energy budget.

Once again, the effect of increased cloudiness on the vertical velocity skewness profiles is studied by partitioning the hourly estimated skewness profiles with respect to the cloud fraction (Fig. 3-5, bottom panel). Overall, increased cloudiness results in lower magnitudes of positive skewness. A transition to negative skewness values

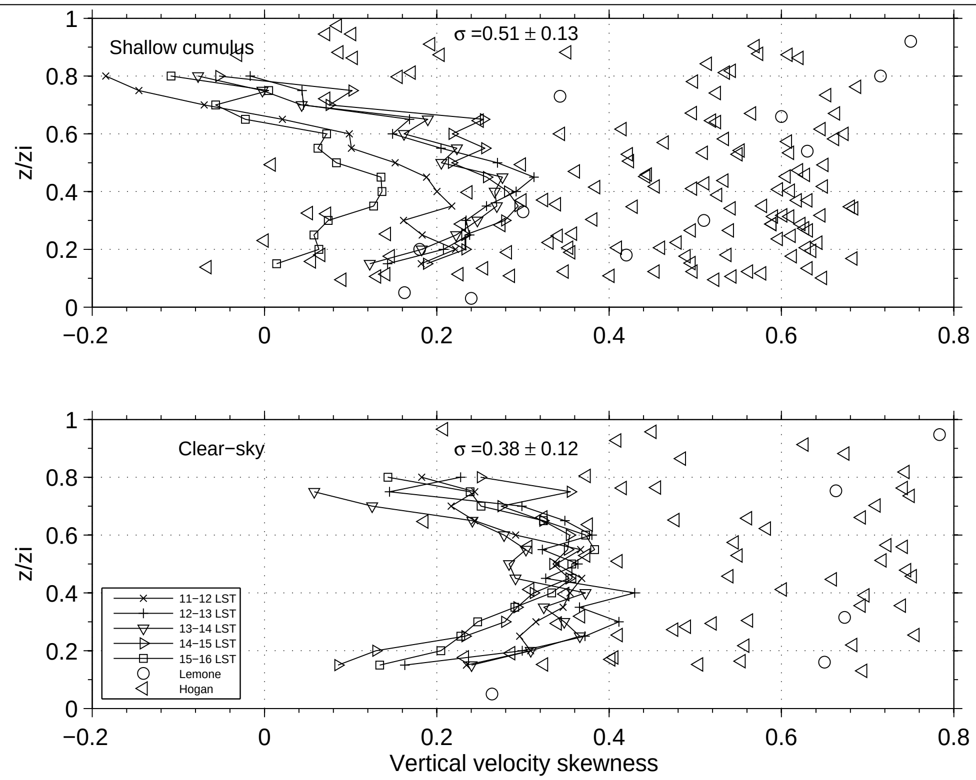

Figure 3–3: Top(bottom) panel: Daytime evolution of vertical velocity skewness profiles during cumulus-topped (clear-sky) conditions. Profiles for each hour are computed from all the cumulus (clear-sky) hours at this hour from 4 yr data set.

in the CBL occurs at middle and high-cloud fractions at levels higher than $\frac{z}{z_i}$>0.7 and $\frac{z}{z_i}$>0.5 respectively. It is evident that skewness, a higher-moment statistic of the vertical velocity field than variance, shows the effect of clouds in the subcloud layer and the turbulent budget in the upper part of the CBL (e.g., Moeng and Rotunno 1990).

3.3.4 Conditional sampling of coherent vertical velocity structures

LES models are developed upon the hypothesis that these models have sufficient resolution to resolve the length of eddies that are responsible for most of the turbulent

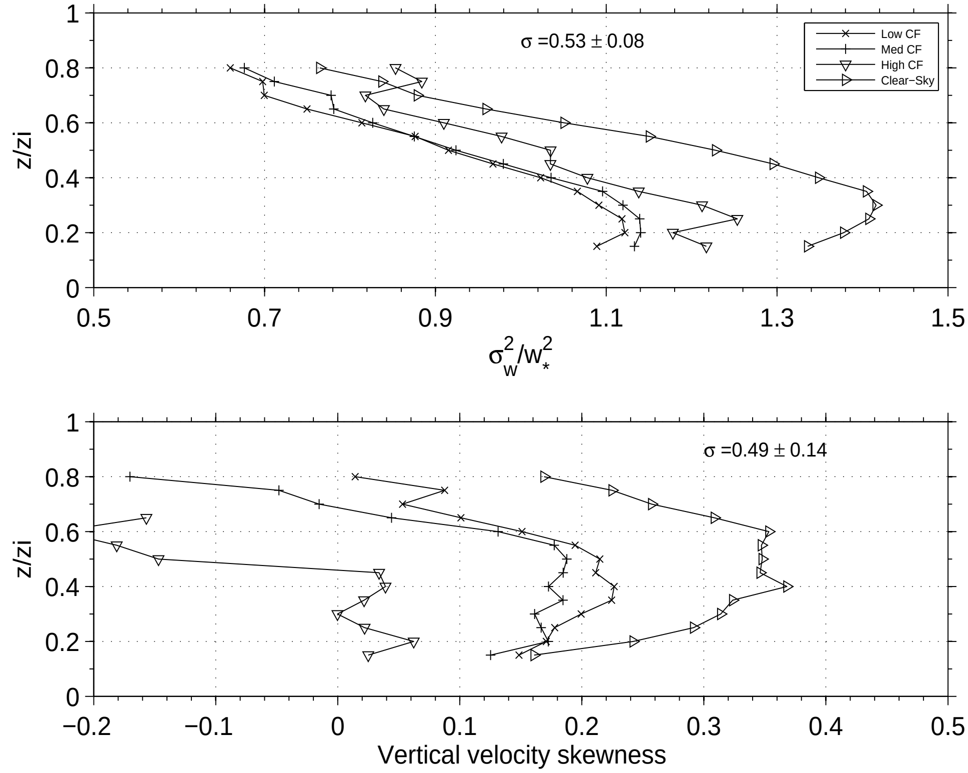

Figure 3–4: Classification of profiles of normalized vertical velocity variance (top) and vertical velocity skewness (bottom) during clear and cumulus conditions for three different CF (cloud fraction) regimes. Low CF: CF less than 0.2; moderate CF: CF between 0.2 and 0.6 and High CF: CF more than 0.6.

transport in the boundary layer. One of the main objectives of this study is to examine to what extent the turbulent transport in the CBL is performed by large coherent eddies and to investigate the corresponding spatial dimensions of these plumes. Both tasks require the detection of coherent vertical velocity structures (plumes) using an objective conditional sampling (e.g., Greenhut and Khalsa 1987; Khalsa and Greenhut 1987; Kollias and Albrecht 2000; Williams and Hacker 1992). If statistics involving dimensions of coherent structures are required, then attention is to be given to the effects of small-scale turbulence embedded within the identified structures and their environment (e.g., Williams and Hacker 1992).

MMCR observations are provided in time and height. Time is converted to horizontal distance using the hourly consensus estimates of the horizontal wind magnitude from the RWP. To avoid the short time, large-amplitude fluctuations that manifest in the data as coherent structures (e.g., Williams and Hacker 1992), a minimum physical width (horizontal dimension) of 300 m is required for the detection of a coherent velocity structure (plume). In addition, a minimum vertical extent of 225 m (five MMCR range gates) is set. Thus, a coherent updraft and downdraft structure is an area with a minimum size of 225 X 300 m where all Doppler velocity perturbations are positive and negative, respectively. Higher updraft velocity magnitudes (0.3-1.0 ms^{-1}) are used to identify more intense plumes. Once the area (time, height) covered with plumes is detected, the widths of updraft and downdraft regions are recorded and are normalized by the boundary layer height (BLH; estimates of these heights are given in chapter 2). Best-fit exponential curves are fitted to the distributions of observed plume widths for updraft and downdraft structures and half-widths (distance at which the best-fit exponential curve attains 0.5 times the smallest resolvable scale) are recorded as a measure of the median width in the observed distributions (e.g., as in Miao et al. 2006). Similarly, the plume contribution to the mass flux is estimated for different velocity thresholds (here, a velocity threshold of 0 ms^{-1} is assumed).

3.3.5 Plume dimensions and updraft mass-flux profiles

Conditional sampling (above section) was applied on the vertical velocity field to extract the physical dimensions of coherent updraft and downdraft structures and to estimate their contribution to the total updraft mass flux. The observed updraft and downdraft half-widths cover the range between 0.49 and 0.83 (Table 3-5). During clear-sky conditions, half-width values for updrafts (downdrafts) are at a maximum 0.73 (0.80) early in the day (1000–1100 LST) and a minimum 0.49 (0.6) in late afternoon (1600–1700 LST). Similarly, during cloud conditions, the half-width values for updrafts (downdrafts) are at a maximum 0.81 (0.83) early (1000–1100 LST) and a minimum 0.53 (0.51) in late afternoon (1600–1700 LST). During cloud-topped conditions, no clear trend is observed between updraft and downdraft half-widths. The statistics of the width of the updraft structures change little when the velocity threshold for the plumes increased from 0 to 0.6 ms^{-1} (only the threshold of 0 ms^{-1} is shown in Table 3-5), indicating the velocity strength in the updraft plumes. Similar results are found for downdraft half-widths.

The updraft mass flux is calculated using both direct and a conditional sampling method. Here, the direct method estimates the total updraft mass flux using all the available upward MMCR velocities at each MMCR range gate for every hour. Thus, in this direct approach, all upward MMCR Doppler velocity points contribute to the updraft mass-flux calculation. Moreover, this calculation does not discriminate as to whether these measurements are associated with an updraft plume.

The conditional sampling method estimates the updraft mass flux from observations that have an upward MMCR velocity and are also part of a coherent updraft plume according to the criteria outlined in section 3b. In the conditional sampling method, not all MMCR upward velocity observations contribute to the estimated mass flux (e.g., Kollias and Albrecht 2000). The updraft mass flux estimated using conditional sampling is usually less than the updraft mass flux estimated using direct sampling. The two estimates are equal only in the extreme case of a coherent vertical velocity field (e.g., sinusoidal wave). The ratio of the two estimates of updraft mass flux (conditional to direct) indicates the percent of turbulent transport in the boundary layer from coherent plumes (large eddies). The shape of mass-flux profiles of both total mass flux and mass flux from coherent structures (not shown) was similar to the normalized variance profiles with a maximum located between $\frac{z}{z_i}$=0.2 and 0.4 and decreases thereafter. This is consistent with the findings of Nicholls and Lemone (1980). On average, the updraft mass–flux magnitudes calculated during cumulus-topped periods are smaller than these observed during clear-sky periods (not shown).

The daytime evolution of the updraft mass-flux conditional-to-direct method ratio during clear-sky and cumulus-topped conditions is shown in Fig. 3-6. Overall, coherent structures are responsible for more than 80% of the turbulent transport, and the standard deviation of this estimate from one day to another is only 7%. This is a significant finding that validates mass-flux-based parameterizations of the turbulent transport in the CBL and the use of LES models (e.g., Couvreux et al. 2010) for modeling boundary layer processes. The maximum of the updraft mass-flux ratio occurs at $\frac{z}{z_i}$=0.3 and then decreases with normalized height to reach their lowest value at the maximum height of our observations ($\frac{z}{z_i}$=∼0.85). No daytime progression of the updraft mass-flux ratio is observed. The shape of the mass-flux profiles during cumulus-topped conditions is similar to the profiles observed for clear skies, except there is a lower mass-flux ratio during later morning (1100-1200 LST) because of relatively small total mass-flux transport. The maximum updraft mass flux is observed at $\frac{z}{z_i}$=0.3, similar to the clear-sky condition.

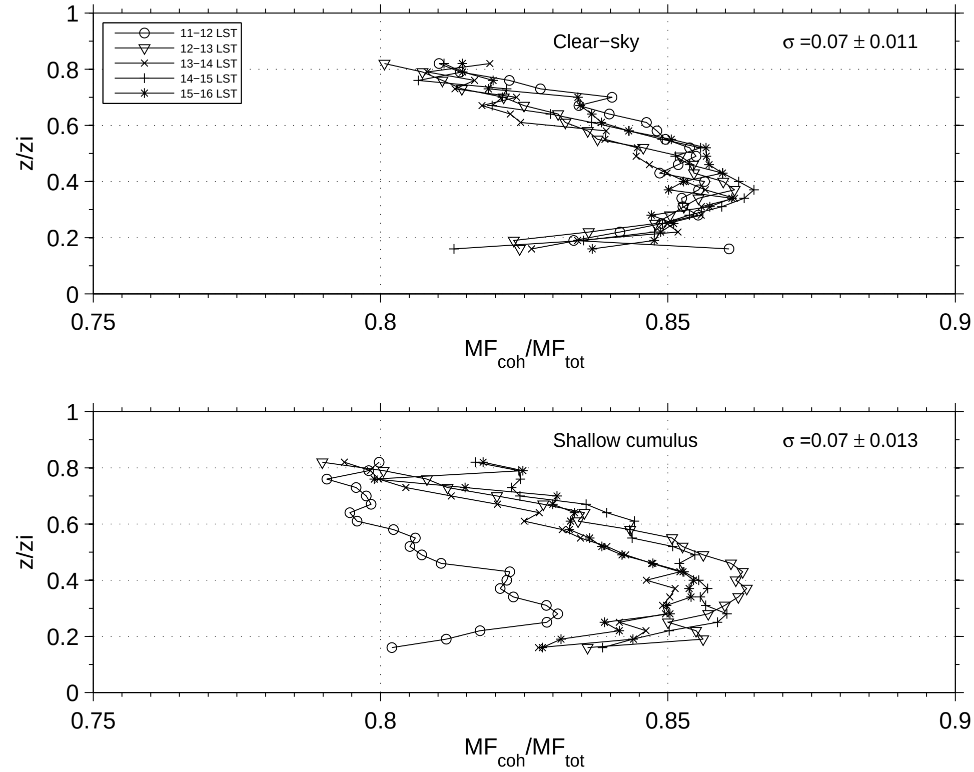

Figure 3–5: Top(bottom) panel: Profiles of mass-flux ratio for different time of the day during clear-sky(cumulus) conditions.

The effect of cloudiness in the observed updraft mass–flux ratio in the subcloud layer is shown in Fig. 3-7. During high-cloud fraction conditions, the mass-flux ratio is relatively lower compare to other cloud fraction regimes and clear-sky conditions above $\frac{z}{z_i}$=0.3. Another observed feature is that the mass–flux ratio during clear-sky conditions is lower than during the low and medium-cloud fraction condition.

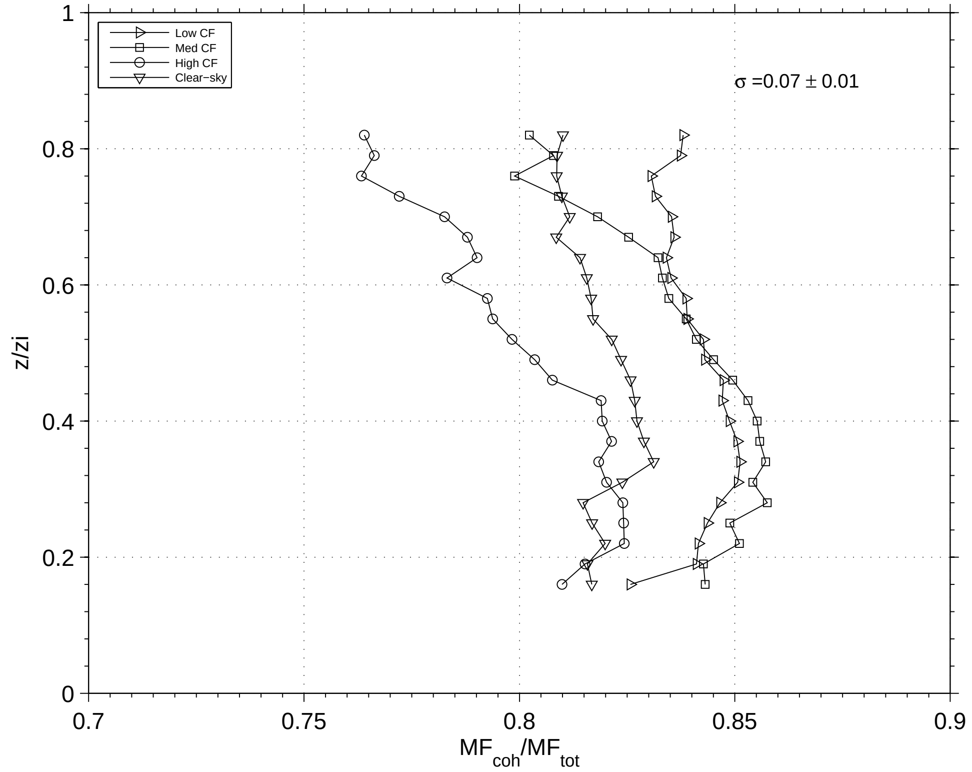

Figure 3–6: Classification of profiles of mass-flux ratio for different CF conditions as in Figure 3-5

3.4 Summary

Insect radar returns at the SGP ACRF have been long considered a nuisance for efforts to use ground-based vertically pointing radars to detect and study boundary layer clouds. In this study, a different approach is adopted wherein the insect radar returns from vertically pointing Doppler cloud radar are used to monitor the properties of boundary layer turbulence. The study makes use of a multi–year summer data set from millimeter-wavelength cloud radar, a 915-MHz wind profiler, and flux-measuring sensors at the surface. The Doppler velocity measurements from insects were corrected for insect motion using the GM05 formula. A clear strength of this study is the use of a large data set of four consecutive warm seasons of vertical velocity observations at the SGP ACRF. The large data set facilitates acquiring smoothed vertical structures of turbulence statistics and documenting their diurnal evolution. The large data set (2894 h of daytime CBL observations) is classified into clear-sky and cumulus-topped conditions. During both clear-sky and cumulus-topped conditions, the 915-MHz wind profiler signal-to-noise ratio (SNR) is used to develop an automated algorithm for the detection of the mixed layer top. The daytime evolution of the boundary layer is studied using the profiles of vertical velocity variance, skewness, and mass-flux ratio.

The normalized vertical velocity variance profiles exhibit a smooth daytime evolution with the maximum turbulent activity observed between 1400 and 1500 LST. During clear-sky conditions, the maximum in normalized variance is observed around $\frac{z}{z_i}$=0.3. This is in agreement with previous aircraft observations for surface driven turbulence. The magnitude of the variance is relatively higher during clear-sky conditions as compared to cumulus-topped conditions; this is consistent with previous observations (e.g., Lenschow et al. 1980; Lenschow and Stephens 1980). Evidence for the effect of clouds in the subcloud layer turbulence budget is found in the vertical structure of the normalized variance for high-cloud fraction conditions. The vertical velocity skewness during clear-sky conditions is positive and higher compared to cumulus-topped conditions. During cumulus-topped conditions, negative skewness is observed near the top of the subcloud layer, indicating the interaction between the subcloud layer and cloud layer. Using an objective conditional sampling method, coherent vertical velocity structures in the boundary layer are identified. The observed normalized updraft and downdraft half–width values vary from 0.8 (prenoon hours) to 0.5 (late-afternoon hours). The reported normalized half-width values are dominated by the presence of numerous plumes with small horizontal width that do not scale with the BLH increase throughout the day. However, when the detail hourly normalized half-width distributions are viewed (not presented here), we do see a number of individual plumes with normalized half-width near or higher than the BLH. Updraft mass-flux calculations using a direct sampling technique and the conditional sampling technique suggest that coherent structures (plumes) are responsible for more than 80% of the total turbulent transport observed by the radar in the boundary layer during clear-sky and cumulus-topped conditions.

Overall, the characterization of the boundary layer turbulence using insect radar returns is consistent with previous studies (e.g., Lenschow et al. 1980; Lenschow and Stephens 1980). The cloud radar observations provided a unique daytime evolution of the convective boundary layer and indicate the role of increased cloudiness in the turbulent budget of the subcloud layer. The large SGP MMCR data set makes the observations suitable for evaluating boundary layer parameterizations for a variety of surface and cloud conditions. The basic analysis of the data provided in this paper gives support to using the cloud radar data in a number of different studies of greater complexity (a variety of surface and cloudy conditions). It is more straightforward to think of using these observations to test LESs. The study also provides the observational evidence to assess the boundary layer parameterizations by including the behavior of CBL statistics under different conditions.

Table 3–2: Tabulated hourly values of boundary layer and surface properties during cloudy conditions with low CF (below 20 % cumulus conditions).

$LST(hr)$	$10-11$	$11-12$	$12-13$	$13-14$	$14-15$	$15-16$	$16-17$
Cumulus-topped hours (total)	38	40	41	57	64	52	49
Cloud coverage, mean (%)	7.5	7.6	9.8	8.4	9.3	10	9.7
Cloud coverage, std.dev (%)	5.9	5	6.1	5.4	6.3	5.4	6.3
Cloud base, mean (m)	1108	1259	1563	1710	1664	1730	1712
Cloud base, std.dev (m)	489	484	577	527	545	482	507
Sfc.buoyancy flux, mean (Wm^{-2})	162	183	195	225	210	164	107
Sfc.buoyancy flux, std dev (Wm^{-2})	87	117	106	107	103	88	64
Convective velocity mean (ms^{-1})	1.73	2.02	2.0	2.23	1.99	1.79	1.60
Convective velocity std.dev (ms^{-1})	0.63	0.79	0.45	0.59	0.48	0.45	0.45
BLH mean (m)	962	1261	1467	1601	1713	1888	1707
BLH std.dev(m)	245	474	560	527	588	415	550

Table 3–3: Tabulated hourly values of boundary layer and surface properties during cloudy conditions with moderate CF (20−60%)cumulus conditions).

$LST(hr)$	$10-11$	$11-12$	$12-13$	$13-14$	$14-15$	$15-16$	$16-17$
Cumulus-topped hours (total)	47	59	54	67	68	68	48
Cloud coverage, mean (%)	39	38.8	37.6	40.1	37.5	35.7	37.3
Cloud coverage, std.dev (%)	10.5	10.9	11.1	11.9	11.9	11.8	11
Cloud base, mean (m)	1225	1360	1524	1447	1684	1621	1623
Cloud base, std.dev (m)	569	513	458	425	414	488	439
Sfc.buoyancy flux, mean (Wm^{-2})	153	183	217	213	190	155	108
Sfc.buoyancy flux, std dev (Wm^{-2})	96	91	96	88	84	77	67
Convective velocity mean (ms^{-1})	1.78	1.75	2.05	1.95	1.87	1.72	1.69
Convective velocity std.dev (ms^{-1})	0.72	0.51	0.53	0.45	0.43	0.51	0.57
BLH mean (m)	991	1233	1612	1420	1677	1618	1615
BLH std dev(m)	311	452	500	501	607	643	547

Table 3–4: Tabulated hourly values of boundary layer and surface properties during cloudy conditions with high CF (above 60%)cumulus conditions).

$LST(hr)$	$10-11$	$11-12$	$12-13$	$13-14$	$14-15$	$15-16$	$16-17$
Cumulus-topped hours (total)	42	45	56	47	45	28	18
Cloud coverage, mean (%)	84.5	86.7	83.6	83.7	85	88.1	79.3
Cloud coverage, std.dev (%)	13.2	12.2	14.1	12.9	13	12.8	14.9
Cloud base, mean (m)	1133	1154	1218	1303	1319	1401	1348
Cloud base, std.dev (m)	398	394	385	403	432	415	551
Sfc.buoyancy flux, mean (Wm^{-2})	121	140	154	141	119	93	75
Sfc.buoyancy flux, std dev (Wm^{-2})	72	62	68	73	64	64	49
Convective velocity mean (ms^{-1})	1.64	1.47	1.65	1.62	1.50	1.46	1.46
BLH mean (m)	924	1224	1330	1287	1545	1363	1247
BLH std dev(m)	310	411	473	555	692	744	785

Table 3–5: Classification of updraft and downdraft half-widths during shallow cumulus and clear-sky events based on the time of day computed from the 4 yr data set.

$LST(hr)$	$10-11$	$11-12$	$12-13$	$13-14$	$14-15$	$15-16$	$16-17$
			Cumulus-topped periods				
Updraft half-width	0.81	0.74	0.57	0.60	0.54	0.51	0.53
Downdraft half-width	0.83	0.69	0.65	0.58	0.53	0.52	0.51
			Clear-sky periods				
Updraft half-width	0.73	0.68	0.66	0.50	0.58	0.57	0.49
Downdraft half-width	0.80	0.79	0.64	0.50	0.58	0.58	0.60

CHAPTER 4
Multi-year, Summertime Observations of Daytime Fair-Weather Cumuli at the ARM Southern Great Plains Facility

4.1 Introduction

Observing FWC are very challenging because of their short length scales ($\sim < 1$km) and life spans (< 30 mins). Previous studies on FWC using aircraft and rawinsonde has its own shortcomings and constraints (e.g., difficulty to a snapshot of vertical profiles inside the cloud from aircraft, lack of high frequency vertical profiles from rawinsonde, etc.) for using them to study vertical structure inside FWC. More over, aircraft observations without onboard radar are dimensionally challenged and operating them routinely are unaffordable. Addressing these problems demands new technologies to sample clouds routinely with high resolution capabilities beyond one dimension. In last 20 years, there has been substantial progress in cloud remote sensing with the development of sophisticated cloud radars, lidars and microwave radiometers (e.g., Lhermitte 1987; Spinhirne 1993; Moran et al. 1998; Liljegren et al. 2001). The strength of cloud radar is its ability to detect cloud and its resolution capabilities, their synergy with lidars, radiometers, sounding and etc., for comprehensive study on clouds. The potential to use cloud radars to study small cumulus has been demonstrated (e.g., Lhermitte 1987; French et al. 1999; Kollias and Albrecht 2000; Kollias et al. 2001). Continuous operation of cloud radars at SGP facility provides an opporutunity to use long–term observations to study FWC. The MMCR

Doppler velocity measurements are treated as representative of the average vertical air motion of the MMCR sampling volume based on the assumption that cloud droplets have negligible fall velocities and thus can be treated as tracers of a vertical air motion (e.g., Kollias and Albrecht 2000). A fuzzy–logic algorithm is developed to remove the insect echoes from MMCR Doppler velocity observations as explained in the methodology (Chapter 2). The processed observations from Millimeter Wavelength Cloud Radar (MMCR) and other active and passive remote sensors at the ARM program Southern Great Plain (SGP) are used to compute the fair weather cumuli macroscopic (horizontal/vertical extend) and dynamical properties of FWC.

Only summertime observations (defined as the 4 month period from May to August - 123 days per season) from the 14-year period from 1997 to 2010 are used in this study. Furthermore, the analysis is limited to the daytime period defined as the 9 hour period from 09:00 - 18:00 LST. Every hourly block of ARM observations is screened for the occurrence of fair-weather cumuli clouds (objectively defined as the cloud tops lower than 4 km) following the methodology used in Chandra et al. 2010, by using both extensive visual inspection of the TSI images and by screening out periods with hourly surface buoyancy fluxes less than 50 Wm^{-2}. Rain gauge measurements and MMCR first detection height and intensity information is used to sample only the non-precipitating clouds. Overcast conditions (stratus or stratocumulus) are filtered out using the TSI and ceilometer.

The inter-annual variability of the occurrence of hourly periods with fair-weather cumuli and in-cloud liquid water path values during the summertime period is shown in Fig. 4-1. The maximum number of hours with FWC that can be observed during the sampled daytime summertime period is 1,098. The fraction of hourly-periods (Fig. 4-1a) with FWC is based on the laser ceilometer measurements and thus is not subject to limitations in instrument sensitivity due to small amounts of liquid or particles size. Noticeable variability (2-4% minimum to 12-17% maximum) is observed from year to year with the maximum occurrence observed almost with a four-year cycle (2002, 2006, and 2010). In addition, the season-averaged LWP (Liquid Water Path) observed by the MWR during FWC conditions is shown (Fig. 4-1b). The value at the box notch in Fig. 4-1b indicate the median value, and the bottom and top edges of the box shows 25th 75th percentile values. The 2-channel microwave radiometer has a detection threshold of 20-25 gm^{-2}. Every hour of FWC observations, only time periods when the ceilometer detects a cloud are used to estimate the hourly LWP value. It is clear from the figure that the summertime shallow FWC contain small amounts of LWC (Liquid Water Content). Though visual inspection of seasonal LWP distributions seems to have a trend, statistical test shows that the trend is insignificant.

4.2 Low radar reflectivities of continental shallow cumuli clouds

The small amounts of LWC combined with typical continental aerosol loading conditions (e.g., Feingold et al. 2003; Vogelmann et al. 2012) results to clouds with small liquid droplet radius. This was confirmed during a recent five-month (February to June, 2011) systematic aircraft-based field experiment (RACORO–Routine AAF (ARM Aerial Facility) Clouds with Low Optical Depths Optical Radiative Observations). The analysis of the aircraft in-site probes revealed that the cloud

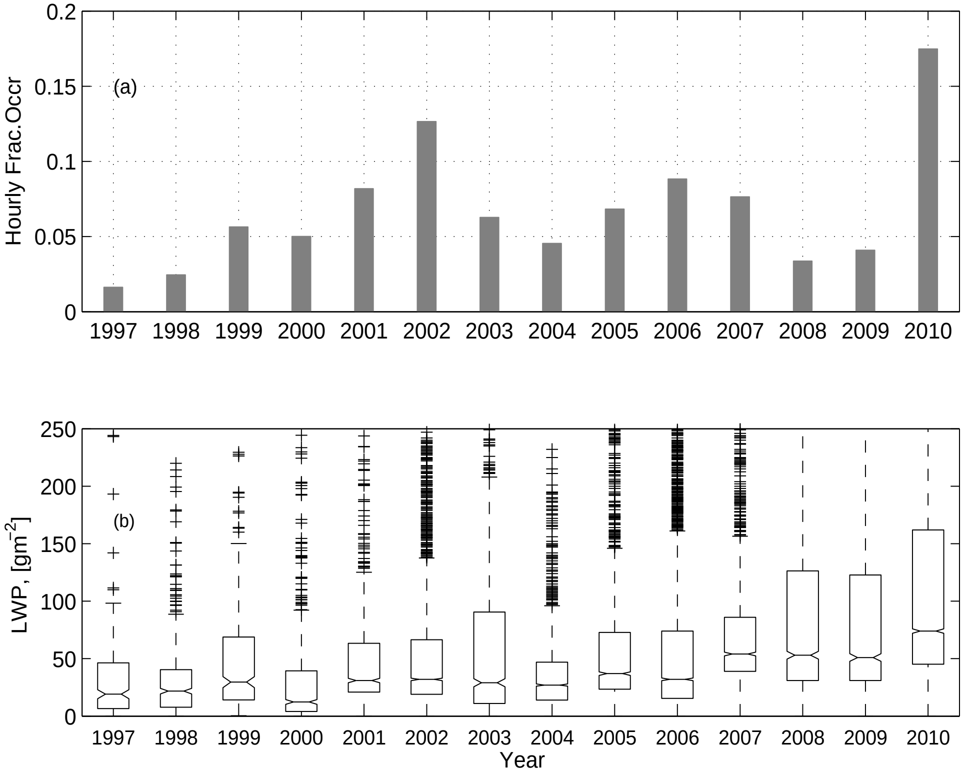

Figure 4–1: Yearly variability of a) Number of fair weather cumuli hours classified based on ceilometer detections during summer time (May-August). b) Summer-time LWP (Liquid Water Path) distributions. The value at the box notch indicate the median value of LWP, and the top and bottom end of the box indicate 25th 75th percentile values.

effective radius between 3-7 μm with preference toward the lower limit (e.g., Vogelmann et al. 2012). Additional verification for the lack of large drops in the shallow cumuli is provided by the statistics of the observed radar reflectivities during FWC conditions. Figure 4-2 shows the frequency distribution of MMCR reflectivity values observed inside FWC clouds as a function of time of day. The plot suggests that the fraction of drizzle particles present in the clouds is negligible and that almost all MMCR observations can be used for the derivation of in-cloud vertical velocity statistics. Furthermore, an interesting daytime evolution of the FWC radar reflectivities is observed, with higher values during morning hours and lower values during late afternoon.

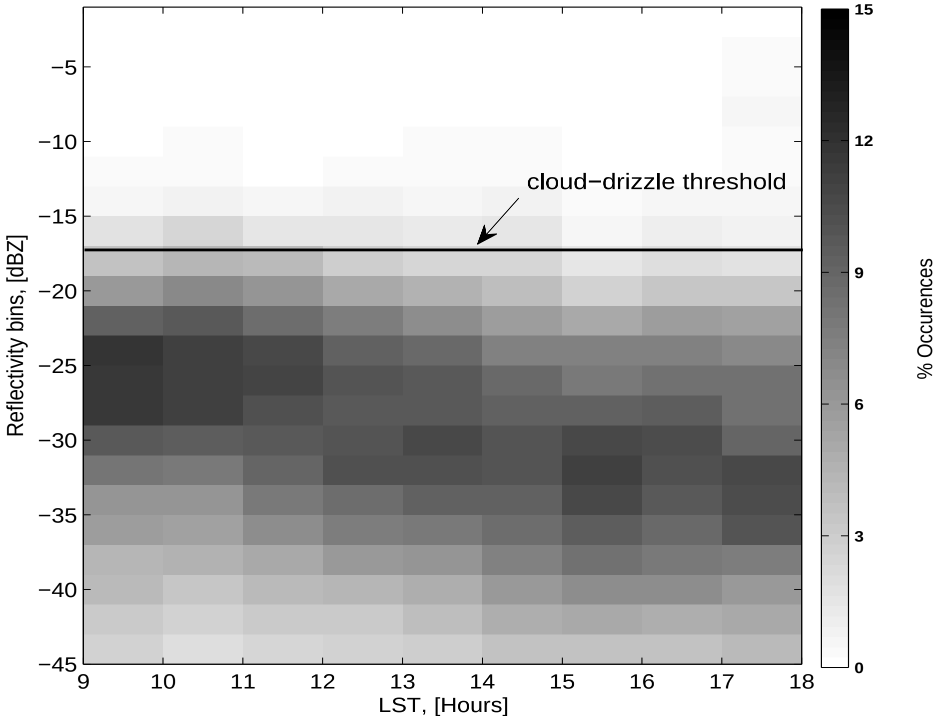

Figure 4–2: Frequency distributions of MMCR Reflectivity values (binsize=2 dBZ) observed inside fair-weather cumuli for different time of the day.

However, the small particle sizes also result in a larger fraction of FWC detected by the ceilometer than by the MMCR. The distribution of ceilometer-only and radar-only detections of FWC as a function of their observed LWP is shown in Fig. 4-3. Assuming that the ceilometer is capable of detecting all overpassing clouds, we can treat the ceilometer-only distribution as the true distribution of shallow cumuli detections as a function of their LWP. As discussed above, the LWP distribution peak at 30-50 gm^{-2}, suggests clouds with very limited vertical development. Despite MMCR's excellent sensitivity (-45 dBZ at 2 km; Moran et al. 1998; Kollias et al. 2007), it misses majority of shallow clouds with LWP<50 gm^{-2} (Fig. 4-3a). Thus, the MMCR based statistics presented here are representative only for a portion (∼ 30-40 %) of the population of FWC developed over the ARM SGP site. Fig. 4-3b shows the hourly comparison of ceilometer-only cloud fraction and radar-only cloud fraction. The ceilometer-only cloud fraction is based on the detection of cloud edge (either cloud base or tilted lateral boundary). The highest cloud fraction (∼ 15 %) is observed early in the day and the cloud fraction gradually decreases below 10 % in late afternoon. The radar-only cloud fraction is the maximum cloud fraction observed by the radar within the cloud layer defined by its ceilometer-defined cloud base and radar-defined cloud top. Earlier studies (e.g., Neggers et al. 2003) reported the significant difference in 1D measurements (like ceilometer or airplane) of cloud size versus 2D (like satellite or LES). Despite these differences, the radar-only cloud fraction is substantially lower (∼ 5 %). The observed differences in the cloud fraction by these two collocated active sensors are consistent with previous studies that have highlighted the challenge in objectively determining cloud fraction (e.g., Wu et al. 2011). Nevertheless, the MMCR misses a significant portion of the FWC clouds at the ARM SGP site.

In addition to the MMCR sensitivity, another challenge that hinders our ability to document FWC clouds at the ARM SGP is insect echoes that overwhelm the

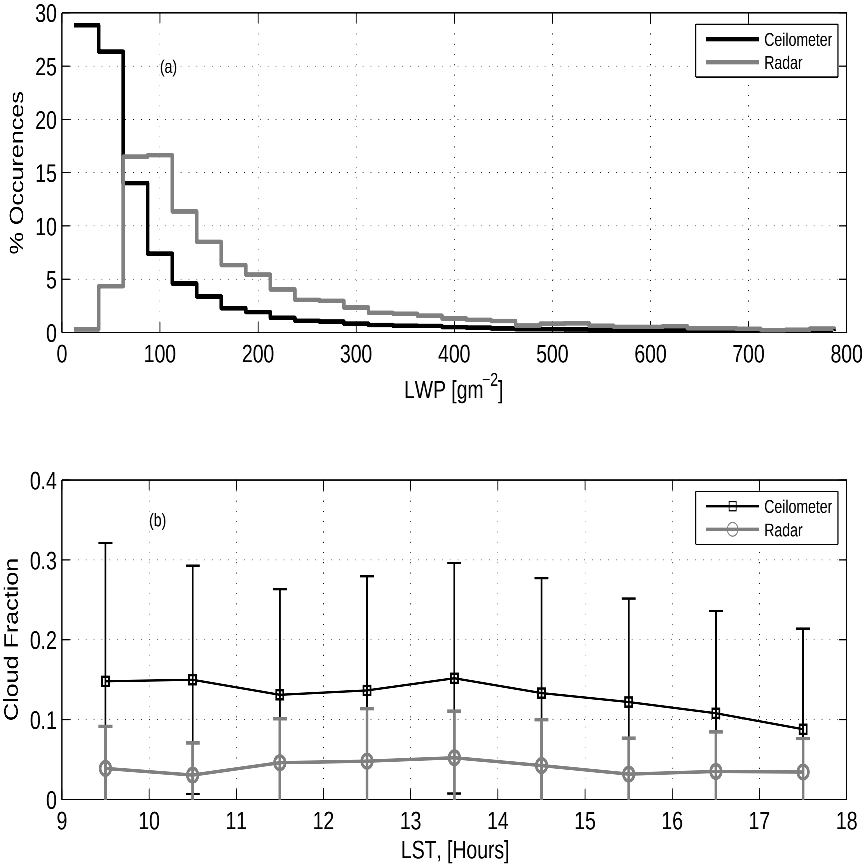

Figure 4–3: (a) Liquid water path distributions inside fair-weather cumuli for the periods when clouds detected from ceilometer and from MMCR. (b) Hourly cloud fractions from the ceilometer detections and the maximum cloud fraction detected from the MMCR.

MMCR returns in the lowest 2-3 km (e.g., Clothiaux et al. 2000; **?**; Luke 2008; Chandra et al. 2010) during the warm season. The ARSCL VAP is the most popular data product in the ARM archive and it is often used as the starting point for deriving cloud macroscopic (e.g., cloud climatology), and cloud microphysical and dynamical properties. As part of the ARSCL standard quality control, insect contamination is addressed by classifying MMCR echoes as either insects' or mixture of cloud and insect returns. No automated algorithm is available, and often manual editing is required. In spite of the extensive quality control efforts, there is considerable misclassification of insect echoes as cloud echoes and the opposite. This is often the case when the ceilometer detects a FWC base and there is little information to enable classification of the radar echoes above the ceilometer-derived cloud base. A new method based on fuzzy-logic (hereafter FL) technique is developed to separate insects from cloud echoes. The details of the algorithm are explained in algorithm section of chapter 2.

4.3 Analysis and discussion

A total of 1040 hours of observations on fair-weather cumuli over the 14-year summer period (1997-2010) are used for the analysis. The hourly statistics calculated from the insect-screened MMCR Doppler moments are classified with respect to their LST from 09:00 to 18:00 and used to provide summary daytime composites. The number of FWC hours available for each LST hourly period, and height distribution of data availability are shown in Fig. 4-4. Panel (4.4a) shows the fractional radar echoes available at each height for every hour considering ceilometer cloud base detections as a reference. Panel (4.4b) shows the fraction of cloud echoes available out of the total radar echoes after applying the fuzzy-logic algorithm. So the missing data fraction is attributed to echoes from insects, drizzle fraction, the portion of the clouds undetected from MMCR due to lack of sensitivity, and reduction in cloud area due to change in cloud chord diameter with reference to the cloud base. The distribution of MMCR FWC echoes screened for insects using the fuzzy-logic technique is skewed towards the base of the cloud layer during 09:00-14:00 LST suggesting very shallow cloud layers (Fig. 4-4a). Such a clustering of the MMCR FWC echoes is not observed during the afternoon hours. This suggests that the source of cloudiness comprises of clouds with different stages of their life cycle. The majority of the cumulus events are observed from 12:00-16:00 LST (Fig. 4-4c) with significantly lower hourly occurrences during the late morning hours (09:00-11:00 LST). This is in agreement with the deepening of the CBL during the day to levels above the LCL (Lifting Condensation Level) of the mixed layer (Fig. 4-4a and 4.4b). A minimum data fraction of 5 % is used to compute in-cloud hourly statistics discussed in the results section. The confidence in the computed statistics is tested using other thresholds (6 and 8 %) for minimum data fraction.

The ceilometer-derived cloud base heights can be used to derive unbiased statistics about the frequency of occurrence of FWC clouds. However, this is not the case with the FWC cloud top height. The use of the ARSCL dataset can lead to significant biases with respect the FWC cloud top height variability (Fig. 4-5b). The ARSCL-derived daytime variability of FWC cloud top height overestimates the FWC layer thickness from 10:00–11:00 LST and underestimates throughout the rest of the day compared to the FL (Fig. 4-5a). Early in the day, the insect layer is deeper than the FWC layer. As the day progresses, the clouds grow deeper with the solar insolation compared to the relatively flat insect layers resulting in an underestimate of the cloud top heights. The cloud thickness vs LWP relation extracted using the ARSCL and the FL dataset cloud top height and the MWR LWP measurements provides additional support for the inferred cloud top biases in ARSCL. Fig. 4-5d shows the relationship between the median of the square of the FWC cloud thickness

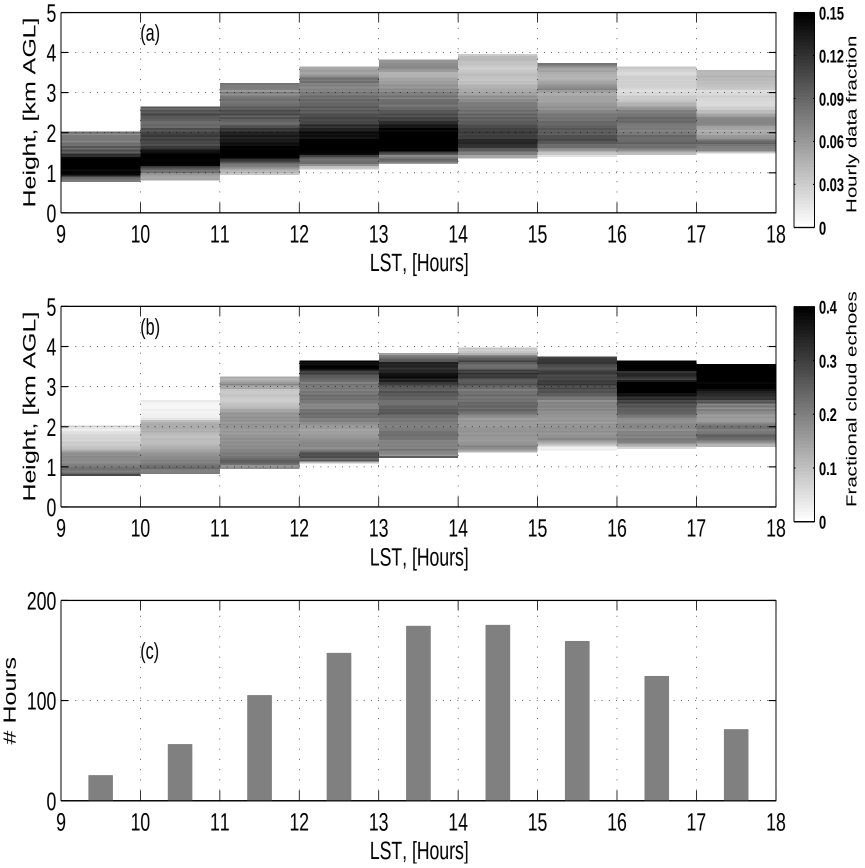

Figure 4–4: (a) Time-height composite of hourly hydrometeor echoes from MMCR available during FWC conditions. (b)Time-height composite of the fraction of the MMCR echoes shown in (a) that are from hydrometeors after applying fuzzy-logic algorithm. (c) Total number of available hours with FWC observations as a function of daytime hours based on the ceilometer detections.

versus their corresponding LWP bins (binsize=50 gm^{-2}). It is clear that the use of the FL dataset results in an improved near-linear relationship that is consistent with clouds that experience only condensational growth and evaporation. The ceilometer reported cloud bases and LCL values show strong diurnal variation with a minimum value occurred during morning, and reaches maximum during late afternoon (14:00–16:00 LST). The daytime variation of LWP values (Fig. 4-5c) shows a maximum value of 120 gm^{-2} between 13:00 and 16:00 LST consistent with the deepening of the cloud layer. The ARSCL-derived data produces unreasonably deep FWC layers for low LWP values (< 50 gm^{-2}) and slightly underestimates for higher LWP values. Thus, the insect contaminations have considerable impact on the ARSCL reported cloud tops, specifically for fair-weather cumuli clouds.

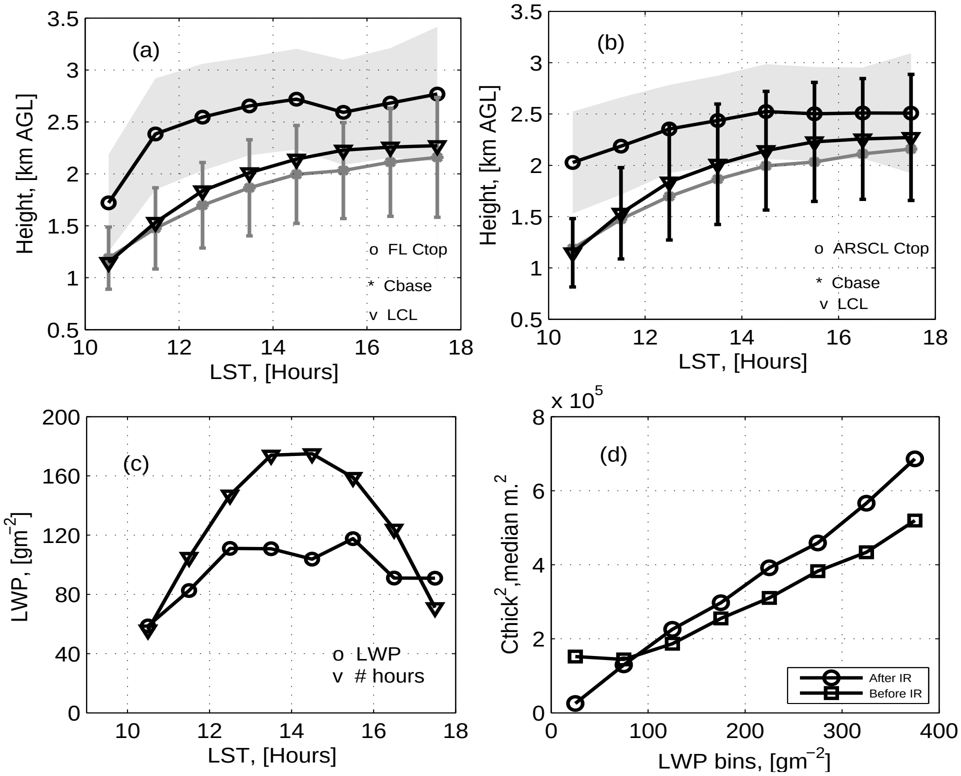

Figure 4–5: Daytime composite variation of a). FL cloud top, cloud base and LCL values. b) ARSCL cloud top, cloud base and LCL values. c) Liquid water path and number of FWC hours available for each hour. d) Plot of LWP (binsize=50 gm^{-2}) v/s Cthick^2 before and after insect removal. Shaded area indicates the standard deviation values. Shaded area in subplot (c) corresponds to the LWP values.

4.3.1 Fair-weather geometrical properties

The cloud geometrical properties such as cloud chord length, cloud spacing, aspect ratio and cloud thickness are very important for radiative transfer calculations in shortwave cloud-radiation parameterization (e.g., Lane et al. 2002; Jiang et al. 2008). The statistics on cloud geometrical properties are calculated on cloud-scale (on individual clouds) using all fair-weather cumuli hours. Here, geometrical properties are estimated for clouds that produced at least 5 consecutive ceilometer detections and have FL-derived cloud thickness of 200 m minimum. Since the ceilometer does not differentiate between actual cloud base and cloud edges, it is necessary to conditionally define the mean cloud base, defined as the lowest 25 % of the ceilometer cloud detections. The average of all the reported cloud top heights within a cloud event is used to derive the cloud mean cloud top. Chord lengths are calculated by transforming the continuous cloud detections from the ceilometer to the horizontal length scale using the winds (from the nearest sounding data) averaged over the cloud depth. The horizontal spacing between clouds is calculated similarly by using the mean winds averaged (winds from the soundings at the closest time) over the cloud depth. The cloud thickness values are calculated from the mean cloud base and cloud top heights. Using all available data, summary distributions of the observed cloud chord length, cloud thickness, aspect ratio and cloud spacing and horizontal wind-speeds averaged over cloud layer depth are estimated (Fig. 4-6). The bin spacing of the cloud chord diameter (L) is 100 m (Fig. 4-6a). 60 % of the observed clouds have a chord length less than 500 m. This is consistent with observed horizontal scales of CBL eddies (e.g., Chandra et al. 2010). The maximum cloud chord length observed in this study is $\sim$ 5 km. The distribution of observed cloud aspect ratio (L/D: ratio of cloud chord length to the cloud thickness) in Fig. 4-6b indicates that 60 % of the clouds have aspect ratio less than 1. These reportings are very intriguing as cumulus clouds generally assumed to have aspect ratios of 1 or above. Detailed inspection of cloud shapes shows that the clouds tend to resemble like towers with lower aspect ratios preferably between morning to late morning hours. Though this explanation offers a plausible reason for the present reportings, it is very difficult to verify because of the assumptions and observational limitations in estimating aspect ratios. It could be possible that the lower aspect ratios may be due to the underestimation of cloud diameters or/and bias in transforming time to length scale due to the lack of high frequency horizontal winds. The MMCR sensitivity can also offer a plausible explanation for the observed low aspect ratio. Due to its limited sensitivity , our sample does not include the numerous shallow clouds with large aspect ratio and it is weighted by the fewer thicker cumulus that are detected by the MMCR and have lower aspect ratio. At this point, we can only offer a plausible reasons. The future scope is to verify the validity of these reportings using models or observations which offers high frequency horizontal observations. The distribution of horizontal winds averaged over cloud depth are shown in Fig. 4-6c. The mean winds are peaks between 7-10 ms^{-1}. The distribution of the FL-derived cloud thickness (D) is shown in Fig. 4-6d. The bin spacing of the cloud thickness (D) is 150 m. The distribution peaks at 300-600 m. Finally, the distribution of horizontal spacing between clouds is shown in Fig. 4-6e. The most frequent occurrence of the cloud spacing values is 250-500 m and drops exponentially.

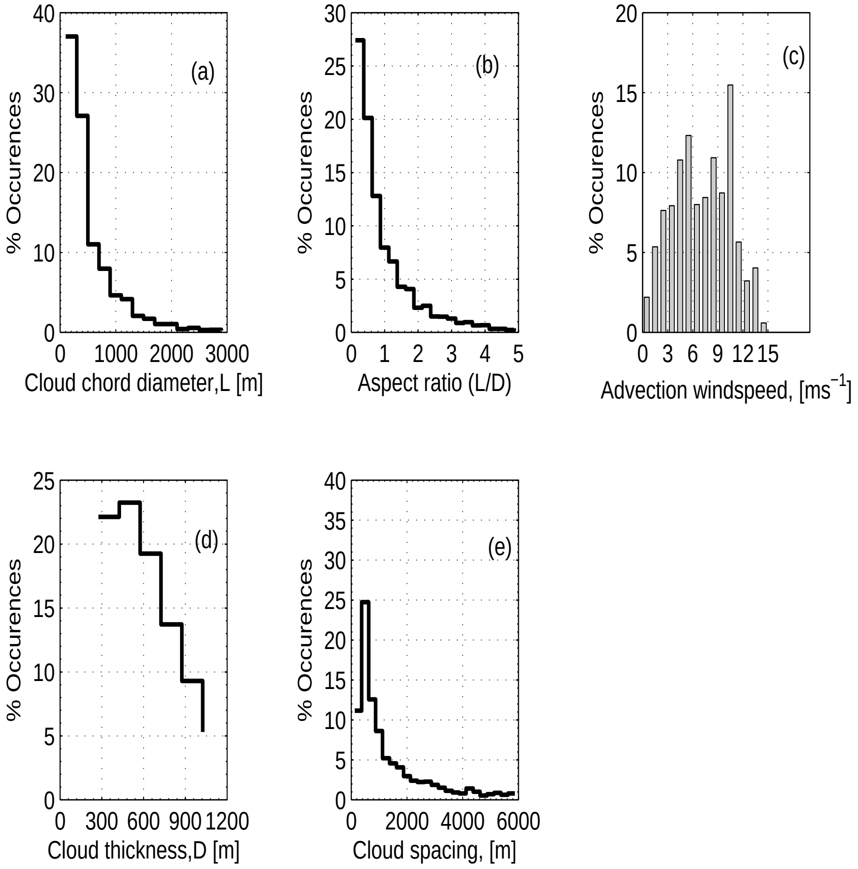

Figure 4–6: Histogram of (a) Cloud chord diameter (binsize of 200 m). (b) Cloud aspect ratio (binsize of 0.25). (c) Wind speed averaged over the cloud depth (binsize of 1 ms^{-1}). (d) Cloud thickness (binsize of 150 m). (e) Cloud spacing (binsize of 250 m).

Figure 4-7 shows a plot of normalized cloud chord diameter density (defined as the probability of occurrence of clouds at the range of the cloud chord sizes) versus cloud chord diameter values. Past studies used aircraft observations and LES model output (e.g., Benner and Curry 1989; Cahalan and Joseph 1989; Neggers et al. 2003; Berg and Kassianov 2008) to develop a functional relationships similar to the ones shown in Fig. 4-7. The large cloud samples (5311 clouds over 14 years) from this study provided an opportunity to examine previous functional relationships. The observed relationship (Fig. 4-7, circles) agrees well with the previously suggested power law fit, and there is a robust feature of clear scale break at $\sim$ 1000 m, which compares well with the derived values of Neggers et al. 2003 [no of clouds= 2828] using LES of cumulus-over-land, and aircraft observations from Jiang et al. 2008 [no of clouds=92]. The exponent of the power law is lower (-1.16 +/- 0.02: mean value indicate daytime average, and the value after +/- indicate the standard deviation) compared with values from the previous studies (-2.3 and -1.9 for aircraft and model study of Jiang et al. 2008; -1.7 for LES study by Neggers et al. 2003; -2.0 for Benner and Curry 1989). This may be due to large sampling of clouds covering different meteorological conditions over 14 years. In general, comparing cloud chord diameters from different platforms (aircraft/ceilometer/satellite) involves bias due to errors in sampling (Neggers et al. 2003).

4.3.2 Turbulence statistics

Using the 1040 FWC hours identified over 14 years, daytime, hourly composites of surface and FWC parameters are composed (Fig. 4-8). The FWC cloud-base updraft mass flux is estimated using the method outlined in Kollias and Albrecht (2010). Significantly higher updraft mass flux (Updraft mass flux=air density*updraft fractional area*updraft velocity) values are observed between 12:00 - 14:00 LST with a magnitude of 0.05-0.06 $kgm^{-2}s^{-1}$ (Fig. 4-8a). Lower values (0.02-0.03 $kgm^{-2}s^{-1}$) are observed during the morning and late afternoon periods. The magnitude and the timing are comparable to the recent FWC study by (Kollias and Albrecht (2010)),

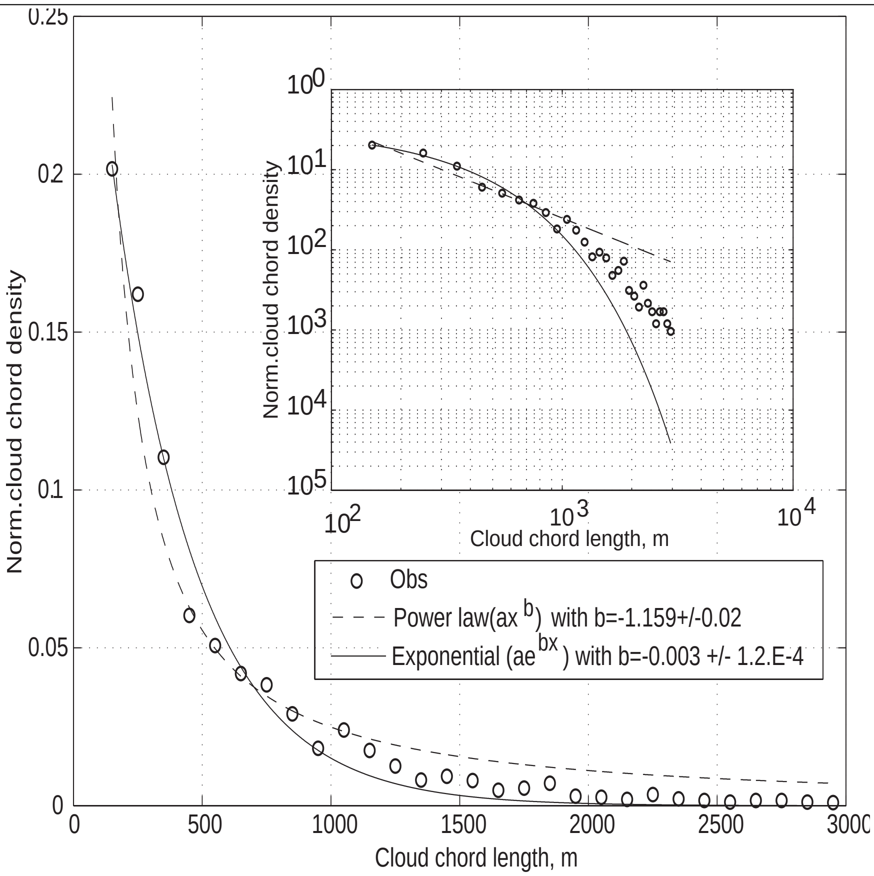

Figure 4–7: Plot of normalized cloud chord diameter density versus cloud chord diameter (binsize=100 m). Circles denote the cloud chords calculated from ceilometer data. A solid and dashed line denotes exponential and power law fit to the data. In the figure legend, the mean value indicates the average of exponents (b) when the cloud chord length is decomposed for different time of the day, and the value after the +/- indicate standard deviation. The logarithmic representation of the distribution is showed on the top-right corner.

who studied island-induced FWC at the ARM Tropical Western Pacific site at Nauru. The updraft mass flux maximum coincides in time with the daytime maximum in the updraft fraction maximum and the surface buoyancy flux maximum (Fig. 4-8b and 4.8d). Subplot 4.8b shows the hourly composite daytime variation of the mean updraft velocity at the cloud base. The maximum cloud base updraft velocity magnitude (0.7-0.8 ms^{-1}) is observed at 13:00-14:00 LST which is in comparable to study by Kollias and Albrecht (2010). Fig. 4-8c shows the daytime variation of the updraft fraction (fraction of updraft portion of the cloud to the total clear and cloudy area in an hour). The maximum in the mean updraft fraction ($\sim$ 6 %) is also observed between 13:00-14:00 LST. Fig. 4-8d shows the daytime variation of the surface sensible, latent and buoyancy flux. The buoyancy flux reaches a maximum of about $\sim$ 300 Wm^{-2} between 13:00-14:00 LST. The latent heat flux exceeds the sensible heat flux with an average Bowen ratio of 0.72.

Figure 4-9 shows hourly cloud base and cloud top vertical velocity statistics over the entire observing period. Every hour, velocities are sampled inside the cloud at the average locations of cloud base and top. The normalized distributions of the hourly-averaged mean vertical air motions at the cloud base and cloud top height are centered on zero (Fig 4-9a). The vertical air motion standard deviation values range between 0.4 to 1.3 ms^{-1} at the cloud base and the cloud top with maximum occurrences between 0.6-0.9 ms^{-1} (Fig. 4-9b). To avoid sampling errors for computing statistics, a minimum cloud fraction 5 % is specified. Assuming there is no bias due to sampling, the normalized distribution of the hourly vertical air motion skewness at the cloud base and tops (Fig. 4-9c) indicates both positive to negative values, with the peak of the distribution at the cloud base and top locations are approximately centered at zero with the variability covering both positive and negative values.

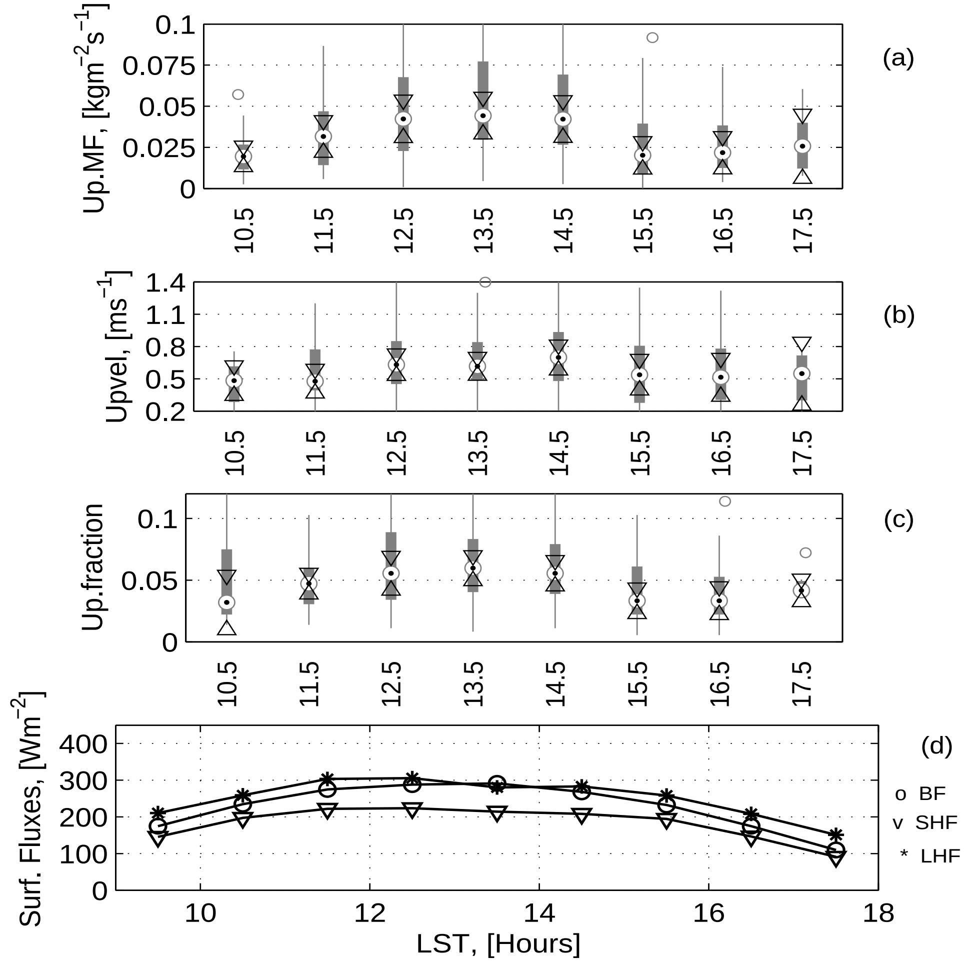

Figure 4–8: Hourly daytime composites during fair-weather cumuli condition for the period 1997-2010. a) Cloud base updraft mass flux. b) Cloud base bulk upward velocity. c) Cloud base updraft fraction. d) Surface sensible (SHF), latent (LHF) and buoyancy fluxes (BF). Circles in subplots (a-c) indicate median values and the corresponding grey vertical bar shows 25th and 75th percentile values.

The entire dataset composites of hourly-averaged profiles of updraft and downdraft mean properties are shown in Fig. 4-10. Each composite profile is a result of averaging the hourly profiles over cloud depth where there are significant hourly profiles (at least 20 profiles) available for computing the statistics. Top and bottom

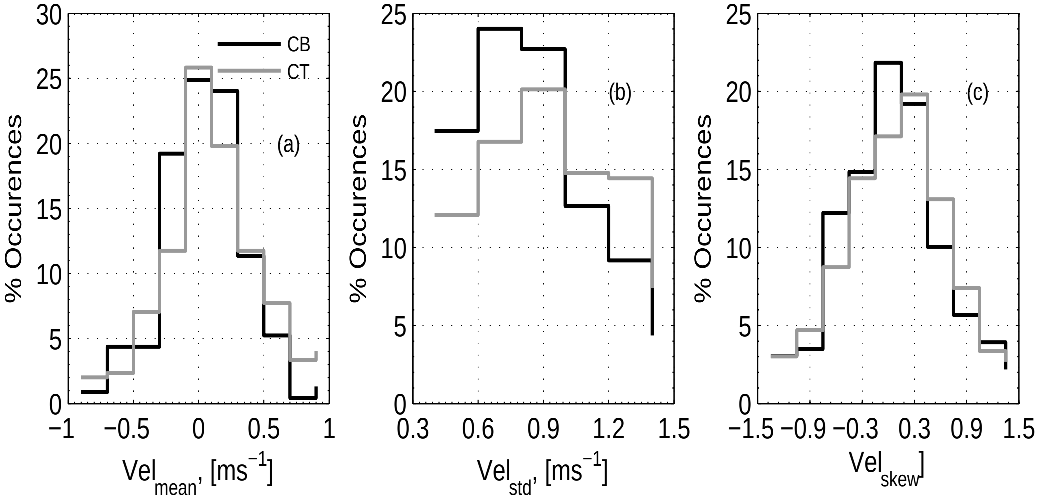

Figure 4–9: Histograms of hourly mean cloud base (CB) and cloud top (CT) statistics from all the FWC hours. (a) Mean vertical velocity (binsize of 0.2 ms^{-1}). (b) Vertical velocity standard deviation (bin size of 0.2 ms^{-1}). (c) Vertical velocity skewness (binsize of 0.3).

locations in each profile indicate the average locations of cloud base and cloud top heights in that hour. At each hour, there is a significant variability of cloud base and tops (as shown in Fig. 4-5) indicating clouds are sampled from different height locations. The updraft fraction is computed as the fraction of the hour with observed in-cloud updraft. All the profiles shown in Fig. 4-10 are mean averaged profiles. The range of variability (25th and 75th percentile values) associated with mean profiles are shown in Fig. 4-11 for the period 13-14 LST. In spite of wide scatter in the mean profiles, the in-cloud profiles show a weak daytime variability. The maximum in updraft and downdraft fraction profiles are observed just above the cloud base height (Fig. 4-10a,d), and their magnitude varies considerably during the daytime with the maximum (0.045) observed during 12:00-14:00 LST and coincides with the maximum cloud fraction (Fig. 4-4). The shifting of the maximum in profiles of updraft and downdraft fractions (Fig 4-10a,d) is due to evolution of average cloud base and top locations (Fig. 4-5). Overall, the profiles of updraft and downdraft fractions are similar in shape and comparable in magnitude. The corresponding profiles of updraft-downdraft air motion magnitudes are shown in Fig. 4-10b,e. The weakest magnitudes for both updrafts and downdrafts are observed near the cloud base (0.6 - 0.8 ms^{-1}) with the exception for the period 11:00 - 12:00 LST. The bulk updraft and downdraft velocities shows increasing trend in the cloud layer from cloud base until near to the cloud top, and thereof shows decreasing trend upto the cloud top, this may be due to cloud top entrainment. The profile of updraft and downdraft massflux profiles (Fig. 4-10c,f) shows no clear trend. It is not straight forward to compare the results from previous LES studies (case studies) with the present results (composites) as there are some significant differences between them. For e.g.: In previous model studies (e.g., Lenderink et al. 2004; Brown et al. 2002; Seibesma et al. 2003), the modeled cloud elements do have roughly the same cloud base height at particular hour, where as, in the present study, there is significant variability of cloud bases at each hour (as shown in Fig. 4-5). These differences influence the mass flux profiles from sampling the clouds at different heights. The Bowen ratio for the case study considered over ARM SGP for previous LES and SCM simulations of shallow cumuli (e.g., Brown et al. 2002; Lenderink et al. 2004) was very low (~ 0.2) compared to an average value (0.72) reported from this study. Lower Bowen ratios influence the subcloud layer through moistening, which in turn influence the cloud vertical development as reported from the recent study by Zhang and Klein (2010). So, the

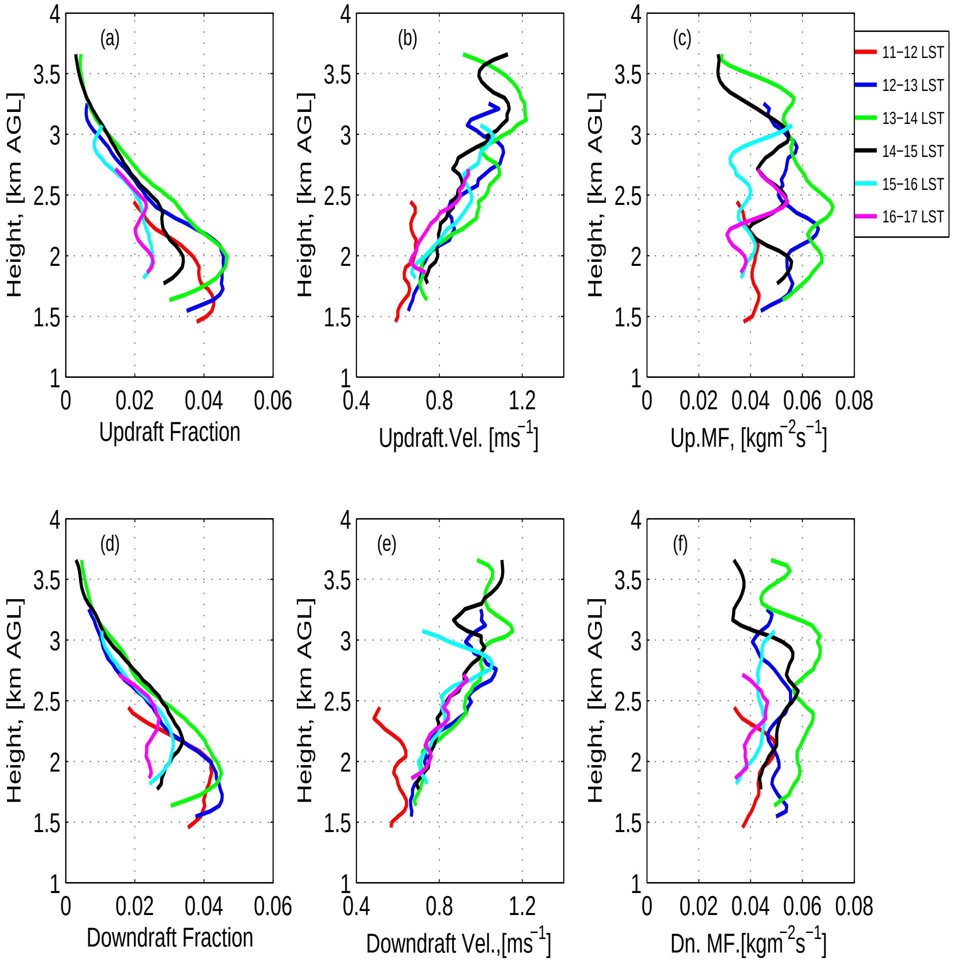

Figure 4–10: Composite hourly profiles of vertical velocity statistics for different time of the day. a) Updraft fraction. b) Bulk updraft velocity. c) Updraft mass flux. and d) Downdraft fraction. (e) Bulk downdraft velocity. (f) Downdraft mass flux. Profiles at each hour are computed independently from all the fair-weather cumuli hourly events at this hour from 14 years of dataset. The values shown on the figure are mean values. The 25th and 75th percentile values for the period 13-14 LST are shown in Fig. 16.

case study considered for previous LES simulations of shallow cumuli over ARM SGP may not be representative for summer-time shallow cumuli over SGP. However, qualitative comparisons of present results with previous modeling results shows both similarities and differences. The shape of updraft velocities inside the cloud layer is in consistent with previous LES simulations (e.g., Seibesma and Cuijpers 1995; Heus et al. 2008) over the ocean. The maximum in updraft fraction profile occurred right at the cloud base in previous model studies compared to the occurrence of maximum slightly above the cloud base values. This may be due to the presence of more forced clouds at the lower levels, which have contributed significantly to the updraft fraction at the lower levels.

Figure 4-11 shows the range of variability for the variables plotted in Fig. 4-10 for the period 13-14 LST. Overall, the variability captures the mean values plotted in Fig. 4-10 with decreasing trend in updraft and downdraft fraction, and increasing trend in updraft and downdraft bulk velocities inside the cloud layer. An increase in updraft fraction (Fig. 4-11a) at the lower levels ($\sim$ 1.75 km) justifies the consistency of the mean profile shown in Fig. 4-10a.

The composite profiles of hourly-averaged in-cloud vertical velocity statistics as a function of normalized cloud height are shown in Fig. 17. The daytime variability for all the variables plotted in Fig. 4-12 are tabulated in Table. 4.1. A gradual daytime evolution of the updraft fraction profiles (Fig. 4-12a) is observed with the strongest updraft fraction values observed during 12:00-14:00 LST period. During this period, the maximum updraft fraction is observed in the middle of the FWC cloud layer (0.13). The profiles of bulk updraft velocity (Fig. 4-12b) shows an increasing trend inside the cloud layer. The shape of mass flux profiles (Fig. 4-12c) are similar to updraft fraction profiles with a gradual daytime evolution and strongest magnitudes (0.12 $kgm^{-2}s^{-1}$)) are observed between 12:00-14:00. The shape and occurrence of

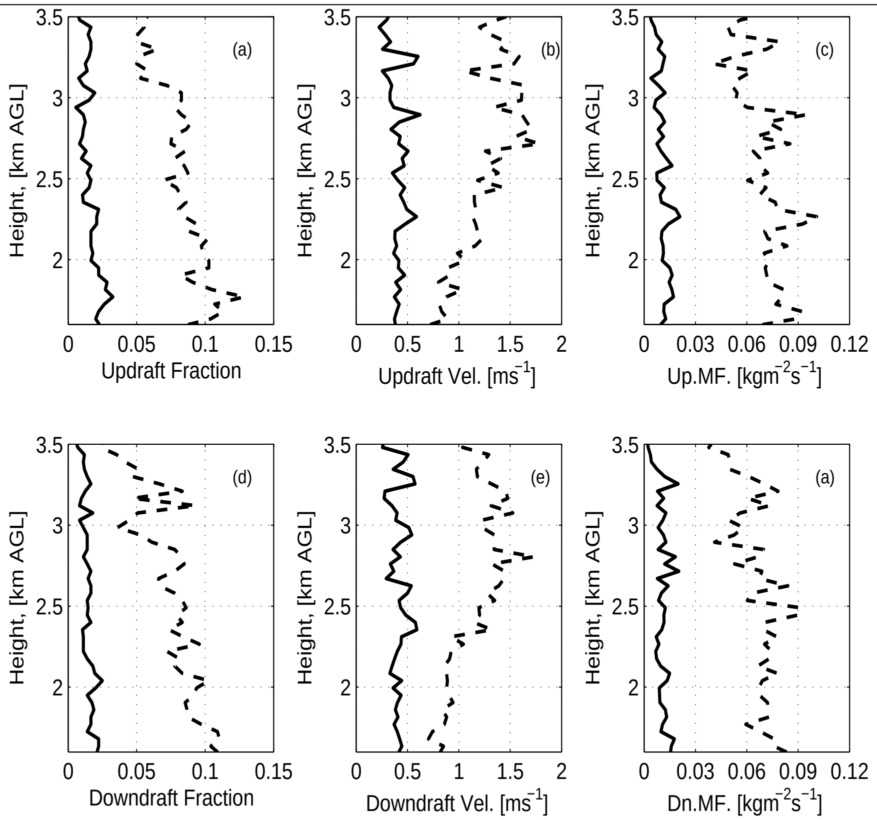

Figure 4–11: 25th (Black line) and 75th (Dotted line) percentile values for the variables plotted in Fig. 4-10. during 13-14 LST.

maximum in the profiles of updraft mass flux are similar updraft fraction. This is consistent with the previous reporting of Ghate et al. 2011. The range of mass flux values are comparable to the recent FWC study by Kollias and Albrecht 2010 and previous LES studies (e.g., Neggers et al. 2004; Rooy and Seibesma 2008; Neggers et al. 2004). The net mass flux profiles (Fig. 4-12d) through out the daytime are positive except during late afternoon periods. Suggesting that the net mass flux is flux is different from the one simulated for BOMEX Seibesma and Cuijpers 1995. The shape and magnitude of downdraft fraction and downdraft mass flux profiles

Table 4–1: Tabulated 25th and 75th percentile values for the variables plotted in figure 17.

$Norm.Cld.Ht$	$Up.MF$	$Dn.MF$	$Net.MF$	$Vel.Mean$
0	0.015/0.053	0.02/0.06	-0.03/0.01	-0.22/0.15
0.2	0.037/0.108	0.03/0.09	-0.02/0.05	-0.133/0.242
0.4	0.041/0.13	0.03/0.12	-0.03/0.06	-0.169/0.3
0.6	0.043/0.136	0.03/0.12	-0.03/0.06	-0.15/0.3
0.8	0.038/0.120	0.03/0.10	-0.04/0.05	-0.175/0.28
1.0	0.031/0.1	0.026/0.1	-0.03/0.04	-0.19/0.30

$Norm.Cld.Ht$	$Upvel.Mean$	$Upfrac$	$Dnvel.Mean$	$Dnfrac$
0	0.41/0.80	0.03/0.07	0.45/0.9	0.03/0.08
0.2	0.47/0.97	0.05/0.133	0.46/0.84	0.04/0.13
0.4	0.44/1.02	0.058/0.162	0.47/0.89	0.04/0.15
0.6	0.44/1.04	0.06/0.147	0.45/0.9	0.05/0.16
0.8	0.42/0.99	0.052/0.147	0.46/0.94	0.047/0.15
1.0	0.44/1.04	0.04/0.11	0.43/0.98	0.04/0.12

(Fig. 4-12e,g) are comparable to the updraft fraction and updraft mass flux profiles respectively. This is suggesting the role of downdrafts in the net mass flux budget as previous model studies over the ocean (BOMEX;(Seibesma and Cuijpers 1995)) suggested that the magnitudes of downdraft mass flux is negligible in the mass flux budget. The bulk downdraft velocities (Fig. 4-12f) inside the cloud layer are nearly constant with height. The profiles of bulk mean vertical velocities (Fig. 4-12h) are upward throughout the cloud layer. Saying that, there is a net upward transport inside the cloud layer.

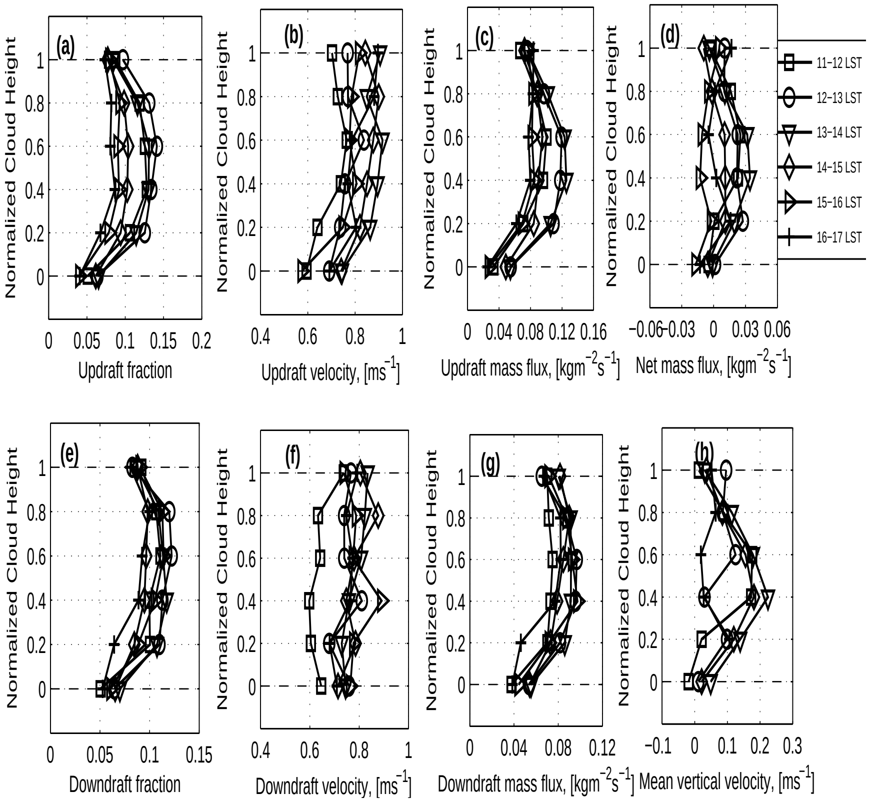

Figure 4–12: Daytime evolution of normalized composite profiles of (a) Updraft fraction. (b) Bulk updraft velocity. (c) Updraft mass flux. (d) Net mass flux. (e) Downdraft fraction. (f) Bulk downdraft velocity. (g) Downdraft mass flux. (h) Mean vertical velocity. For each hour, normalized profiles are computed between average cloud base and cloud top, and composite profiles are obtained by averaging all the normalized profiles at this hour. The quantities plotted above are mean values, its daytime variability in terms of 25th and 75th percentile values are tabulated in table 4.1.

4.4 Summary

The multi-year observations at the ARM SGP site offers unique opportunities to develop robust statistics of summertime shallow cumulus clouds macroscopic and dynamical properties. Although a breadth of measurements from surface, active and passive sensors is used in this study, the MMCR observations are the main source of information above the laser-detected cloud base height. Two factors complicate the utilization of the MMCR observations to characterize the FWC properties. First, due to radar sensitivity limitations, the MMCR-observed FWC clouds are only representative of a subset of the total FWC population formed at the SGP site. Second, the presence of insects above the ceilometer-derived cloud base height contaminates the MMCR observations of FWC with a considerable amount of insect echoes. To address this, a new fuzzy-logic based algorithm is developed to eliminate the insect echoes in the boundary layer. The technique is evaluated using dual-wavelength observations at the ARM SGP site and it is applied to the multi-year (14 summer months) MMCR data set. The refined ARSCL dataset is then used to document the daytime evolution of fair-weather cumulus clouds such as in-cloud vertical velocity statistics (such as profiles of updraft and downdraft fractions, bulk updraft and downdraft velocities, and updraft and downdraft mass fluxes), surface parameters and cloud geometrical properties.

There is a noticeable variability in the inter-annual occurrence of summer-time FWC (2-4 % minimum to 12-17 % maximum) with maximum occurrence observed every four years. The results confirms that the summer time shallow FWC contain small amounts of liquid water content with liquid water path peaks at 30-60 gm^{-2} and the cloud radar sensitivity misses significant fraction of thin clouds with LWP< 50 gm^{-2}. These findings serve as a guidelines for using MMCR systems to study shallow cumulus clouds.

The insect contamination has considerable impact on the ARSCL reported cloud tops, LWP-cloud thickness relationship, and also on the vertical velocity statistics (e.g., vertical profile of cloud fraction and mass flux profiles). The cloud thickness is overestimated by more than a factor of two for lower LWP values and slightly underestimates for higher LWP values. The adjusted LWP-cloud thickness relation using FL derived cloud tops follows near linear relationship, which is consistent with the clouds that experience condensational growth in the absence of precipitation. On daily basis, the bias in the cloud fraction profiles varies from 0-60 % and for the mass flux profiles, it varies between 0-30 % for various insect fractions.

The cloud geometrical properties such as cloud chord length, cloud spacing, aspect ratio and cloud thickness are calculated using large cloud sample ($\sim$ 5300 clouds) over 14 years. It is observed that the typical occurrence of cloud thickness values are 300-600 m and cloud chord length is $\sim$ 200 m. The maximum occurrence of aspect ratios based on cloud chord diameters is at 0.5, indicating the dominance of tower like clouds with vertical extent higher than their horizontal dimensions. The distribution of normalized cloud chord diameter density follows power law with a clear scale break at $\sim$ 1000 m, which compares well with the previous studies.

This study is the first of its kind to provide composite daytime evolution of FWC turbulence parameters. The maximum in the mean cloud base mass flux is occurred between noon and 2 pm with a magnitude of 0.05 $kgm^{-2}s^{-1}$ and drops to minimum towards morning and evening periods. The timing of maximum in the cloud base mass flux coincides with the maximum in the updraft fraction and the surface buoyancy flux indicating the association of clouds to the surface forcing. The magnitude and timing of cloud base mass flux values in this study are comparable to the previous studies. The mean updraft velocity at the cloud base is 0.8 ms^{-1} and maximum occurs between 1 and 2 pm, which is comparable to that reported in previous studies (e.g., Kollias and Albrecht 2010; Heus et al. 2008). The maximum in the mean updraft fraction at the cloud base is occurring between 1 and 2 pm with a mean value of $\sim$ 6 %. The LCL values and the cloud boundaries (cloud base and tops) have a strong daytime variation with the lowest values observed during morning, and cloud boundaries and LCL reaches maximum between 2 and 3 pm and 3 and 4 pm respectively. The timing of the LWP (convective activity) shows a maximum value of 120 gm^{-2} between 1 and 4 pm. The cloud fraction has a weak diurnal variation with a mean value of 0.12.

The hourly mean vertical velocities both at the cloud base and cloud tops are close to zero, suggesting that the fractional area of updrafts inside the clouds compensates the downdraft area, which is in agreement with previous observations in shallow, non-precipitating cumulus clouds. It is interesting to observe the hourly vertical velocity skewness at the cloud base and tops to have lot of variability around zero, because some cloud parameterization schemes (e.g.,Bretherton et al. 2004) assume a gaussian (Skewness=0) vertical velocity distributions at the cloud base. The hourly profiles of vertical velocity statistics such as updraft and downdraft fraction, and mean updraft and downdraft velocity inside the cloud have a weak diurnal variability with a maximum occurring between 12-14 LST at $\sim$ 1.8 km. The composite profiles of updraft fraction as a function of normalized cloud layer depth showing maximum at the middle of the cloud layer, which is consistent with the previous reporting from (Kollias and Albrecht 2010);but the updraft velocity profiles show an increase with height through the entire cloud layer except near cloud top. The normalized profiles of updraft mass flux inside the cloud shows a maximum at the middle of the cloud layers that occurs between 12-14 LST. The magnitude of downdraft mass-flux values are in comparable to the updraft massflux profiles, suggesting the role of in-cloud downdrafts in massflux budget in shallow cumuli.

The properties of fair-weather cumuli observed over the ARM SGP provide a crucial data set for assessing the distribution of scalar fluxes (e.g., heat, moisture, etc) inside the cloud. The analysis provided can serve as an observational target for evaluating LES and mass flux schemes for shallow clouds at a continental site. The day-time evolution of the cloud and boundary layer properties provide a particularly robust behaviour for challenging models and parameterizations.

CHAPTER 5
Evaluating the updraft characteristics in mass-flux schemes using Doppler Lidar observations

5.1 Introduction

In cloudy boundary layers, the mass-flux at the cloud base is often parameterized in terms of subcloud layer turbulence driven by the surface forcing and atmospheric stability. Mass-flux based parameterization are very appealing since the turbulent transport requires only knowledge of the updraft magnitude and fractional area. However, the available mass-flux schemes are based on limited data sets and often tested only over the ocean. Our work (Chapter 4) has shown already that there is very little correlation between the cloud fraction and surface forcing. While there is little surprise in this finding, here we are interested in testing some of the fundamental assumptions in the proposed mass-flux schemes (e.g., Bretherton et al. 2004; Grant 2001). In particular, we will test some of the assumptions made with respect to the statistical properties for the vertical air motion and its relationship to cloud fraction. Some of these assumptions are: i) the vertical air motion PDF in the subcloud layer and in particular near the cloud base is described by a Gaussian distribution; ii) the fractional coverage of updrafts at the LCL equals the cloud fractional coverage and iii) clouds do not contribute to the subcloud layer turbulent kinetic energy budget. In most cases, models (e.g., LES, CRMs, etc.) are used to test the rationale behind these schemes but model validation is challenging due to the lack of comprehensive observational data sets especially related to the vertical velocity field.

During April-May 2011, a joint field campaign MC3E involving NASA and ARM investigators was conducted in south-central Oklahoma to address various components (such as- convective initiation, updraft/downdraft dynamics, condensate transport and detrainment, precipitation, and cloud microphysics, etc.) of convective parameterizations (Midlatitude Continental Convective Cloud Experiment (MC3E) ;http://campaign.arm.gov/mc3e/). Some of the recent observations available from MC3E field campaign include Doppler lidar measurements, high frequency soundings (8 per day), and dual frequency scanning cloud radar measurements along with the supplemental surface observations.

5.2 Doppler Lidar Observations

The Doppler Lidar (www.arm.gov/instruments/dl) is an active remote sensing instrument that provides time-height resolved Doppler velocity and attenuated backscatter. Doppler lidars operate in the near-infrared region (1.5 μ m) and are thus sensitive to micron-sized aerosol particles. Since aerosol concentration decreases with height, the range of the Doppler lidar observations is limited to the CBL. Doppler lidars are capable of measuring the radial Doppler velocity during clear-sky and non-precipitating convective conditions within the boundary layer with very good velocity precision ($\sim$ 0.1 ms^{-1}). In vertical pointing-mode, Doppler lidars provide time-height measurements of vertical air velocity. The height coverage of vertical velocity in the boundary layer depends on the aerosol concentration profile. During convective conditions, there are more organized coherent structures in the CBL associated with scalar (e.g., pollutants, aerosols, heat, moisture, etc) transport. This results in the possibility to trace the vertical velocity up to the top of the mixed layer. An example of a time-height plot of lidar measurements has been shown in Figure 5-1.

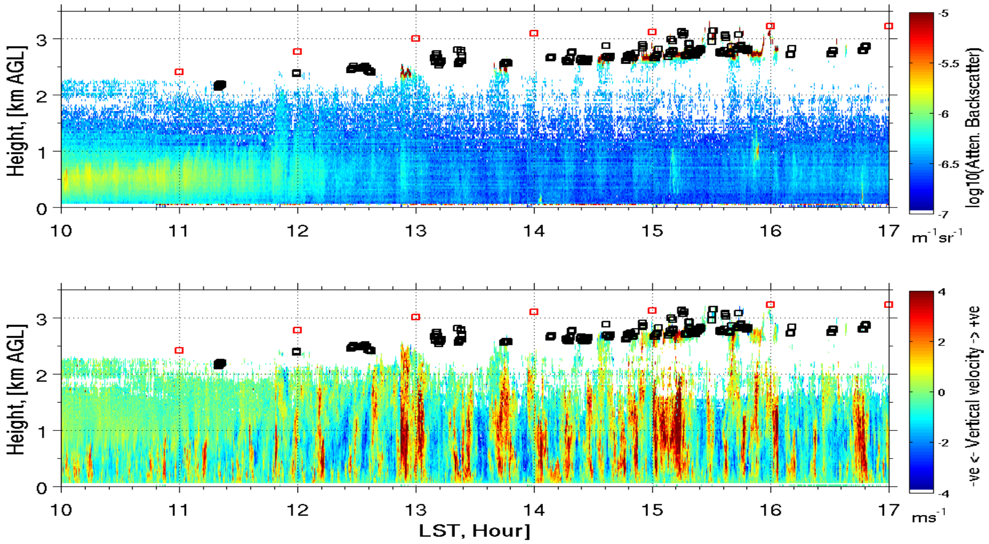

Figure 5–1: Time-height plots of attenuated backscatter ($m^{-1}sr^{-1}$; top panel) and radial velocity (ms^{-1} ; bottom) from vertical pointing Doppler Lidar at the ARM SGP central site. Black (red) squares in the panels indicate cloud base detections from the ceilometer, and hourly LCL values estimated based on surface conditions from the method explained in Bolton (1980), respectively.

5.2.1 Quality control and Data Processing

Doppler lidar measurements should be fairly representative of the magnitude of the radial (or vertical if operate in profiling mode) component of the air motion. The quality of the Doppler velocity measurements strongly depend on the signal-to-noise ratio (SNR in dB). Thus, a SNR threshold is needed to filter out noisy Doppler velocity measurements. The SNR level is generally estimated from the coherency (lag autocorrelation) in the time series of the radial velocity (Frehlich 2001). Based on the level of coherency, one can estimate the precision of velocity measurements as a function of SNR. A sample plot of vertical velocity precision versus hourly SNR values from the measurements taken at the middle of the CBL is shown in Figure 5-2.

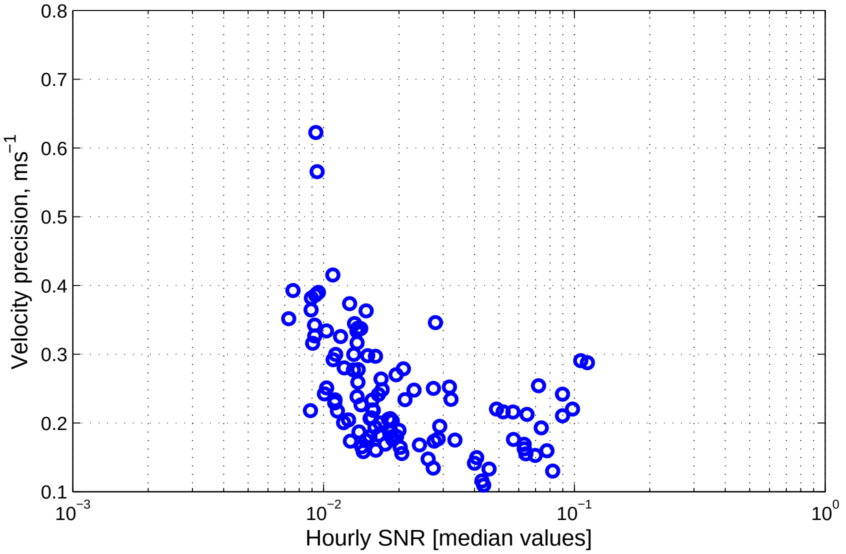

Figure 5–2: Estimates of vertical velocity precision as a function of hourly SNR median values. The data is collected at the SGP central facility during the MC3E campaign and the lidar time series sampled at 0.6 normalized cloud base height from the surface are used for the calculation.

5.2.2 Processing of vertical velocity data

Since the turbulent fluctuations are used for calculating turbulence statistics, the mean has to be removed at each height and for every hour. Outliers in the vertical velocity observations are identified for SNR below 0.01 and velocity precision larger than 0.2 ms^{-1}. Profiles of turbulent statistics (such as variance, skewness, updraft properties, etc) are computed every hour at each height. The vertical coordinate (height) is normalized with the hourly-averaged cloud-base height to express turbulent statistics as a function of normalized distance from surface to the cloud base. The Doppler lidar observations closest to the cloud base height are used to describe the cloud base vertical air motion.

The vertical velocity statistics in vertical columns occupied by clouds and in vertical columns of clear skies are computed separately by decomposing the hourly Doppler lidar observations into cloudy and clear segments. The vertical velocities in cloudy regions are obtained from the lidar corresponding to the continous cloud segments detected from the ceilometer. Similarly, the clear-air region is selected from the periods with no clouds detected by the ceilometer. Once the regions of cloudy and clear-air are separated, the differences in the shape of velocity PDF's are analyzed. The description of method can be followed easily.

5.3 Analysis and discussion

5.3.1 Meteorological conditions

The MC3E field campaign lasted almost two months (April 20 - June 06, 2011),but the new instrumentation and in particular the Doppler lidar continue to operate at the ARM site. Thus, our analysis includes observations for a five month summer period (May - September, 2011). The time series of FWC and surface conditons are shown in Figure 5-3. There is a total of 147 FWC hours available over four months with varying cloud conditions. Precipitation periods are removed using the rain gauge measurements and the MMCR first detection height and intensity to sample only the non-precipitating clouds following the methodology used in Chandra et al. (2010). Overcast conditions (stratus or stratocumulus) are filtered out using the TSI and ceilometer. All the FWC hours considered here are non-precipitating clouds with cloud tops less than 4 km. Panels, (a,c) shows hourly sensible and latent heat flux values. In July, there is maximum net solar radiation reaching the surface, which results in higher sensible heat flux. The hourly FWC cloud fraction varies between 0.1 to 0.6 with the highest values observed during the end of May, which is shown in panel (b). The hourly lowest cloud bases (lowest cloud base values detected from the ceilometer in an hour) calculated from the ceilometer, and hourly LCL values calculated based on surface conditions using the method described in Bolton (1980)) are shown in panel (d). The hourly convective velocities (defined in Chapter 3) are shown in panel (e). Higher sensible fluxes and cloud bases resulted in larger convective velocity values in the month of July. Contrarily, lower cloud bases and sensible heat fluxes during second half of May resulted in smaller convective velocity values. The daily rainfall amount for the five months is shown in panel (f). The numbers inside the box in panel (f) indicates the total number of FWC hours available for different summer months. The number of FWC hours available during June is less compared to May and July, because of more occurrence of deep convective systems (peak tornado season at SGP) compared to the non precipitating cumuli clouds.

5.3.2 Convective velocity approach

According to the relation proposed by Grant (2001), the mass-flux (M/ρ) is linearly related to the convective velocity scale. The linear relationship is tested

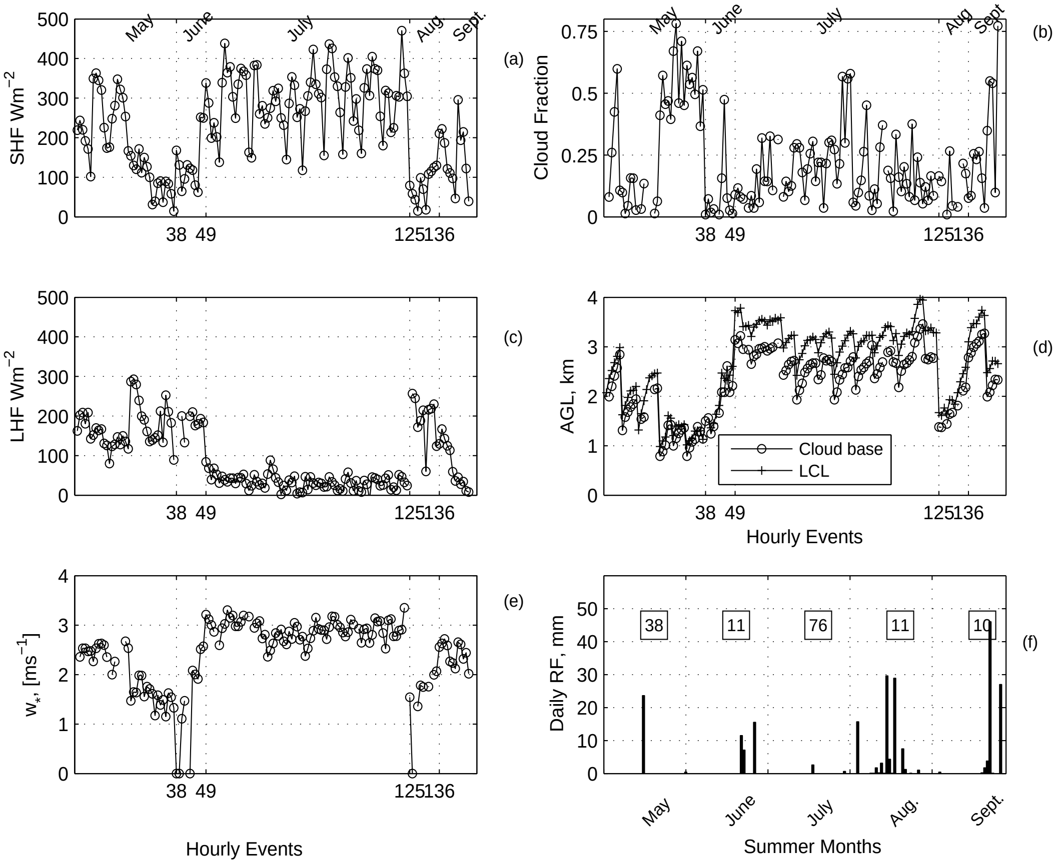

Figure 5–3: Timeseries of (a) Hourly sensible heat flux. (b) Hourly cloud Fraction. (c) Hourly latent heat flux. (d) Hourly cloud bases and lifting condensation level. (e) Hourly convective velocity. (f) Daily rainfall rate during summer month

using LES results for oceanic conditions, and has been discussed in Chapter 1. Here, the validity of the relationship between cloud base mass-flux and convective velocity scale is tested using MC3E data. Figure 5-4 shows the plot of hourly mass-flux (M/ρ) near cloud base as a function of convective velocity (w_*). No clear relationship between mass-flux and convective velocity is evident from the Figure 5-4. This variability can be attributed to different reasons: (1) In this approach, the updraft mass flux is estimated in bulk sense based on surface conditions, without specifically accounting for the transport due to thermals. (2) The stability values observed over the ocean ranges from near-neutral to slightly unstable conditions, where as the range of stability values observed at SGP during MC3E period are very large (not shown here).

If we consider only cloudy columns and we estimate the mean updraft velocity within cloudy periods, we can see a better relationship with convective velocity (Fig. 5.4b). It suggests that conditionally sampling of the updraft motions in cloudy regions could improve the existing relation in parameterizing bulk updraft velocity. Nevertheless, as it was expected, the Grant 2001 mass-flux scheme shows very little skill in predicting the cloud-base mass flux.

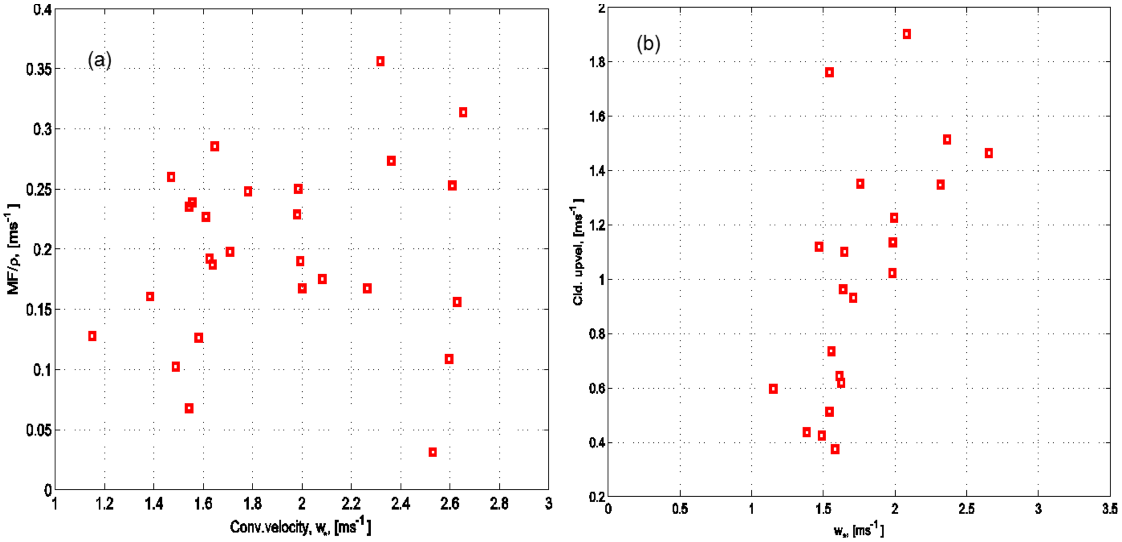

Figure 5–4: Plot of (a) hourly updraft mass-flux (M/ρ) versus convective velocity (w_*). (b) Bulk updraft velocities sampled in cloudy regions as a function of convective velocity (w_*).

5.3.3 CIN based approach

In this approach (Bretherton et al. 2004), the cloud base updraft parameters (such as updraft velocity, updraft fraction, and updraft mass-flux) are expressed in terms of vertical velocity variance near mixed layer top and CIN in the inversion layer assuming a Gaussian form of vertical velocity distribution near cloud base. The total area under the PDF includes the overall contribution of updraft and downdraft motions in a total area (which includes both clear and cloudy area). The fraction of updrafts at the mixed layer top from this total area reaching the LFC is estimated using PDF by introducing a velocity threshold called critical velocity (w_c). That means the surface parcels from this domain reaching the inversion base having updraft velocities higher than the critical velocity will continue to move upward and reach LFC (Bretherton et al. 2004). The critical velocity is estimated based on the CIN in the inversion layer.

However, CIN calculation is very sensitive and challenging for many reasons. Previous studies have demonstrated the sensitivity of CIN to small changes in surface conditions. A fractional change in the surface temperature ($\sim$ 1 Kelvin) could change the conditions from no convection to intense convection (e.g., Crook 1996). In addition, computing CIN especially for shallow layers (i.e. FWC with average depth < 1 km) is very challenging both using observations as well as models because the magnitude of CIN values is very sensitive to vertical grid spacing. Thus, the practical implementation of the Bretherton et al. (2004) parameterization is questionable.

Estimation of the critical velocity (w_c)

using observations Here, a different approach is used to estimate the critical velocity. From observations, we know the cloud fraction and the detailed vertical air motion PDF at all levels. Thus, if we move from the right edge (strongest updrafts) of the observed hourly vertical velocity PDF until the fractional area under the PDF curve matches the observed updraft fraction, we can estimate the critical velocity. In this study, the critical velocity is estimated using Doppler velocity observations. The critical velocity is defined as the velocity above which surface parcels reaching the inversion base will continue to move upward and reach LFC with zero velocity (Bretherton et al. 2004). The definition used here retained the physical meaning as defined in Bretherton et al. 2004. Figure 5-5 shows the schematic representation of the methodology used to estimate critical velocity from Doppler lidar observations. Hours with fair-weather cumuli (Lower threshold of 5% for FWC cloud fraction) are only considered to estimate critical velocity. The total area (cloudy and clear-air area) can be classified into bulk cloudy and clear-air region as shown in the top panel of Figure 5-5. The bell shaped curve is the PDF (Probability Density of Function) of vertical velocity points in any hour near mixed layer top. The shaded area is the area of updrafts in the cloudy region starting from the right end of the curve. The velocity at the left end of the shaded area is the critical velocity.

The sensitivity of the aforementioned observational-based method for the estimation of the w_c is tested by sampling the vertical air motion PDF at different normalized heights. We found that this approach is stable. The relationship between the observed cloud fraction, vertical velocity variance near to the mixed layer

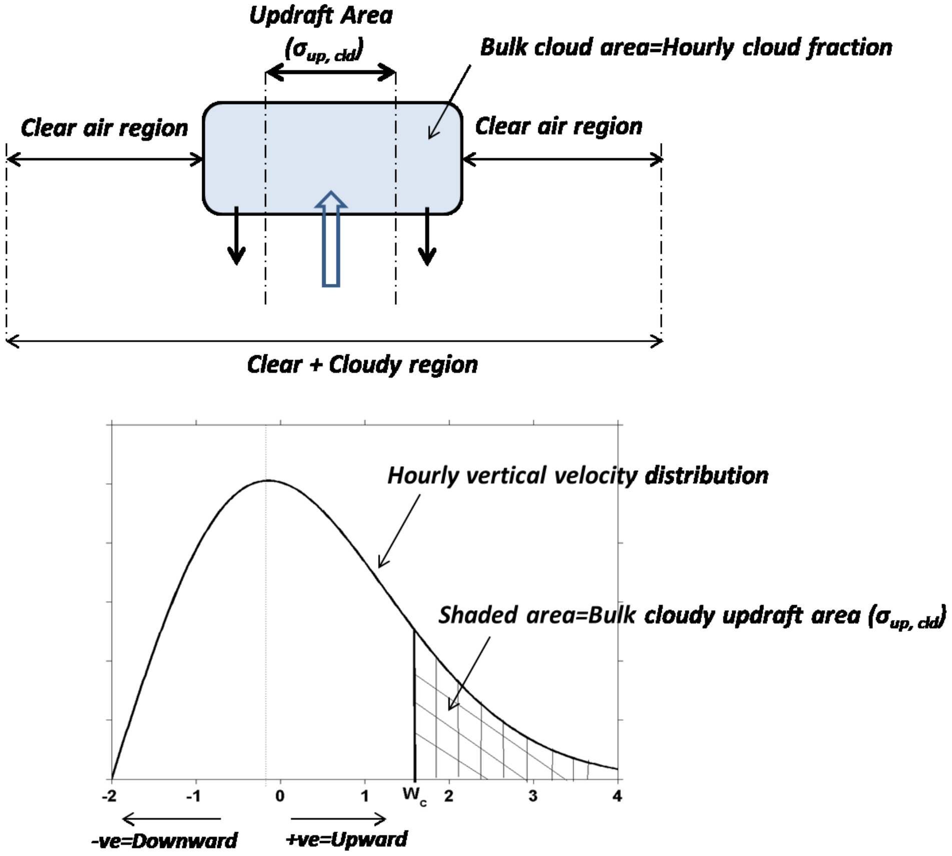

Figure 5–5: Schematic showing the methodology to estimate the critical velocity from the Doppler lidar vertical velocity PDF.

top, critical velocity, and the convective velocity is shown in Fig. 5-6. The events with cloud fraction$>$ 5% are only considered to compute the statistics, which resulted in less FWC hours compared to the total (147 hours) FWC hours. The cloud fraction is estimated from the ceilometer (Fig. 5-6a). The low cloud fraction conditions have higher magnitudes of critical velocities (Fig. 5-6b) compared to the high cloud fraction conditions. This is consistent with the approach used to estimate critical velocity (Higher the critical velocity, only fewer parcels at the mixed layer could make it to the LFC and vice versa). The magnitude of critical velocities observed are comparable to the cloud base velocities reported in FWC using cloud radar observations as discussed in Chapter 4. The time series of hourly vertical velocity variance estimated near mixed layer top are shown in Fig. 5-6c. The variance values shows lot of variability for different cloud cover conditions.

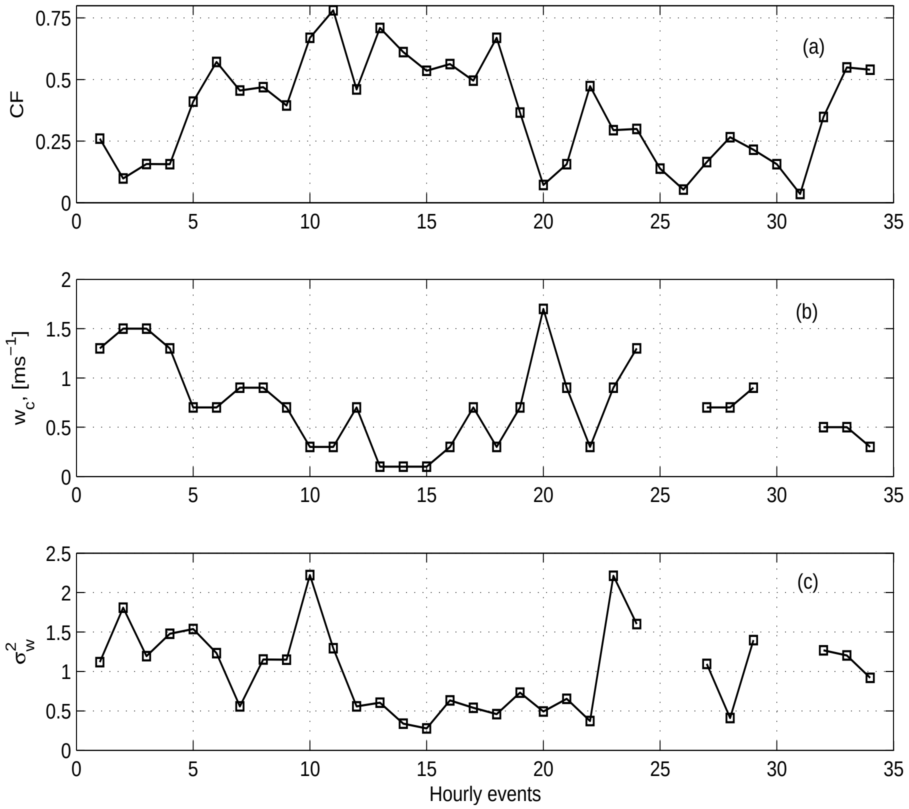

Figure 5–6: Hourly time series of (a) Cloud fraction, (b) Critical velocity [ms^{-1}], (c) Vertical velocity variance [ms^{-1}], (d) Convective velocity [ms^{-1}].

The parameters such as critical velocity, vertical velocity standard deviation and normalized critical velocities at the mixed layer top are plotted for various bins of cloud fraction as shown in Figure 5-7. The critical velocities estimated at the mixed layer top as a function of cloud fraction are shown in Fig. 5-7a. An increase in the magnitude of critical velocity with decreasing cloud fraction is evident. The vertical velocity standard deviations are plotted against various cloud fractions are shown in the Figure 5-7b. The significant variability in the vertical velocity standard deviation values for various cloud fractions would be important to refine the suggestions from the previous studies (Nicholls and Lemone 1980; Grant 2001) on the minor impact of shallow cumulus on subcloud vertical velocity variance by accounting for various cloud fractions. The critical velocities have been normalized with the corresponding vertical velocity standard deviations for various cloud fractions as shown in Figure 5-7c. It is very interesting to note that the normalized critical velocities are scaled linearly with the cloud fraction. This suggests that the variance at the cloud base and the critical velocity influences cloud fraction.

Updraft Properties at the Cloud Base

Using the Bretherton et al. (2004) scheme, the updraft fraction, mean updraft magnitude and updraft mass flux are estimated (see Chapter 1, Eqns 1.6-1.8 for details). The computed updraft properties are compared with those estimated from the Doppler lidar at the cloud base level (5-8). Since CIN computations are not available, the Bretherton et al. (2004) scheme uses the critical velocities and vertical velocity variance values estimated at the mixed layer top from the observations. Thus, we expect that the directly observed and parameterized updraft properties at the mixed layer top to be very similar (Fig. 5-8 a-c panels).

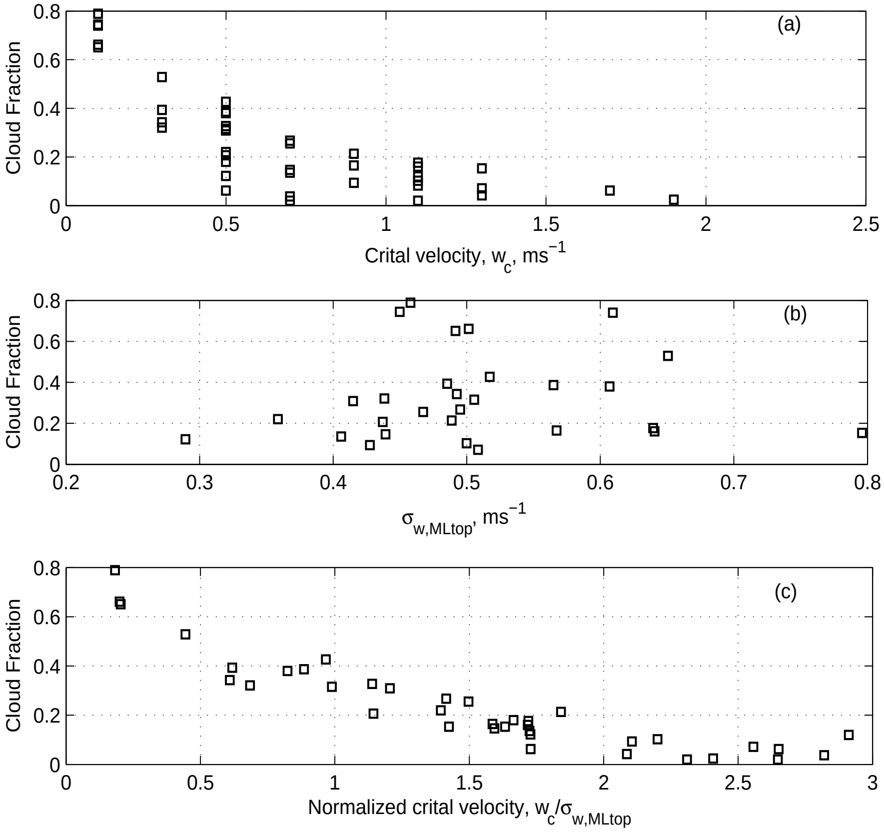

Figure 5–7: Plot of (a) critical velocity (w_c), (b) vertical velocity standard deviation (σ_w), and (c) normalized critical velocity (w_c/σ_w) as a function of cloud fraction.

The updraft fraction estimates agree well at the cloud base (Fig. 5-8a), however it is noticeable that updraft fraction near the cloud base are considerably lower than 1. Here the Bretherton-based estimate of the updraft fraction at the cloud base agrees well with observations because the critical velocity information is based on the updraft fraction and not the cloud fraction. The relationship between the cloud fraction and updraft fraction of the cloudy areas is investigated in the next section.

The comparison of the directly observed (Doppler lidar) and computed (Bretherton et al. (2004)) updraft velocity magnitudes near the cloud base exhibit larger differences (Fig. 5-8b), and these differences are also shown in the updraft mass flux near the cloud base (Fig. 5-8c). It is plausible that these differences are caused by the details of the shape of the vertical air motion PDF near the cloud base. In the Bretherton et al. (2004) scheme, a Gaussian PDF is assumed for the vertical velocity. However, the skewness of the vertical air motion PDF at the cloud base exhibits overall significant positive skewness (Fig. 5-8d). Positive skewed PDF's of vertical air motion are consistent with bottom (surface) forcing and have been observed in the past (e.g., Chapter 3). Nevertheless, none of the aforementioned scheme considers the effects of a non-Gaussian PDF for the vertical air motion. The relationship between the cloud fraction and skewness of the vertical air motion PDF is investigated in the next section.

5.4 Vertical Air Motion PDF statistics

5.4.1 Updraft and downdraft fractions in the sub-cloud layer

Generally, it is assumed that most of the area below the clouds are associated with the updraft regions. This assumption is reasonable when the conditions are predominantly buoyant with no significant wind shear in the CBL. In actual conditions, there is both buoyancy and wind shear. In reality, one should be cautious in studying the connection of clouds with the subcloud layer by bearing in mind the influences of tilting of thermals, advection, shear, fractional cloud cover, etc. Observationally it is difficult to decompose their individual effects, however, documenting frequency and range of variability in updraft and downdraft fractions should be of

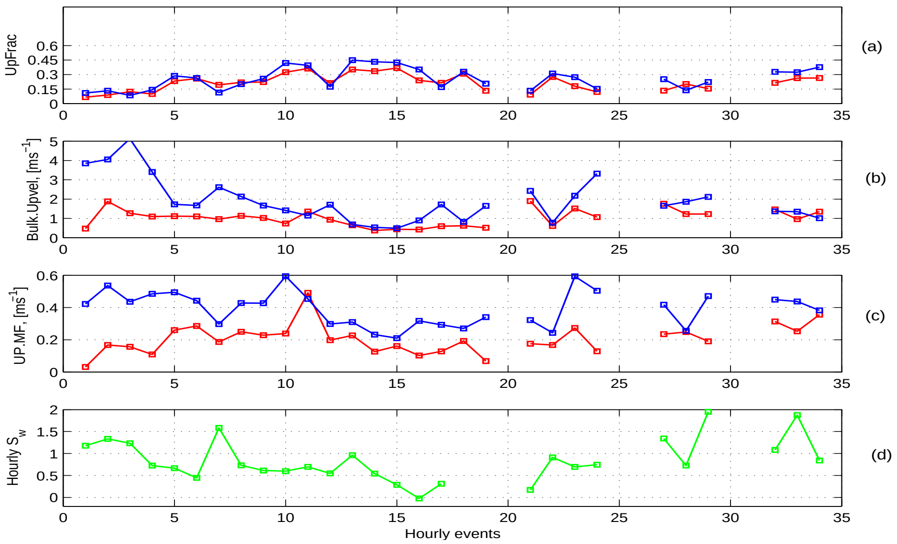

Figure 5–8: Comparison of cloud-base updraft properties between the Bretherton scheme and observations. Red and blue boxes indicates the quantities calculated from lidar observations and estimates from the Bretherton scheme. (a) Active updraft fraction, (b) Bulk updraft velocity (ms^{-1}), (c) Updraft mass flux (M/ρ), ms^{-1}), and (d) Vertical velocity skewness.

high value. The fractional coverage of updraft and downdrafts beneath the clouds at various normalized heights in the CBL for different cloud fractions have been shown in Figure 5-9. Left (right) panel shows the profile of fractional updraft (downdraft) area beneath the clouds in the subcloud region for various cloud fractions. The updraft and downdraft fractions vary from 40–80 % and 20–70 % percent in the subcloud layer respectively. The conditions with low fractional cloud cover have more fractional updraft area in the subcloud regions compared to the high cloud cover conditions. The results are plausible. This is consistent with the previous study by (Kollias and Albrecht (2000)), which reports updraft and downdrafts occupy around 40% of the total cloud area during overcast conditions. The systematic behaviour in updraft fraction profiles for different cloud fraction suggesting the role of cloud cover to estimate the updraft characteristics in mass-flux approaches.

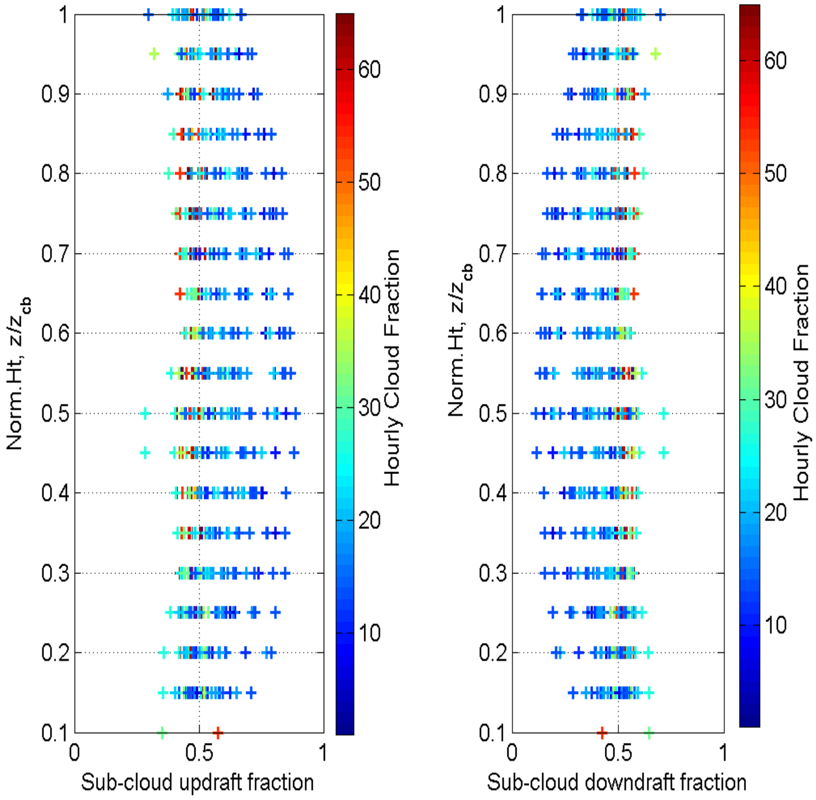

Figure 5–9: Fractional coverage of updraft and downdrafts beneath the clouds at various heights in the subcloud layer for different cloud fractions.

5.4.2 Vertical velocity PDF

The previous analysis considers the fraction of updrafts and downdrafts in the subcloud layer as a function of cloud fraction. Here, we separate the sub-cloud layer vertical air motion field in the cloudy and clear column and we construct the vertical air motion PDFs for these two segments. An example case-study of hourly PDF's of vertical velocity for clear, cloudy, and total periods at various normalized height locations is shown in Figure 5-10. The vertical velocity PDF's have well-defined coherency with height indicating the presence of thermals in the subcloud layer. At low cloud fraction conditions (left column in Fig. 5-10), the PDF of the vertical air motion in cloudy columns exhibits the strongest difference to the total vertical air motion PDF. The shift of the vertical air motion PDF in cloudy regions toward updraft motions is consistent with the results shown in Figure. 5-9. As the cloud fraction increases, the vertical air motion PDFs in cloudy and clear sky segments become more similar.

Using all available Doppler lidar observations within the May-August 2011 period (23-hours, 21-hours and 20-hours of low, median, and high cloud fraction conditions respectively) the vertical air motion PDFs are constructed (Fig. 5.11). The total vertical velocity PDF for each regime is obtained by taking all the vertical velocity points at each hour after normalizing the velocity points in each hour with the respective convective velocities. For each cloud fraction regime, composite PDF's of clear, cloudy, and total periods are obtained by considering all the velocity points in those events. The composite profiles confirms the findings discussed in the above section. The systematic differences in the shape of the PDFs suggests that the fractional area of updrafts in the cloudy region decreases with the increase in cloud fraction.

5.4.3 Vertical velocity skewness

The profiles of hourly vertical velocity skewness as a function of cloud fraction have been shown in Figure 15. The presence of significant skewness in the vertical velocity PDF is often overlooked in mass-flux parameterization schemes (e.g.,

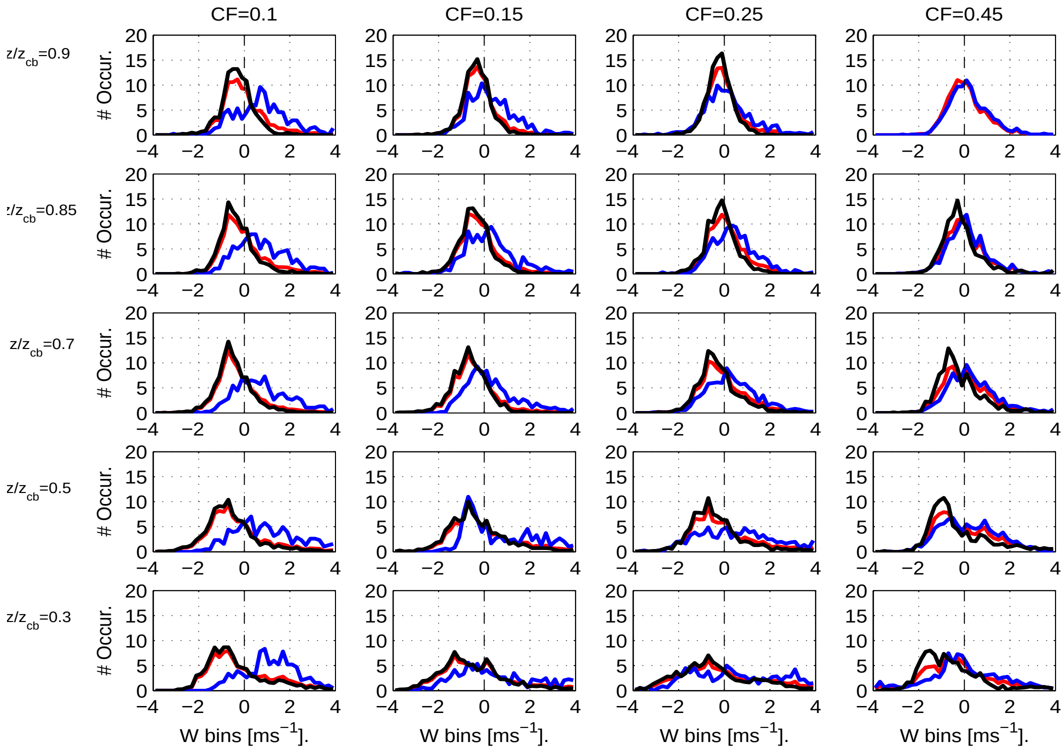

Figure 5–10: Sample of hourly vertical velocity PDF'-s at various normalized heights for clear, cloudy, and total periods. Red, black, and blue color indicates total, clear, and cloudy periods respectively. The label (CF) for each column indicates the hourly cloud fraction.

Bretherton et al. (2004)). Using the same methodology applied in the case of updraft and downdraft fractions as a function of the cloud fraction, the relationship between vertical air motion PDF skewness and cloud fraction is estimated (Fig. 5-12). Overall, the vertical air motion PDF is positively skewed in the CBL. The only exception is during high cloud fraction conditions. As the cloud fraction increases, the role of the cloud as a source of turbulence in the CBL increases and this results to a top (cloud) driven turbulence that leads to negatively skewed vertical air motion

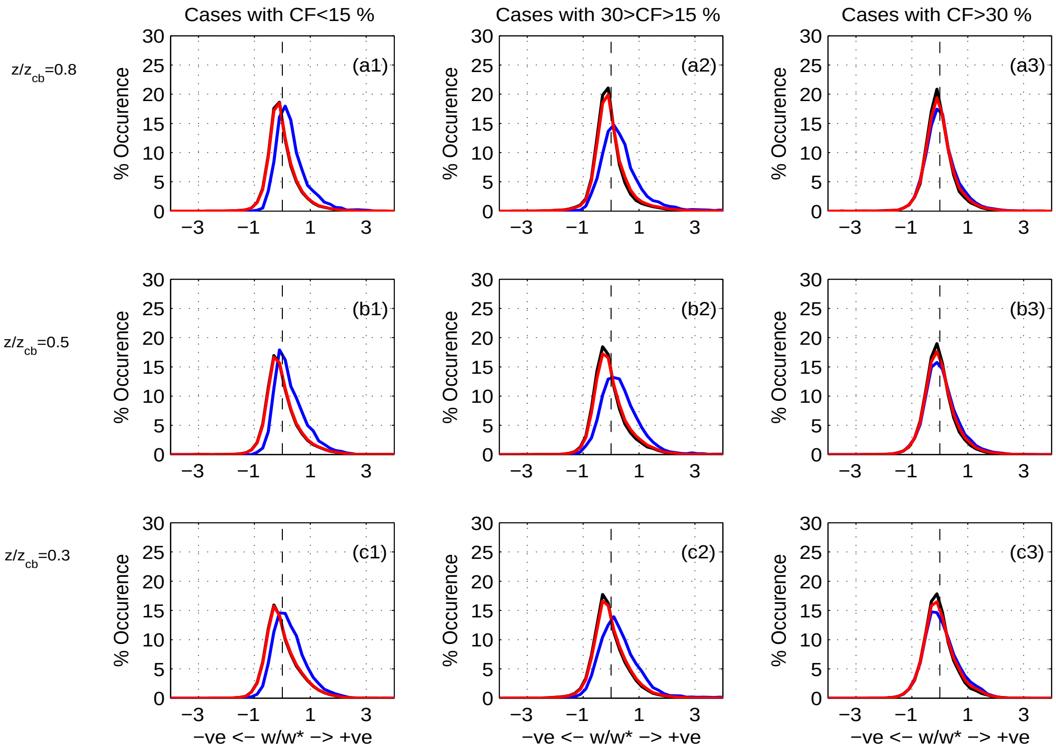

Figure 5–11: Composite vertical velocity PDF'-s for clear, cloudy, and total periods at various normalized locations. Red, black, and blue color indicates total, clear, and cloudy periods respectively. Each profile is obtained by considering the velocity points from all those events in that regime after being normalized with respective convective velocities during that hour.

PDF's. The Doppler lidar data analysis is consistent with results from recent studies (Chandra et al. 2010; Hogan et al. 2009). At lower cloud fraction conditions (below 30%) the skewness is positive with its maximum values at the upper part of the CBL.

5.5 Summary

The potential to use vertical velocity observations from Doppler lidar for turbulent statistics in the subcloud layer during clear and non-precipitating conditions is

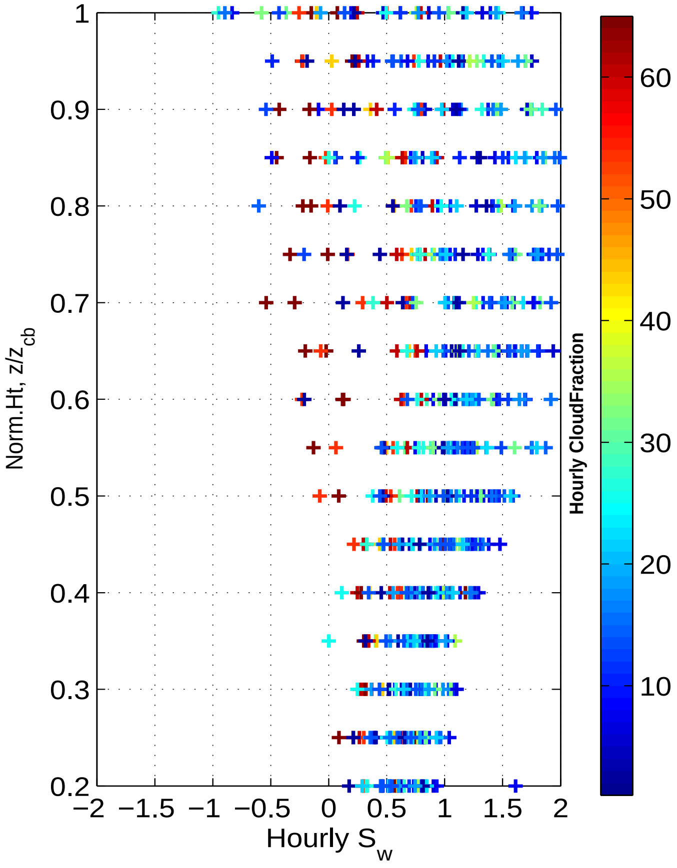

Figure 5–12: Profiles of hourly vertical velocity skewness as a function of cloud fractions.

demonstrated. The Doppler lidar observations provided an opportunity to test some aspects of the existing mass-flux schemes. The performance of these schemes over land is tested with the observations. The vertical velocity in the subcloud layer is analyzed separately by decomposition into cloudy and clear-air regions to understand the interaction between cloud and subcloud layer.

The updraft aspects from two mass-flux schemes have been evaluated with the observations to test its applicability over land. Both schemes showed significant differences with the observations. In the convective velocity approach, the linear relationship proposed by Grant (2001) between mass-flux and convective velocity based on oceanic conditions, exhibits little skill over land. The bulk updraft velocity in the cloudy region near cloud base seems to have a linear relationship with the convective velocity. In the Bretherton et al. (2004) approach, a new alternative method to estimate critical velocity is proposed from observations. The estimates from this approach can be used as a constraint in models to get proper vertical velocity distributions. There are significant differences between the updraft parameters calculated from this scheme with the observations. The skewness values from lidar observations near cloud base have significant deviations from the Gaussian assumption. This suggests that accounting for non-Gaussian variability may play an important role.

The vertical velocity observations in the subcloud layer are analyzed for various cloud conditions by separately decomposing into clear and cloudy regions and for various cloud fractions. The investigation reveals that the characteristics of vertical velocity PDF's in the subcloud layer shows systematic differences for various fractional cloud cover. It suggests that low fractional cloud cover conditions have higher fractional updrafts in cloudy region compared to the conditions with high fractional cloud cover. These initial findings gave new insights about the role of cloudiness in influencing the subcloud structure. The detailed analysis about the factors controlling the shape of the PDF is the future scope for further investigation.

CHAPTER 6
Final remarks

The daytime evolution of the CBF turbulence and associated cloudiness over land present significant challenges. Furthermore, there is a luck of comprehensive long-term observations to provide observational targets for BL models. The ARM facility at the SGP has long-record of observations from various instrument platforms, combined with the homogeneous geography and variable synoptic conditions that lead to seasonal cloud variability. The strength of the ARM observations at the SGP site is the long record (14 years), which is sufficient to generate robust statistics of the daytime evolution of the CBL and associated cloudiness. However, over the course of our work, several challenges and limitations were identified. Throughout the presented study, the most significant limitation was the limited sensitivity of the MMCR. In fact, the MMCR is one of the most sensitive ground-based radars, however, a significant fraction of FWC's (especially those with LWP of $\sim 50\ gm^{-2}$ or less) were not detected by the MMCR. The overall continental nature of the ARM SGP site results in shallow cumuli with high number concentrations of cloud droplets (e.g., Vogelmann et al. 2012) and thus low radar reflectivity values. Second, we faced the challenge of separating insects from clouds as significant fraction of cloud observations were contaminated with the insect echoes. To solve this issue, a new fuzzy–logic algorithm was developed to remove insect contamination. Though the original data set was reduced due to these constraints, it didn't limit the scope of its utilization for addressing the aspects such as diurnal cycle and composite statistics. The fuzzy-logic based insect classification algorithm was applied to the entire process entire 14 years of cloud radar vertical velocity data used for calculating FWC geometrical properties, composites of turbulent statistics, and their daytime evolution. While dealing with the challenges of removing insect echoes, the potential of using radar insect echoes to study subcloud layer turbulence characteristics. The long-term (4 years) data set of insect radar echoes was used to document the turbulent structure of the subcloud layer and its daytime evolution. These two long-term analyses provide a unique insight into the role of cloudiness on turbulent energy budget in CBL, and the daytime evolution of turbulence statistics in CBL as well as FWC.

During April-May 2011, the Mid-latitude Continental Convective Clouds Experiment (MC3E)field campaign involving NASA and ARM investigators was conducted in south-central Oklahoma to address various components of convective parameterization (http://campaign.arm.gov/mc3e/). During the MC3E new and enhanced observations were available. In particular, observations from a new Doppler lidar system, high frequency soundings (8 per day), multi-frequency radars and aircraft measurements. The vertical velocity observations from the Doppler lidar gave us an unique opportunity to understand the subcloud characteristics in detail. The good height coverage (up to the cloud base during convective conditions) of vertical velocity observations gave us a confidence of using them to study subcloud characteristics up to the mixed layer top during both clear and non-precipitating FWC conditions.

The Doppler lidar observations were initially screened for low Signal-to-Noise conditions and subsequently used to study the subcloud layer turbulence for variable cloud fraction conditions. In particular, the boundary layer column was classified as cloudy or clear and vertical velocity statistics were derived for each regime. Using the high resolution Doppler lidar observations several assumptions used in well established mass-flux based parameterizations of BL cloudiness were tested.

6.1 Summary of key findings

6.1.1 Turbulent structure of the Convective Boundary Layer at the ARM Southern Great Plains Facility

The normalized vertical velocity variance profiles exhibit a smooth daytime evolution with the maximum turbulent activity observed between 1400 and 1500 LST.

During clear-sky conditions, the maximum in normalized variance is observed around $\frac{z}{z_i}$=0.3, and the magnitude of the variance is relatively higher during clear-sky conditions as compared to during cumulus-topped conditions.

Evidence for the effect of clouds in the subcloud layer turbulence budget is found in the vertical structure of the normalized variance for high cloud fraction conditions.

The vertical velocity skewness during clear-sky conditions is positive and higher compared to its value during cumulus-topped conditions. During cumulus-topped conditions, negative skewness is observed near the top of the subcloud layer, indicating the interaction between the subcloud layer and cloud layer.

Updraft mass-flux calculations using a direct sampling technique and the conditional sampling technique suggest that coherent structures (thermals) are responsible for more than 80% of the total turbulent transport observed by the radar in the boundary layer during clear-sky and cumulus-topped conditions. These statistics would address what fraction of a turbulence statistic must be accounted for by the subgrid parameterizations of large eddy simulations.

6.1.2 Multi-year, Summertime Observations of Daytime Fair-Weather Cumuli at the ARM Southern Great Plains Facility

There is a noticeable variability in the inter-annual occurrence of summer-time FWC (from a mininum of 2-4 % to a maximum of 12-17 %) with maximum occurrence observed every four years. The results confirm that the summer time shallow FWC at SGP contain small amounts of liquid water content with liquid water path peaks at 30-60 gm^{-2} and the cloud radar sensitivity fails to detect the significant fraction of thin clouds with LWP$<$ 50 gm^{-2}.

The insect contamination has considerable impact on the ARSCL reported cloud tops and LWP-cloud thickness relations. The cloud thickness is overestimated by more than a factor of two for lower LWP values but it is slightly underestimated for higher LWP values. The adjusted LWP-cloud thickness relation using FL derived cloud tops follows near linear relationship, which is consistent with the clouds that experience condensational growth in the absence of precipitation.

It is observed that the typical occurrence of FWC cloud thickness values are 300-600 m and cloud chord length is $\sim$ 200 m. The maximum occurrence of aspect ratio in FWC is $\sim$0.5, indicating the dominance of tower like clouds with vertical extent higher than their horizontal dimensions. The distribution of normalized cloud chord diameter density follows power law with a clear scale break at $\sim$ 1000 m, which compares well with the previous studies.

The maximum in the mean cloud base mass flux occurred between noon and 2:00 pm with a magnitude of 0.05 $kgm^{-2}s^{-1}$ while drops to minimum towards morning and evening periods. The timing of maximum in the cloud base mass flux coincides with the maximum in the updraft fraction and the surface buoyancy flux indicating the association of clouds to the surface forcing.

The magnitude and timing of cloud base mass flux values in this study are comparable to the previous studies. The mean updraft velocity at the cloud base is 0.8 ms^{-1} and maximum occurs between 1:00 and 2:00 pm, which is comparable to that reported in previous studies (Kollias and Albrecht 2010). The maximum in the mean updraft fraction is $\sim$ 6 % occurring between 1:00 and 2:00 pm. The LCL values and the cloud boundaries (cloud base and tops) have a strong daytime variation with the lowest values observed during morning, and cloud boundaries and LCL reaches maximum between 2:00 and 3:00 pm and 3:00 and 4:00 pm respectively.

The timing of the LWP (convective activity) shows a maximum value of 120 gm^{-2} between 1:00 and 4:00 pm, indicating that clouds at this time are in their matured stage of their life cycle and suggests that the cloud layer quickly adjusts to the surface forcing. The cloud fraction has a weak diurnal variation and a mean value of 0.12.

The hourly mean vertical velocities both at the cloud base and cloud tops are close to zero, suggesting that the fractional area of updrafts inside the clouds compensates the downdraft area, which is consistent with the previous observations in shallow, non-precipitating cumulus clouds. The hourly vertical velocity skewness values both at the cloud base and tops have lot of variability close to zero, which is quite interesting because cloud parameterization schemes (e.g., Bretherton et al. 2004) assume a Gaussian (Skewness=0) vertical velocity distributions at the cloud base.

The normalized profiles of updraft mass flux inside the cloud shows a maximum at the middle of the cloud layers that occurs between 12:00-14:00 LST. The updraft fraction in the profiles increases from the cloud base to about the middle of the cloud layer, and then decreases with height; but the updraft velocity profiles show an increase with height through the entire cloud layer.

6.1.3 Evaluating updraft characteristics in mass-flux schemes using Doppler Lidar observations

The updraft aspects from two mass-flux schemes (Bretherton et al. 2004; Grant 2001) have been evaluated with the observations to test its applicability over land. Both schemes showed significant differences with the observations.

In the convective velocity approach (Grant 2001), the linear relationship proposed between mass-flux and convective velocity based on oceanic conditions, exhibits little skill over land. The bulk updraft velocity in the cloudy region near cloud base seems to have some correlation with the convective velocity.

In this study, a new alternative method to estimate critical velocity is proposed from observations. The estimates from this approach can be used as a constraint in models to get proper vertical velocity distributions. There are significant differences between the updraft parameters calculated from this scheme with the observations.

The skewness values from lidar observations near cloudbase have significant deviations from the Gaussian assumption. This suggests that accounting for non-Gaussian variability may play an important role in velocity PDF based schemes.

The vertical velocity observations in the subcloud layer are analyzed for various cloud conditions by separately decomposing into clear and cloudy regions and for various cloud fractions. The investigation reveals that the characteristics of vertical velocity PDF's in the subcloud layer shows systematic differences for various fractional cloud covers. It suggests that low fractional cloud cover conditions have higher fractional updraft in cloudy region compared to the conditions with high fractional cloud cover. These initial findings gave new insights about the role of cloudiness in influencing the subcloud structure.

6.2 Limitations of the present study

The present study is based on observations from a specific location. Consequently, some of the results reported here may not be representative for other regions because of differences in geography, meteorological conditions, climate, etc. For example, 1) The FWC occurences may vary depending on the large scale conditions. 2) Cloud fraction and liquid water distribution inside the clouds are influenced by the aerosol concentrations. 3) Large scale subsidence may influence the mixed layer depth through entrainment. 4) Surface conditions (e.g., surface Bowen ratio) may influence the entrainment through entrainment moisture flux. Thus, in order to generalize the present results, one needs to understand the influence of each parameter on a particular process.

Unlike models, observations lack this flexibility as models have control over all the state variables to study the cause and effect relationships. The main emphasis of the present study is on the effective utilization of profiling observations from cloud radars and doppler lidars. However, profiling observations have some shortcomings. While the vertical structure of the clouds is well capture, it is unclear which part of the FWC is observed (edge, center etc.). Observations from profiling mode do not account for the variability in cloud boundaries and in-cloud variables (e.g., reflectivity, doppler velocity) in other dimensions, which may influence some of the statistics (e.g., cloud aspect ratio, chord length, plume widths, etc.) presented here.

The main focus here is on the effective utilization of long-term vertical velocity observations to address some key aspects in CBL and FWC. In reality, apart from vertical velocity, temperature and humidity observations are also equally important for comprehensive understanding of the turbulent structure in CBL, FWC, and subcloud-cloud coupling. Though there were 14 years of MMCR observations, the MMCR missed a significant fraction of non-precipitating FWC population because of high aerosol loading at the SGP site. Thus, unfortunately, the full potential of MMCR system could not be utilized.

6.3 Future Work

During the completion of the presented study, several challenges associated with the available measurements and the particularities of the SGP site were identified. Using this knowledge, future work in FWC could benefit from the following:

The MMCR misses significant population of FWC clouds at SGP due to high aerosol loading. In addition to this, the presence of a deep layer of insects makes the analysis of observations more challenging. The future scope is to extend the present methodology to the marine clouds (where typically there is low aerosol loading), thus, full advantage of the MMCR systems can be explored to better characterize the internal structure of the clouds. The recent announcement by the ARM program that the Azores will be a permanent fixed site offers a location with abundance of FWC (Remillard et al. 2012) with lower aerosol loading and the present methodology is applied. The present methodology and retrieval algorithms only focussed on the non-precipitating porting clouds due to the limitations of cloud radars. The higher wavelength radars (such as X, C, and S Band) offers an advantage by overcoming the limitations of cloud radars (e.g., attenuation, aliasing, etc) to probe precipitating clouds and precipitation. The future scope is to explore and merge the individual strength of these radars to address the present limitations to study beyond non-precipitating clouds.

The present study demonstrated the potential capabilities of Doppler lidar for studying subcloud layer, and careful utilization of lidar observations for testing some of the aspects of mass-flux parameterization using short-term data set. The future scope is to extend the present analysis to long-term data set to better understand the factors controlling the shape of vertical velocity PDF's in different regimes. This would be very useful for evaluating existing parameterization schemes for various regimes.

Some of the shortcoming of using profiling mode could be addressed by utilizing the scanning capabilities of cloud radar and Doppler lidar. The scanning capabilities of cloud radars could provide horizontal winds inside clouds, information about in-cloud circulations, and horizontal variability of the cloud variables, which would be useful to validate the present statistics (e.g., cloud chord length, cloud aspect ratio) and to understand the 3D structure of clouds. Scanning capabilities of Doppler lidar could be very useful to fill the gaps in lack of high resolution horizontal winds within CBL, and for studies including BL rolls and convergent lines with in CBL, which are one of the least studied areas.

The primary focus of present study is thus mainly on hourly statistics. But, one can utilize these data sets to look for other aspects (e.g., scale interactions in CBL, long term trends, etc.) using other techniques such as frequency analysis, principle component analysis, etc.

References

Achtemeier, G. L., 1991: The use of insects as tracers for clearair boundary-layer studies by Doppler radar. *J. Atmos. Oceanic Technol.*, **8**, 746–765.

Albrecht, B. A., 1979: A Model of the Thermodynamic Structure of the Trade-Wind Boundary Layer: Part I. wave–driven circulation of the mesosphere. *J. Atmos. Sci.*, **60**, 103–118.

Albrecht, B. A., 1981: Parameterization of trade-cumulus cloud amounts. *J. Atmos. Sci.*, **38**, 97–105.

Benner, T. C. and J. A. Curry, 1989: Characteristics of small tropical cumulus clouds and their impact on the environment. *J. Geophys. Res.*, **103**.

Berg, L. K. and E. I. Kassianov, 2008: Temporal variability of fair-weather cumulus statistics at the ACRF SGP site. *J. Climate.*, **21**, 3344–3358.

Berg, L. K. and R. B. Stull, 2005: A simple parameterization coupling the convective boundary layer and fair-weather cumuli. *J. Atmos. Sci.*, **62**, 1976–1988.

Betts, A. K., 1973: Non-precipitating cumulus convection and its parameterization. *Quart. J. Roy. Meteor. Soc.*, **99**, 178–196.

Betts, A. K., 1975: Parametric interpretation of trade-wind cumulus budget studies. *J. Atmos. Sci.*, **32**, 1934–1945.

Betts, A. K. and P. Viterbo, 2005: Land-surface, boundary-layer, and cloud-field coupling over the southwestern Amazon in ERA-40. *J. Geophys. Res.*, **100**, 1–15.

Blyth, A. M. and J. Latham, 1985: An airborne study of vertical structure and microphysical variability within a small cumulus. *Quart. J. Roy. Meteor. Soc.*, **111**, 773–792.

Bolton, D., 1980: The computation of equivalent potential temperature. *Mon. Wea. Rev.*, **108**, 1046–1053.

Bony, S., et al., 2006: How well do we understand and evaluate climate change feedback processes. *J. Climate.*, **19**, 3445–3482.

Bretherton, C. S., J. R. McCaa, and H. Grenier, 2004: A New Parameterization for Fair-weather cumuli Convection and Its Application to Marine Subtropical Cloud-Topped Boundary Layers. Part I: Description and 1D Results. *Mon. Wea. Rev.*, **132**, 864–882.

Brown, A. R., et al., 2002: Large-eddy simulation of the diurnal cycle of fair-weather cumuli convection over land. *Quart. J. Roy. Meteor. Soc.*, **128**, 1075–1094.

Cahalan, R. F. and J. H. Joseph, 1989: Fractal statistics of cloud fields. *Mon. Wea. Rev.*, **117**, 261–272.

Chandra, A. S., P. Kollias, S. Giangrande, and S. Klein, 2010: Long-Term Observation of the Convective Boundary Layer Using Insect Radar Returns at the SGP ARM Climate Research Facility. *J. Climate*, **23**, 5699–5714.

Clothiaux, E. E., T. P. Ackerman, G. G. Mace, K. P. Moran, R. T. Marchand, M. A. Miller, and B. E. Martner, 2000: Objective determination of cloud heights and radar reflectivities using a combination of active remote sensors at the ARM CART Sites. *J. Appl. Meteor.*, **39**, 645–665.

Couvreux, F., F. Hourdin, and C. Rio, 2010: Resolved versus parametrized boundary-layer plumes. Part I:Aparametrization-oriented conditional sampling in large-eddy simulations. *Bound.-Layer Meteor.*, **134**, 441–458.

Cuijpers, J. W. M. and P. G. Duynkerke, 1993: Large eddy simulation of trade wind cumulus clouds. *J. Atmos. Sci.*, **50**, 3894–3908.

David, C. T. and J. Hardie, 1998: The visual responses of freeflying summer and autumn forms of the black beam aphid, Aphis fabae, in an automated flight chamber. *Physiol. Entomol.*, **13**, 277–284.

Deardorff, J. W., 1974: Three-dimensional numerical study of the height and mean structure of a heated planetary boundary layer. *Boundary-Layer Meteorology.*, **7**, 81–106.

DeRoode, S. R. and C. S. Bretherton, 2003: Mass-flux budgets of shallow cumulus clouds. *J. Atmos. Sci.*, **60**, 137–151.

Echternacht, K. L. and M. Garstang, 1976: Changes in the structure of the tropical subcloud layer from the undisturbed to the disturbed states. *Mon. Wea. Rev.*, **104**, 407–417.

Ecklund, W. L., D. A. Carter, and B. B. Balsley, 1988: A UHF Wind Profiler for the Boundary Layer: Brief Description and Initial Results. *J. Atmos. Oceanic. Technol.*, **5**, 432–441.

Emanuel, K. A. and D. J. Raymond, 1992: Report from a workshop on cumulus parameterization. *Bull. Amer. Meteor. Soc.*, **73**, 318–325.

Esbensen, S., 1975: An analysis of subcloud-layer heat and moisture budgets in the western Pacific trades. *J. Atmos. Sci.*, **32**, 1921–1923.

Feingold, G., W. L. Eberhard, D. E. Veron, and M. Previdi, 2003: First measurements of the twomey aerosol indirect effect using ground-based remote sensors. *Geophys. Res. Lett.*, **52**, 2788–2799.

Frehlich, R., 2001: Estimation of velocity error for Doppler lidar measurements. *J. Atmos. Oceanic Technol.*, **18**, 1628–1639.

French, J. R., G. Vali, and R. D. Kelly, 1999: Evolution of small cumulus clouds in florida: Observations of pulsating growth. *Atmos. Res.*, **52**, 143–165.

Garratt, J. R., 1994: The Atmospheric Boundary Layer. *Cambridge University Press.*, **1994-04-21**, 336.

Ghate, V., M. A. Miller, and L. DiPretore, 2011: Vertical velocity structure of marine boundary layer trade wind cumulus clouds. *J. Geophys. Res.*, **116-D16206**, doi:10.1029/2010JD015 344.

Goke, S. and Coauthors, 2007: Radar analysis of precipitation initiation in maritime versus continental clouds near the Florida coast: Inferences concerning the role of CCN and giant nuclei. *J. Atmos. Sci.*, **64**, 3695–3707.

Gossard, E. E., R. B. Chadwick, W. D. Neff, and K. P. Moran, 1982: Use of ground-based Doppler radars to measure gradients, fluxes and structure parameters in elevated layers. *J. Appl. Meteor.*, **21**, 211–226.

Grant, A. L. M., 2001: Cloud-base fluxes in the cumulus-capped boundary layer. *Quart. J. Roy. Meteor. Soc.*, **127**, 407–421.

Greenhut, G. K. and S. J. S. Khalsa, 1987: Convective elements in the marine atmospheric boundary layer. Part I: Conditional sampling statistics. *J. Climate Appl. Meteor.*, **26**, 813–822.

Grimsdell, A. W. and W. M. Angevine, 1998: Convective boundary layer height measurement with wind profilers and comparison to cloud base. *J. Atmos. Oceanic. Technol.*, **15**, 1331–1338.

Grund, C. J., R. M. Banta, J. L. George, J. N. Howell, M. J. Post, R. A. Richer, and A. M. Weickmann, 2001: Interpretation of the fluctuating echo from randomly distributed scatterers. *J. Atmos. Oceanic. Technol.*, **18**, 376–393.

Hogan, R. J., A. L. M. Grant, A. J. Illingworth, G. N. Pearson, and E. J. O'Connor, 2009: Vertical velocity variance and skewness in clear and cloud-topped boundary layers as revealed by Doppler lidar. *Quart. J. Roy. Meteor. Soc.*, **135**, 635–643.

Issac, G., P. Joe, and P. W. Summers, 1984: *The vertical transport and redistribution of pollutants by clouds, in Meteorology of Acid Deposition.* 1st ed., Edited by P. J. Samson, Air pollut. Control Assoc, Pittsburgh., 450 pp pp.

Jiang, H., G. Feingold, H. H. Jonsson, M. L. Lu, P. Y. Chuang, R. C. Flagan, and J. H. Seinfeld, 2008: Statistical comparison of properties of simulated and observed cumulus clouds in the vicinity of Houston during the Gulf of Mexico Atmospheric Composition and Climate Study (GoMACCS). *J. Geophys. Res.*, **113-D13205**, doi:10–1029/2007JD009 304.

Johnson, R. H., 1977: Effects of cumulus convection on the structure and growth of the mixed layer over south Florida. *Mon. Wea. Rev.*, **105**, 713–724.

Kaimal, J. C. and J. J. Finnigan, 1994: Atmospheric Boundary Layer Flows; Their Structure and Measurement. *Oxford University Press.*, **ISBN-0-19-506239-6**, 289.

Kaimal, J. C., J. C. Wyngaard, D. A. H. O. R. Cote, Y. Izumi, S. J. Caughey, and C. J. Readings, 1976: Turbulent structure in the convective boundary layer. *J. Atmos. Sci.*, **33**, 2152–2169.

Khalsa, S. J. S. and G. K. Greenhut, 1987: Convective elements in the marine atmospheric boundary layer. Part II: Entrainment at the capping inversion. *J. Climate Appl. Meteor.*, **26**, 824–836.

Kollias, P. and B. A. Albrecht, 2000: The turbulence structure in a continental stratocumulus cloud from millimeter wavelength radar observations. *J. Atmos. Sci.*, **57**, 2417–2434.

Kollias, P. and B. A. Albrecht, 2010: Vertical Velocity Statistics in Fair-Weather Cumuli at the ARM TWP Nauru Climate Research Facility. *J.Climate.*, **23**, 6590–6604.

Kollias, P., B. A. Albrecht, R. Lhermitte, and A. Savchenko, 2001: Radar observations of updrafts, downdrafts, and turbulence in fair-weather cumuli. *J. Atmos. Sci.*, **58**, 1750–1766.

Kollias, P., E. E. Clothiaux, M. A. Miller, B. A. Albrecht, G. L. Stephens, and T. P. Ackerman, 2007: Millimeter Wavelength Radars: New Frontier in Atmospheric Cloud and Precipitation Research. *Bull. Amer. Meteor. Soc.*, **88**, 1608–1624.

Lane, D. E., K. Goris, and R. C. J. Somerville, 2002: Radiative transfer through Broken Clouds: Observations and Model Validation. *J. Climate*, **15**, 2921–2933.

Lemone, M. A., 1980: Some observations of vertical velocity skewness in the convective planetary boundary layer. *J. Atmos. Sci.*, **47**, 1163–1169.

Lemone, M. A. and W. T. Pennell, 1976: The relationship of trade wind cumulus distribution to subcloud layer fluxes and structure. *Mon. Wea. Rev.*, **104**, 524–539.

Lenderink, G., et al., 2004: The diurnal cycle of fair-weather cumuli clouds over land: A single -column model intercomparison study. *Quart. J. Roy. Meteor. Soc.*, **130**, 3339–3364.

Lenschow, D. H., 1970: Airplane measurements of planetary boundary layer structure. *J. Appl. Meteor.*, **9**, 874–884.

Lenschow, D. H., J. C. Wyngaard, and W. T. Pennell, 1980: Mean-field and second-moment budgets in a baroclinic, convective boundary layer. *J. Atmos. Sci.*, **37**, 1313–1326.

Lhermitte, R., 1987: A 94 GHz Doppler Radar for Cloud Observations. *J. Atmos. Oceanic Technol.*, **4**, 36–48.

Liljegren, J. C., E. E. Clothiaux, G. G. Mace, S. Kato, and X. Dong, 2001: A new retrieval for cloud liquid water path using a ground-based microwave radiometer and measurements of cloud temperature. *J. Geophys. Res.*, **106**, 14,485–14,500.

Luke, E., 2008: A technique for the automatic detection of insect clutter in cloud radar returns. *J. Atmos. Oceanic Technol.*, **25**, 1498–1513.

Marshal, J. S. and W. Hitschfeld, 1953: Interpretation of the fluctuating echo from randomly distributed scatterers. *Canada. J. Phys.*, **31**, 962–994.

Miao, Q., B. Geerts, and M. Lemone, 2006: Vertical velocity and buoyancy characteristics of coherent echo plumes in the convective boundary layer, detected by a profiling airborne radar. *J. Appl. Meteor. Climatol.*, **45**, 838–855.

Moeng, C. H., 1984: A large-eddy-simulation model for the study of planetary boundary-layer turbulence. *J. Atmos. Sci.*, **41**, 2052–2062.

Moeng, C. H. and R. Rotunno, 1990: Vertical-velocity skewness in the buoyancy-driven boundary layer. *J. Atmos. Sci.*, **47**, 1149–1162.

Monin, A. S. and A. M. Obukhov, 1954: Basic laws of turbulent mixing in the surface layer of the atmosphere. *Tr. Akad. Nauk SSSR Geofiz. Inst.*, **24**, 163–187.

Moran, K. P., B. E. Martner, M. J. Post, R. A. Krofli, D. C. Welsh, and K. B. Widener, 1998: An unattended cloud-profiling radar for use in climate research. *Bull. Amer. Meteor. Soc.*, **79**, 443–455.

Moyer, K. A. and G. S. Young, 1991: Observations of vertical velocity skewness within the marine stratocumulus-topped boundary layer. *J. Atmos. Sci.*, **48**, 403–410.

Neggers, R. A. J., H. J. J. Jonker, and A. P. Seibesma, 2003: Size Statistics of Cumulus Cloud Populations in Large-Eddy Simulations. *J. Atmos. Sci.*, **60**, 1060–1074.

Neggers, R. A. J., A. P. Seibesma, G. Lenderink, and A. A. M. Holtslag, 2004: An evaluation of mass flux closures for diurnal cycles of fair-weather cumuli. *Mon. Wea. Rev.*, **132**, 2525–2538.

Nicholls, S. and M. A. Lemone, 1980: The fair weather boundary layer in GATE: The relationship of subcloud fluxes and structure to the distribution and enhancement of cumulus clouds. *J. Atmos. Sci.*, **37**, 2051–2067.

Norris, J. R., 1998: Low cloud type over the ocean from surface observations. Part II:Geographical and seasonal variations. *J. Climate.*, **11**, 383–403.

Ooyama, K., 1971: A theory on parameterization of cumulus convection. *J. Meteor. Soc. Japan.*, **49**, 744–756.

Rauber, R. M. and Coauthors, 2007: A supplement to Rain in Shallow Cumulus over the Ocean: The RICO campaign. *Bull. Amer. Meteor. Soc.*, **88**, 512–518.

Remillard, J., P. Kollias, E. Luke, and R. Wood, 2012: Marine Boundary Layer Cloud Observations in the Azores. *J. Climate.*, **doi:10.1175/JCLI-D-11-00610.1**, In press.

Reynolds, A. M. and D. R. Reynolds, 2008: Aphid aerial density profiles are consistentwith turbulent advection amplifying flight behaviours: abandoning the epithet passive. *Proceedings of the Royal Society.*, **London**, 275.

Richter, J. H., D. R. Jensen, V. R. Noonkester, and J. B. Kreasky, 1973: Remote radar sensing: atmospheric structure and insects. *Science.*, **180**, 1176–1178.

Riley, J. R., 1992: A millimetric radar to study the flight of small insects. *Electron. Commun. Eng. J.*, **4**, 43–48.

Riley, J. R. and D. R. Reynolds, 1979: Radar-based studies of the migratory flight of grasshoppers in the middle Niger area of Mali. *Proc. Roy. Soc. London.*, **B204**, 67–82.

Rio, C. and F. Hourdin, 2008: A thermal plume model for the convective boundary layer: Representation of cumulus clouds. *J. Atmos. Sci.*, **65**, 407–425.

Rogers, R. R., W. L. Ecklund, D. A. Carter, K. S. Gage, and S. A. Ethier, 1993: Research Applications of a Boundary-Layer Wind Profiler. *Bull. Amer. Meteor. Soc.*, **74**, 567–580.

Rooy, W. C. D. and A. P. Seibesma, 2008: A simple parameterization for detrainment in fair-weather cumuli. *Mon. Wea. Rev.*, **136**, 560–576.

Russell, R. W. and J. W. Wilson, 1997: Radar-observed fine lines in the optically clear boundary layer: Reflectivity contributions from aerial plankton and its predators. *Bound.-Layer Meteor.*, **82**, 235–262.

Schaefer, G. W., 1976: Radar observations of insect flight. *Proceedings of the Symposium of the Royal Entomology Society*, **7**, 157–197.

Schmidt, H. and U. Schumann, 1989: Coherent structure of the convective boundary layer derived from large-eddy simulations. *J. Fluid. Mech.*, **200**, 511–562.

Schumann, U. and C. H. Moeng, 1991: Plume budgets in clear and cloudy convective boundary layers. *J. Atmos. Sci.*, **48**, 1758–1770.

Seibesma, A. P. and J. W. M. Cuijpers, 1995: Evaluation of parametric assumptions for shallow cumulus convection. *J. Atmos. Sci.*, **52**, 650–666.

Seibesma, A. P., et al., 2003: A large eddy simulation intercomparison study of fair-weather cumuli convection. *J. Atmos. Sci.*, **60**, 1201–1219.

Shen, S. and M. Y. Leclerc, 1995: How large must surface inhomogeneities be before they influence the convective boundary layer structure? A case study. *Quart. J. Roy. Meteor. Soc.*, **121**, 1209–1228.

Sommeria, G. and M. A. Lemone, 1978: Direct testing of a threedimensional model of the planetary boundary layer against experimental data. *J. Atmos. Sci.*, **35**, 25–39.

Spinhirne, J. D., 1993: Micro pulse lidar. *IEEE.Transactions Geoscience Remote Sensing*, **31**, 48–55.

Squires, 1958: Penetrative downdraughts in cumuli. *Tellus*, **10**, 381–389.

Stevens, B. and Coauthors, 2001: Simulations of trade wind cumuli under a strong inversion. *J. Atmos. Sci.*, **58**, 1870–1891.

Stull, R. B., 1998: An Introduction to Boundary Layer Meteorology. *Kluwer Academic Publishers.*, **1998-07-31**, 683.

Stull, R. B. and E. W. Eloranta, 1984: Boundary Layer Experiment. *Bull. Amer. Meteor. Soc.*, **65**, 450–456.

Stull, R. B., E. Santoso, L. K. Berg, and J. Hacker, 1997: Boundary Layer Experiment(BLX96). *Bull. Amer. Meteor. Soc.*, **78**, 1149–1158.

Sullivan, P. P., J. C. McWilliams, and C. H. Moeng, 1994: A subgrid-scale model for large-eddy simulation of planetary boundary-layer flows. *Boundary-Layer Meteorology.*, **71**, 247–276.

Teixeira, J., et al., 2008: Parameterization of the atmospheric boundary layer: A view from just above the inversion. *Bull. Amer. Meteor. Soc.*, **89**, 453–458.

Thompson, N., K. L. Webber, and B. P. Norris, 1980: Eddy-fluxes and spectra in the GATE sub-cloud layer. *Quart. J. Roy. Meteor. Soc.*, **106**, 277–292.

Tiedtke, M., 1989: A comprehensive mass flux scheme for cumulus parameterization in large-scale models. *Mon. Wea. Rev.*, **117**, 1799–1801.

Vogelmann, A. M., et al., 2012: RACORO extended-term, aircraft observations of boundary-layer clouds. *Bull. Amer. Meteor. Soc.*, **Submitted**.

Wang, S. and B. Stevens, 2000: Top-hat representation of turbulence statistics in cloud-topped boundary layers: A large-eddy simulation study. *J. Atmos. Sci.*, **57**, 423–441.

Warner, J., 1977: Time variation of updraft and water content in small cumulus clouds. *J. Atmos. Sci.*, **34**, 1306–1312.

Williams, A. G. and J. M. Hacker, 1992: The composite shape and structure of coherent eddies in the convective boundary layer. *Bound.-Layer Meteor.*, **61**, 213–245.

Wood, C. R., E. J. O'Connor, R. A. Hurley, and R. Reynolds, 2009: Cloud-radar observations of insects in the UK convective boundary layer. *Meteor. Appl.*, **16**, 491–500.

Wu, W., Y. Liu, M. P. Jensen, and T. Toto, 2011: Comparative study of different cloud fraction estimates over the southern great plains. *The Second Science Team Meeting of the Atmospheric System Research (ASR) Program*, San Antonio, TX, March 28-April 1, http://www.ecd.bnl.gov/pubs/BNL–94 698–2011–AB.pdf.

Young, G. S., 1988: Turbulence structure of the convective boundary layer. Part I: Variability of normalized turbulence statistics. *J. Atmos. Sci.*, **45**, 719–726.

Zhu, P. and B. A. Albrecht, 2002: A theoretical and observational analysis on the formation of fair-weather cumuli. *J. Atmos. Sci.*, **59**, 1983–2005.

Zhu, P. and B. A. Albrecht, 2003: Large eddy simulations of continental shallow cumulus convection. *J. Geophys. Res.*, **108**, D15, 4453, doi:10.1029/2002JD003 119.

Zhu, P. and C. S. Bretherton, 2004: A simulation study of shallow moist convection and its impact on the atmospheric boundary layer. *Mon. Wea. Rev.*, **132**, 2391–2409.